CHAPTER 3

RESULT AND DISCUSSION

CHAPTER-3
RESULT AND DISCUSSION

3.1 Pyrano-pyrazoles (EPPs) as corrosion inhibitors

Pyrano-pyrazoles derivatives are reported as potentially active pharmaceutically compounds and as effective corrosion inhibitors. These compounds have been used in various medicinal activities like; These derivatives have been used as anti-cancer, antibacterial, anti-inflammatory, anti-fungal, antitubercular, anti-malarial, anti-oxidant, antihypertensive, vasodilator, etc. [Reddy *et al.* (2016)], [Gogoi *et al.* (2009)]

In view of above, the present work describes the corrosion inhibition efficiency of three pyrano-pyrazole derivatives (EPPs) on mild steel corrosion in 1M HCl solution using electrochemical impedance spectroscopy (EIS), potentiodynamic polarization, gravimetric measurements, scanning electron microscopy (SEM), atomic force microscopy (AFM). Theoretical calculations were done by density functional theory (DFT), and the Monte Carlo simulation methods (MC). The novelty of the work is that Ethyl 6-amino2, 4-dihydropyrano [2, 3, C] pyrazole-5-carboxylate (EPPs) has not been investigated earlier as metallic corrosion inhibitors. Survey of literature showed there are a few reports on use of pyranopyrazole derivatives as corrosion inhibitors for mild steel in hydrochloric acid[Yadav *et al*, (2015)], [Yadav *et al.* (2012)]. The literature survey revealed that pyrano-pyrazole derivatives showed good inhibition efficiency. Further, a careful survey of literature revealed that Ethyl 6-amino2, 4-dihydropyrano [2, 3, C] pyrazole-5-carboxylate (EPPs) derivatives synthesized in our lab, Oxygen containing pyran is fused with pyrazole ring which contains two N atoms. In addition to this two functional groups such as NH_2 and carboxylate group are attached with pyrano-pyrazole ring. All these structural features favour adsorption of inhibiting molecule

on the metal surface there by giving high inhibition effect. The investigated inhibitors exhibited more than 98 % efficiency at 100 mg/L. The choice of these compounds as corrosion inhibitors is based on the fact that they can: (a) be easily synthesized using green starting materials with high yield, (b) exhibit high inhibition efficiency even at very low concentrations, (c) strongly adsorb on metal surface through polar functional groups (-CH_3, -H, -NO_2) and aromatic rings and thereby inhibit corrosion effectively. The molecular structure, IUPAC name and abbreviation of the inhibitors used are given in Table 3.1.1.

Table 3.1.1: IUPAC name, molecular structure, abbreviation and analytical data of the studied inhibitor molecules (EPPs)

S. No.	IUPAC name of Inhibitor	chemical Structure	Analytical data
1	(Ethyl 6-amino-3-methyl-4-(P-tolyl) 2,4dihydropyrano[2,3,C]pyrazole-5-carboxylate) (EPP-1)	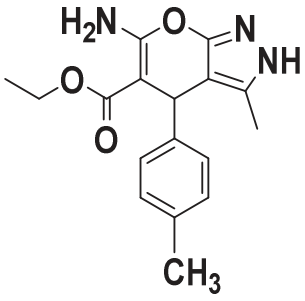	Off white crystalline powder; m.p= 190-200oC; 1H NMR (500 MHz, DMSO-d6):δ (ppm)=2.20 (CH_3), 4.19 (CH_2), 4.75 (CH), 6.83 (NH2) 7.08–7.42 (Ar-H), 11.82 (NH) ^{13}C NMR (DMSO-d6):δ (ppm)=13.44, 21.88,34.82,60.84,79.12, 114.22,124.28,129.26,135.24,140.44,160.12,164.54,170.82

2	Ethyl (6-amino-3-methyl-4(phenyl)-2,4dihydropyrano[2,3,C]pyrazole-5- carboxylate) (EPP-2)	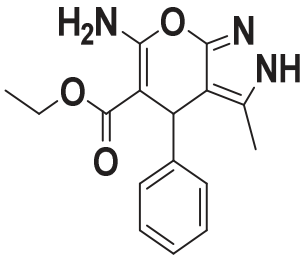	Off white crystalline powder; m.p= 273oC; 1H NMR (500 MHz, DMSO-d6):δ (ppm)= 1.96 (CH_3), 4.21 (CH_2), 4.96 (CH), 6.89 (NH_2), 7.21–7.45 (Ar-H), 12.06 (NH) ^{13}C NMR (DMSO-d6):δ (ppm)= 13.82, 35.60, 62.02,79.20, 113.24,126.01, 129.42, 139.72, 143.18, 159.28, 163.88, 169.92
3	(Ethyl 6-amino-3methyl-4-(3-nitrophenyl) 2,4-dihydropyrano[2,3,C]pyrazole-5-carboxylate) (EPP-3)	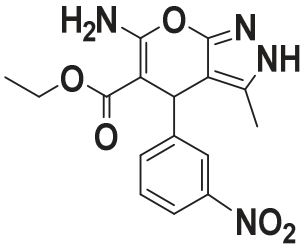	Pale yellow crystalline powder ; m.p= 260-263^{o}C; ^{1}H NMR (500 MHz, DMSO-d_6):δ (ppm)=1.93 (CH_3), 4.31 (CH_2), 4.71(CH), 6.83(NH_2) 7.45– 8.32 (Ar-H), 11.95 (NH) ^{13}C NMR (DMSO-d6):δ (ppm)= 13.88,33.62, 61.54, 79.22, 113.80, 121.25, 133.10, 140.24, 147.82, 160.12, 164.28, 170.12

3.1.1. Weight loss measurements

3.1.1.1. Inhibitor Concentration Effect

The variation of inhibition efficiency with inhibitor concentrations is shown in Figure. 3.1.1. The values of weight loss parameters such as corrosion rate (C_R), inhibition efficiency (η%), and surface coverage (θ) obtained from weight loss measurements are given in Table 3.1.2. The weight loss measurements show that η% increases with increasing concentration for all the inhibitors and attain a maximum value 98.57% for EPP-1, 96.19% for EPP-2, 91.90% and for EPP-3, at 100mgL^{-1}. The highest inhibition efficiency achieved by EPP-1 is due to the electron donating (-CH_3) group attached to phenyl ring. EPP-3 showed slightly lower efficiency than EPP-1 due to presence of electron withdrawing NO_2 group. Further increase in concentration did not cause any significant change in the inhibition performance suggesting that 100 mgL^{-1} is the optimum concentration. The inhibitor molecules adsorb onto the metallic surface perpendicularly because of the electrostatic repulsion function at higher concentration [Zarrouk *et al.* (2015)] The increased inhibition efficiency upon increasing concentration of EPPs is attributed to increase in the extent of surface coverage by the inhibitor molecules [Zarrouk *et al.* (2002)] From the weight loss results it is observed that the inhibition efficiency of the studied EPPs follows the order: EPP-1 > EPP-2 > EPP-3.

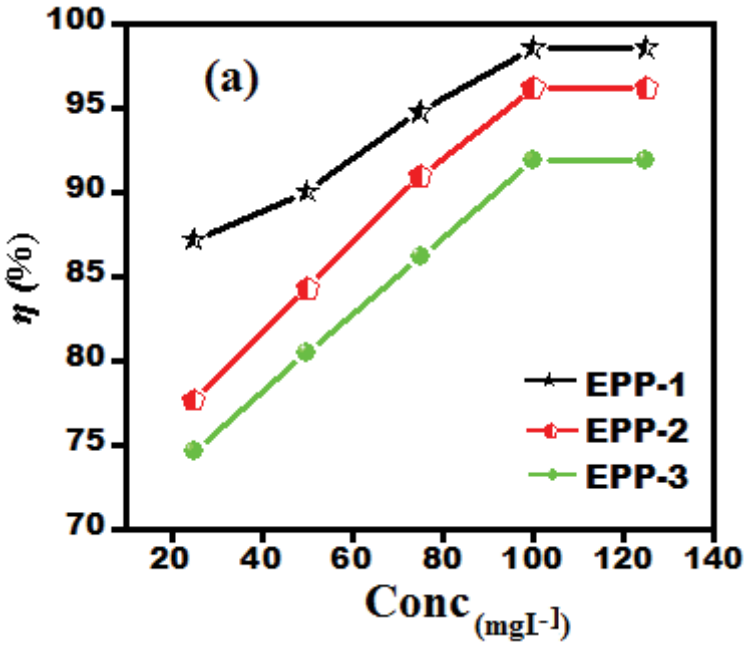

Figure 3.1.1(a) Variation of inhibition efficiency (η%) with inhibitor concentration at 308 K for MS in 1 M HCl.

Table 3.1.2: The gravimetric measurement parameters obtained for mild steel in 1 M HCl containing different concentrations of EPPs

Inhibitor	Conc (mg/L)	Weight loss (mg)	C_R (mm/y)	Inhibition efficiency (η %)
Blank	0.0	210	77.91	---
EPP-1	25	27	10.01	87.14
	50	21	7.791	90.00
	75	11	4.081	94.76
	100	3	1.113	98.57
EPP-2	25	47	17.43	77.61
	50	33	12.24	84.28
	75	19	7.049	90.95
	100	8	2.968	96.19
EPP-3	25	47	17.43	77.61
	50	41	15.21	80.47
	75	29	10.75	86.19
	100	17	6.307	91.90

3.1.1.2. Effect of temperature

The effect of temperature was studied by performing the gravimetric measurement experiments in the absence and presence of optimum concentrations of the EPPs for 3 h immersion time in the temperature range of 308-348 K. The values of the inhibition efficiency (η %) and corrosion rate (C_R) derived from the gravimetric measurement experiments at different temperatures are presented in Table 3.1.3. From the results depicted in Table 3.1.3 it is seen that an increase in temperature causes decrease in the η% and

increase in the C_R. The decreased η% and increased C_R with increasing temperatures may due to desorption of the adsorbed inhibitor molecules leading to greater surface area of mild steel exposed to the acidic solution[Ansari *et al* (2015)]. Moreover, rapid etching, desorption, and decomposition and/or rearrangement of inhibitor molecules might also be responsible for the decrease in the inhibition performance at elevated temperatures [Cao *et al*. (2014)].

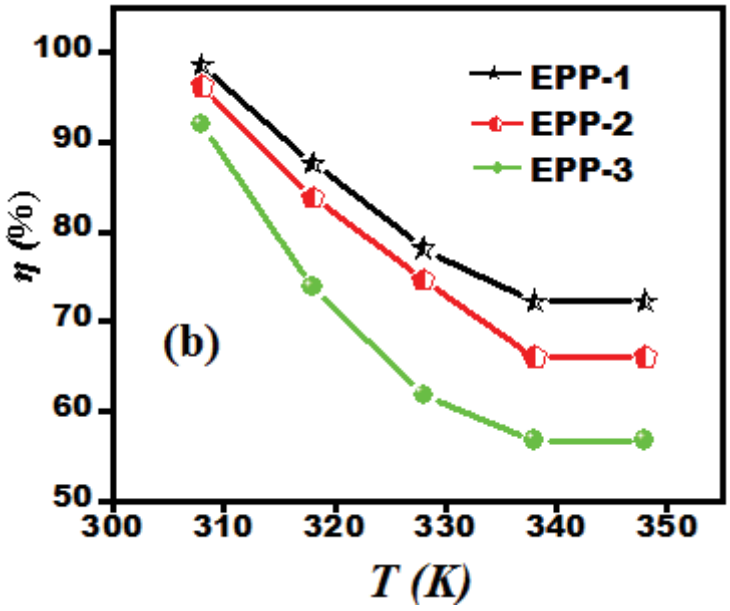

Figure 3.1.2(b): Variation of inhibition efficiency (η%) with solution temperature (308-338 K) at optimum concentration of EPPs

Table 3.1.3: Variation of C_R and η % with temperature in absence and presence of optimum concentration of EPPs in 1M HCl

Temperature (K)	**Corrosion rate (C_R) (mg cm^{-2} h^{-1}) and Inhibition efficiency (η%)**							
	Blank		**EPP-1**		**EPP-2**		**EPP-3**	
	C_R	η%	C_R	η%	C_R	η%	C_R	η%
308	7.00	---	0.1	98.5	0.26	96.1	0.56	91.9
318	9.66.	---	1.2	87.5	1.56	83.7	2.53	73.7
328	14.6	---	3.2	78.0	3.70	74.6	5.56	61.8
338	18.7	---	5.2	72.2	6.36	66.0	8.11	56.7
348	22.2	---	5.2	72.3	6.36	66.0	8.11	56.7

The temperature dependency of C_R can be expressed with the aid of Arrhenius equation, where the natural logarithm of C_R is a linear function of $1/T$ [Haque *et al.* (2017)], [Verma *et al.* (2016**(a)**]. The values of E_a were calculated from the slope of Arrhenius plots ($-\Delta E_a/2.303R$) [Figure 3.1.3)] for all studied EPPs. The calculated values of E_a were 113.3kJmol^{-1}, 90.1kJmol^{-1} and 76.6kJmol^{-1} for EPP-1, EPP-2 and EPP-3, respectively. The values of activation energy are higher in the presence of the EPPs ranging from 76.66 to 113.3kJmol^{-1} compared to 28.74 kJmol^{-1} observed in the absence of the inhibitors. A larger increase in activation energy is observed for the more efficient inhibitor. The higher values of E_a suggested that more energy barrier have been achieved in presence of inhibitors and the rate of mild steel dissolution is reduced due to the formation of inhibitors–Fe complex [Schmidt and Bedbur (1985)].

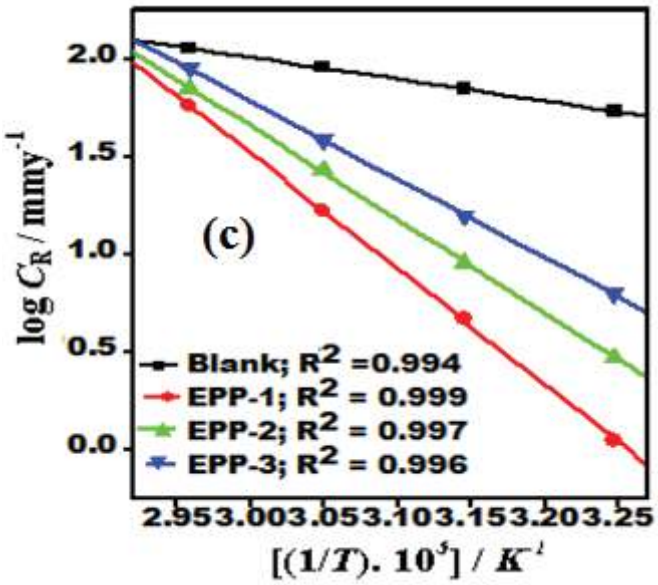

Figure 3.1.3: (c) Arrhenius plots for the corrosion of mild steel in 1 M HCl

3.1.3. Adsorption isotherm

Adsorption isotherm experiment was carried out to understand the mechanism of corrosion inhibition and interaction of inhibitor molecules with the metal surface. The adsorption isotherms provide structural as well as thermodynamic information of the adsorbed double layer. Various isotherms namely Langmuir, Temkin and Frumkin were tested among which the Langmuir isotherm [Figure 3.1.4] showed the best fit with regression coefficient (R^2) values close to unity for all studied compounds, whereas for Frumkin and Temkin isotherms, the values of R^2 were much apart from unity. Further, although the values of R^2 in Langmuir adsorption isotherm were close to one.

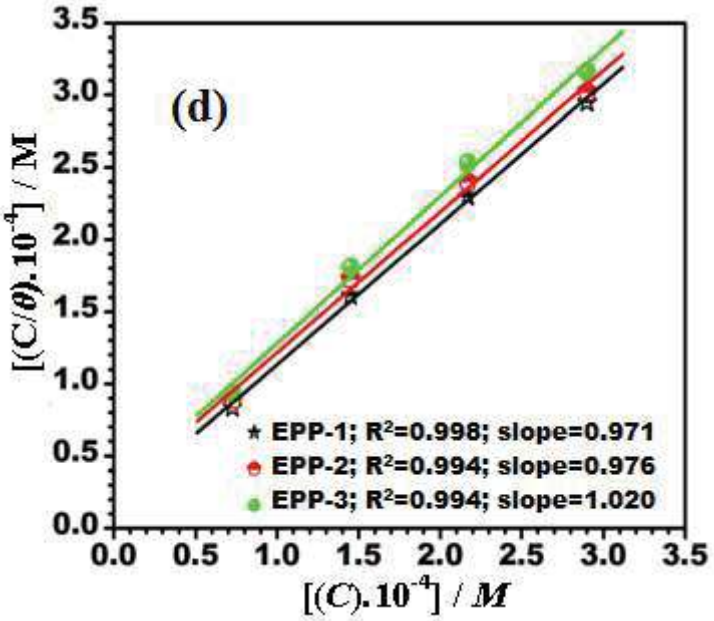

Figure 3.1.4: Langmuir adsorption isotherm plots for the adsorption of EPPs on mild steel surface in 1M HCl

It is reported that, the values of ΔG_{ads} varying between -40 kJ mol^{-1} or more negative suggests that the adsorption is chemisorptions, while a value of ΔG_{ads} around -20 kJ mol^{-1} or less negative implies that the adsorption is electrostatic interaction i.e. physiosorptions. The values reported in Table 3.1.4 range between -34.67to -39.16 kJ mol^{-1} which is close to -40 kJ mol^{-1} thereby, suggesting mixed mode of adsorption and predominantly by chemisorptions [Verma *et al.* (2015**(a)**], [Yıldız *et al.* (2014)]

Table 3.1.4: The values of K_{ads}, ΔG°_{ads} and E_a for mild steel in the absence and presence of optimum concentration of EPPs in 1M HCl at 308K

Inhibitor	K_{ads} **($10^4 M^{-1}$)**	$-\Delta G^{\circ}_{ads}$ **(k $Jmol^{-1}$)**	E_a **(kJ mol^{-1})**
Blank	----	----	28.74
EPP-1	7.8	39.16	113.39
EPP-2	3.6	37.19	90.16
EPP-3	1.3	34.67	76.66

3.1.4. Potentiodynamic Polarization measurements

The potentiodynamic polarization measurements were undertaken in order to study the effect of investigated inhibitors (EPPs) on the anodic mild steel dissolution and cathodic hydrogen evolution reactions. The polarization curves for mild steel dissolution in the absence and presence of EPPs at optimum concentration are shown in Figure 3.1.4. Extrapolation of the linear segments of cathodic and anodic Tafel curves furnished essential corrosion parameters such as corrosion potential (E_{corr}), corrosion current density (i_{corr}) and anodic and cathodic Tafel slopes (β_a and β_c respectively). These polarization parameters along with calculated inhibition efficiency (η%) are presented in Table 3.1.5.

From Table 3.1.5, it is clear that the addition of inhibitor causes a remarkable decrease in corrosion current density (i_{corr}). It should be noted that the cathodic Tafel slope values as more affected as compared to anodic slopes in presence of inhibitors, which suggests that cathodic reaction is more inhibited than anodic reaction, Thereby indicating that inhibitors are predominantly cathodic. The E_{corr} values in the presence of all the three inhibitors are in the range of 58 to 75 mV. The literature survey shows that the values range

suggests mixed type mechanism but predominantly cathodic, since there is a slight shift in the E_{corr} values towards cathodic region. [Qian *et al*. (2013); Mourya *et al*. (2014); It is clear from Figure. 3.1.4 that the both the anodic and cathodic current densities decrease significantly with addition of inhibitors, which indicates that inhibitor molecules inhibit both the anodic and cathodic reactions. The parallel cathodic Tafel lines (Figure. 3.1.4) suggests that the addition of inhibitors does not modify the mechanism of the reduction reaction. The values of both anodic and cathodic Tafel slopes (β_a , β_c) slightly change when the addition of inhibitor, which suggests that the addition of the inhibitor reduces the anodic dissolution of mild steel as well as retards the cathodic hydrogen evolution reaction, without affecting the reactions mechanism [Solmaz (2014)].

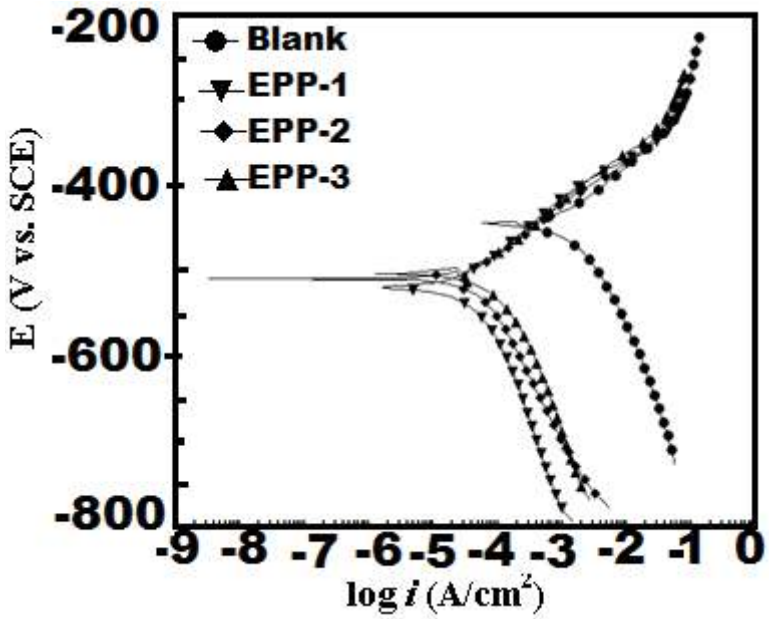

Figure 3.1.5: Polarization curves for mild in absence and presence of optimum concentrations EPPs

Table 3.1.5: Potentiodynamic polarization parameters (±SD) for mild steel in 1M HCl in absence and presence of optimum concentration (100 mg L^{-1}) of EPPs at 308K

Inhibitor	E_{corr} (mV/SCE)	i_{corr} (μA/cm^2)	β_a (mV/dec)	$-\beta_c$ (mV/dec)	η (%)
Blank	-445	1320(0.003)	74.6	123.9	----
EPP-1	-520	38.4(0.04)	77.7	142.9	98.8
EPP-2	-509	52.9(0.004)	68.6	143.6	96.4
EPP-3	-503	77.6(0.003)	75.9	138.6	94.3

3.1.6: Electrochemical impedance spectroscopy (EIS) studies

The EIS measurement was carried out to understand the kinetics of the electrochemical process at MS/solution interface in the absence and presence of inhibitors. The Nyquist plots, equivalent circuit model and Bode-phase angle plots are presented in Figures 3.1.6 (a, b, c) and the corresponding parameters are listed in Table 3.1.6. The effect of the synthesized compounds on the corrosion behaviour of mild steel in 1 M HCl was also investigated by means of EIS method. The Nyquist plots obtained for mild steel in 1 M HCl in the absence and presence of optimum concentration of the studied inhibitors are shown in Figure 3.1.6(a). It is seen that, the Nyquist plot of mild steel in the absence and presence of the inhibitor contains a slightly depressed semi-circular shape, which indicates that the corrosion of mild steel in 1M HCl solution is mainly controlled by a charge transfer process [Achouri *et al.* (2001)].It is also evident from Figure 3.1.3 that the diameter of the Nyquist plots increases with increasing inhibitors concentration which is attributed to the formation of protective film on mild steel surface leading to successful retardation of the corrosion process [Yousefi *et al.* (2015)].For a metallic system corroding in acid solution, the replacement of capacitance

by CPE gives a better approximation [Roy *et al.* (2015)]. The impedance parameters were derived from the EIS spectra of the studied compounds using a previously described equivalent circuit [Zhang *et al.* (2009)], and the results are presented in Table 3.1.6.

Bode and phase angle plots show only one time constant (Figure 3.1.4), which is related to relaxation process corresponding to one semi-circle capacitive loop in the Nyquist plots. The ideal capacitor behaviour would result if a slope value attains -1 and phase angle values attain -90° [Sudheer and M.A. Quraishi (2013)]. In present study the Bode and phase angle values in blank are-0.53 and -40° and in presence of EPPs range from -0.81 to -0.88 and -61° to -76°.

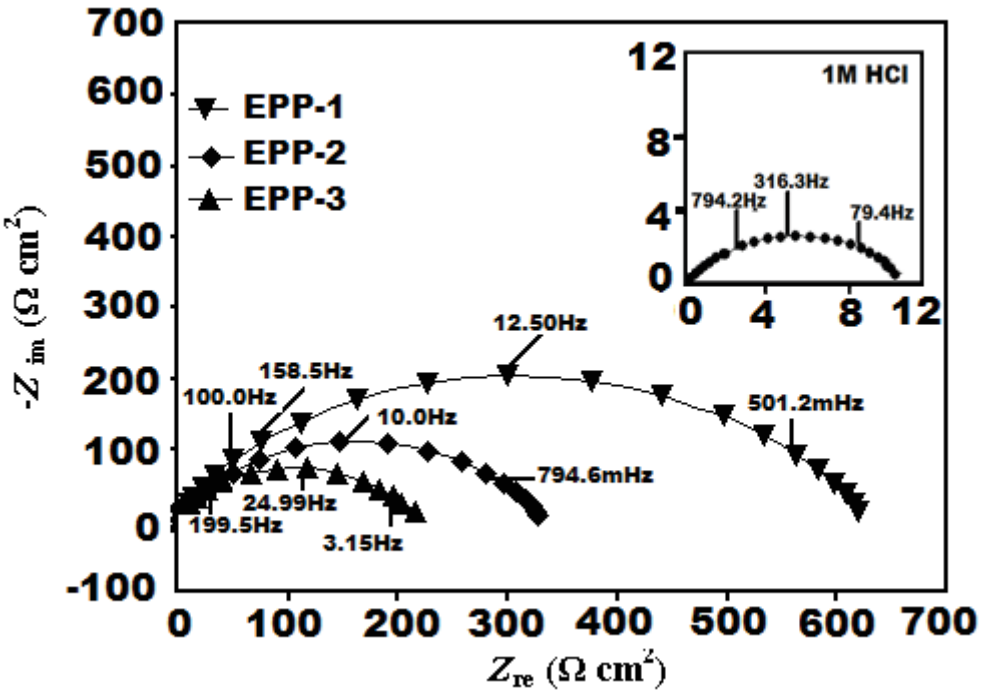

Figure 3.1.6: Nyquist plots for the mild steel at optimum concentration of inhibitors EPPs

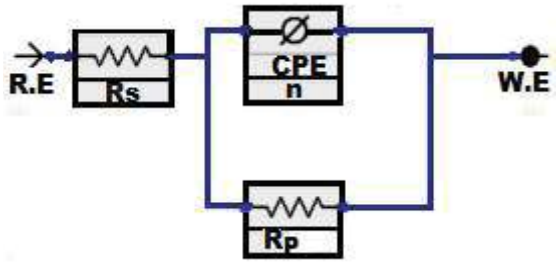

Figure 3.1.6 (b): Equivalent circuit model used to analyze the EIS data.

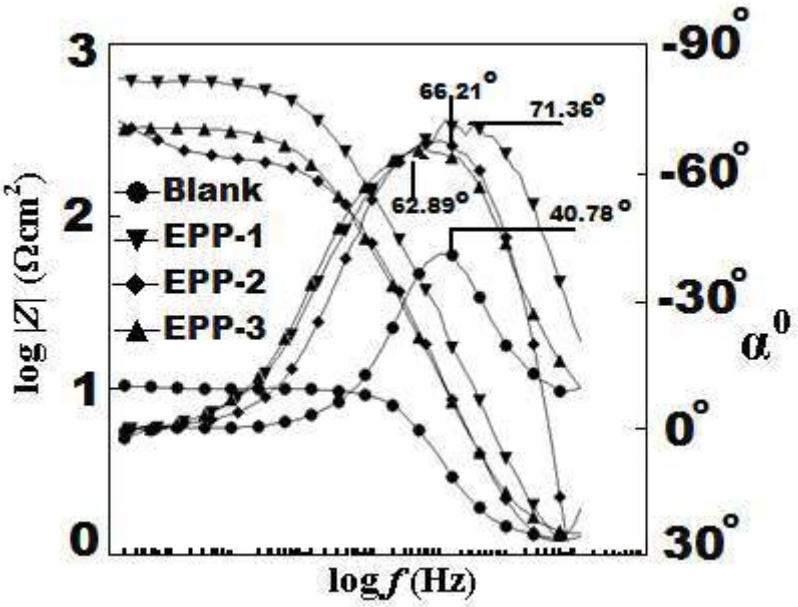

Figure 3.1.6 (c) Bode (log *f* vs log |*Z*|) and phase angle (log *f* vs α) plots for MS in 1 M HCl without and with EPPs

Table 3.1.6: Electrochemical impedance parameters (±SD) for mild steel in 1M HCl in absence and presence of optimum concentration (100 mg L^{-1}) of EPPs at 308K

C_{inh} (mgL^{-1})	R_s (Ω)	R_p (Ω cm^2)	n	Y_0 (μF/cm^2)	C_{dl} (μF/cm^2)	η (%)
Blank	1.02(0.002)	7.44 (0.002)	0.798	481.2	137.9	----
EPP-1	0.76(0.002)	590.1(0.002)	0.843	44.2	20.6	98.7
EPP-2	1.19(0.002)	319.4 (0.002)	0.825	54.7	22.5	97.6
EPP-3	1.17(0.002)	199.7 (0.002)	0.808	107.9	39.4	96.2

3.1.7. Surface characterization

The SEM micrographs for MS in absence and presence of EPP -1, EPP -2, and EPP -3 are shown in Figure 3.1.7.(a-d). The SEM image without inhibitor is highly corroded (Figure 3.1.7. (a), resulting in a rough and heterogeneous surface of MS in 1 M HCl. But in the presence of the studied EPPs, the MS surface is smoother, which confirms their inhibition action as shown in Figures 3.1.7(b-d) [Yadav *et al*. (2013) (a)].

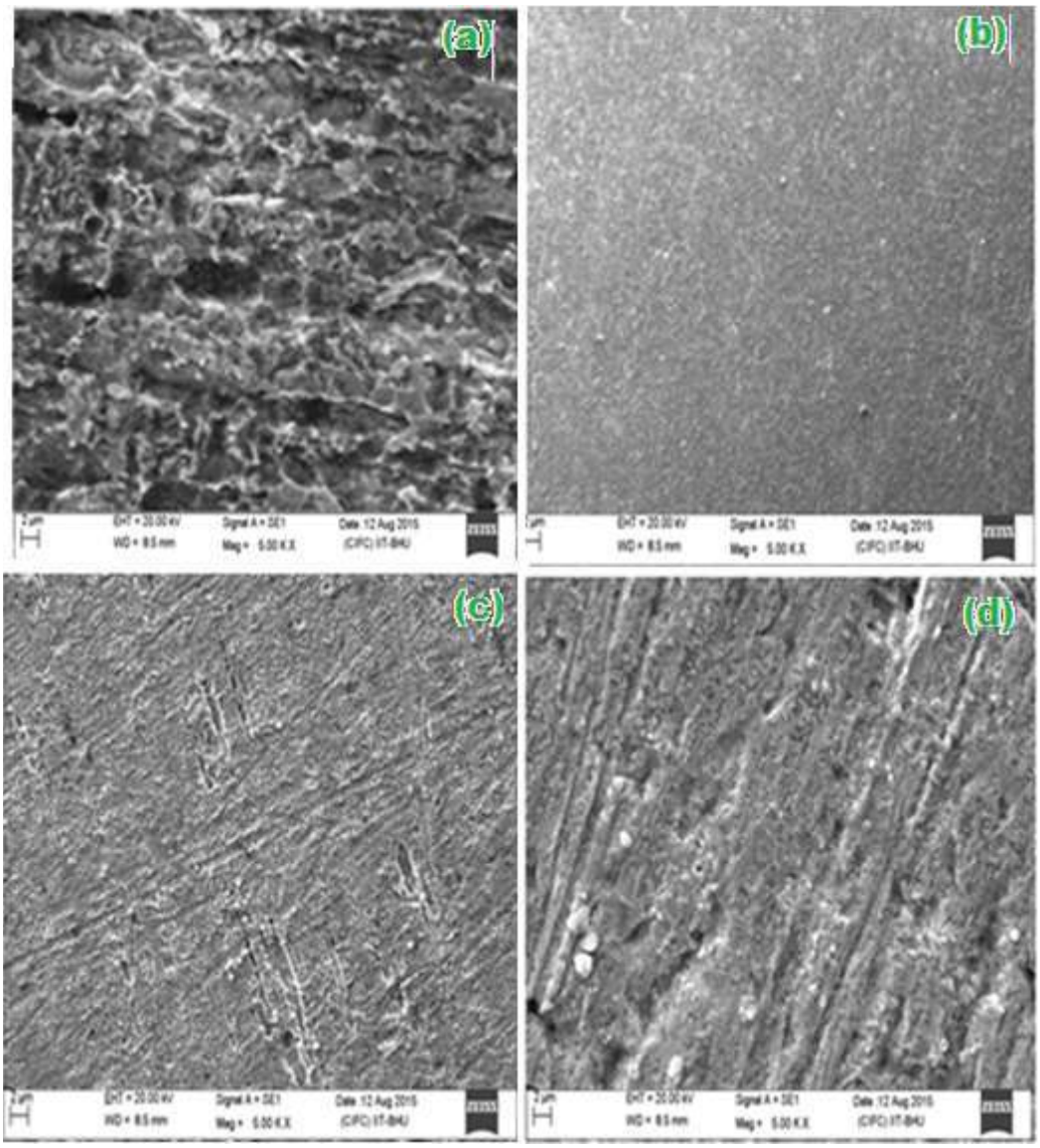

Figure 3.1.7(a-d) SEM micrographs for MS in (a) 1 M HCl and in presence of inhibitors (b) EPP-1, (c) EPP-2, and (d) EPP-3 at 100mgL^{-1}.

AFM is another useful method for the surface analysis [Mourya *et al.* (2014)].In the absence of pyrano-pyrazoles; the surface displayed an extremely rough topography due to unhindered acid attack (Figure 3.1.8. (a)) while in presence of EPP -1, EPP -2, and EPP -3, the MS shows smoother surface (Figure 3.1.8 (b-d)). Both the surface studies supported the corrosion inhibition for MS in presence of inhibitors.

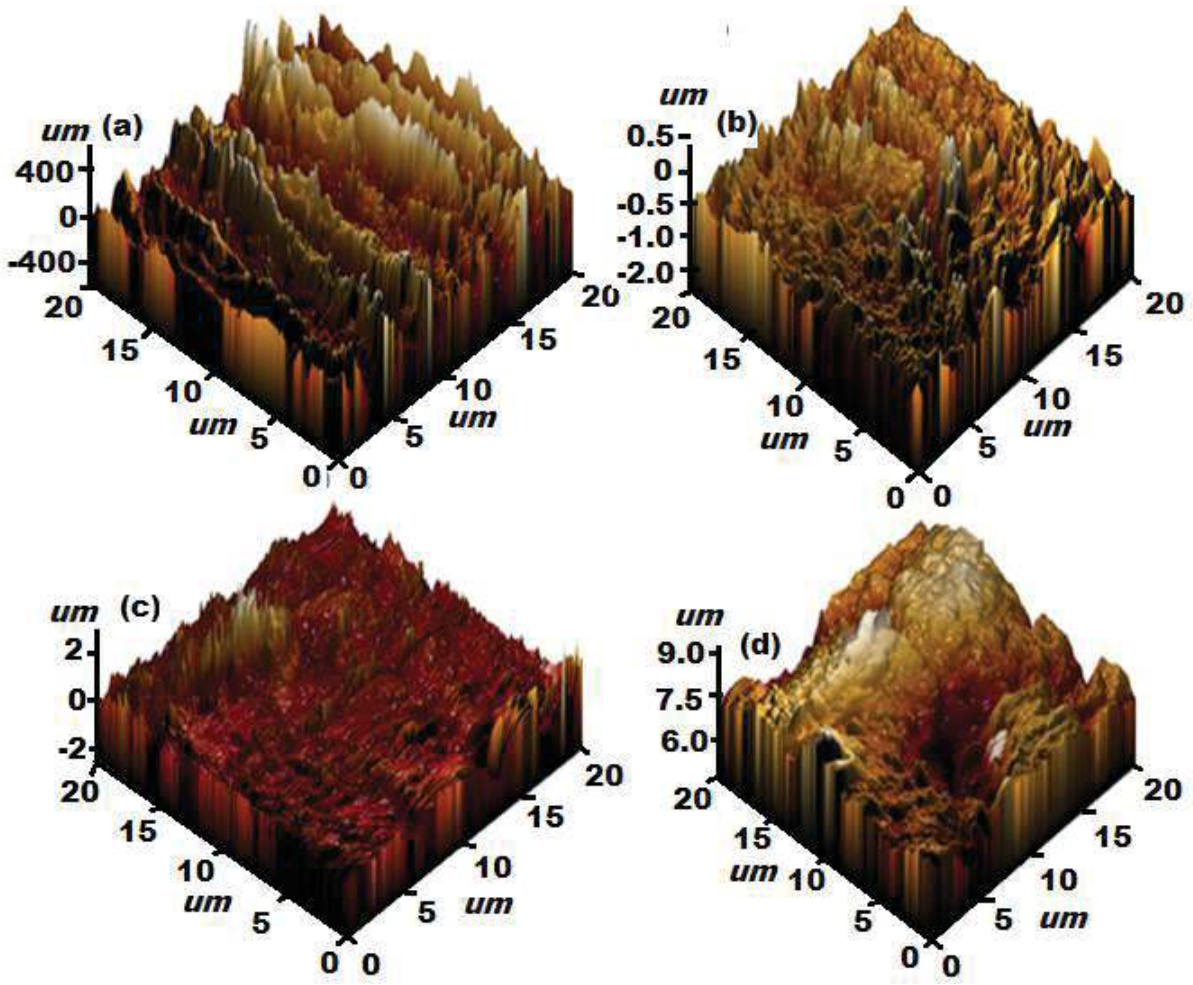

Figure 3.1.8: (a-d) AFM micrographs for MS (a) in 1 M HCl and in presence of inhibitors (b) EPP -1, (c) EPP -2, and (d) EPP -3 at 100mgL^{-1}.

3.1.8. Quantum chemical calculations

The gas phase optimized molecular structures and the respective HOMO and LUMO electron density surfaces of the studied compounds are shown in Figure 3.1.9. The optimized structures revealed that the molecules of the studied compounds adopt near planar geometries. The near planar geometries of these compounds might contribute to their high inhibition efficiencies because high degree of planarity has been reported to favour optimum adsorption of inhibitor molecules on metal surface leading to enhanced inhibition efficiency [Gomez *et al.* (2006)], [Arslan *et al.* (2009)], [Bentiss and Lagrenee (2011)]. The HOMO

electron density surface provides information about the sites of the molecule that are most likely to donate electrons to the appropriate orbital of an acceptor species, while the LUMO electron density surface suggests the sites of the molecule that possess higher chances of accepting electrons from a donor species. The FMO electron density distribution of the studied compounds exhibit similar features of the LUMO but clearly different HOMO surfaces. For this reason, the variation in the inhibition efficiencies of the studied molecules might not be describable based on the LUMOs. Both the HOMOs and the LUMOs of the studied molecules comprise the π- type orbital, which suggests that the molecules can favourably interact with the vacant/filled d- or p- orbitals of the metal atom. It can be observed that in case of neutral inhibitor molecules (EPP-1, EPP-2 and EPP-3), the HOMO electrons are distributed over the phenyl ring, nitrogen and oxygen atoms of the pyranopyrazole derivatives. In case of EPP-1 and EPP-2 LUMO, the electron distribution is confined on entire molecule, where as in case of EPP-3 LUMO regions are distributed over the phenyl ring and NO_2 group. The values of calculated quantum chemical parameters such as E_{HOMO}, E_{LUMO}, ΔE (E_{LUMO} - E_{HOMO}) are listed in Table 3.1.7.The difference in energy level (ΔE= E_{LUMO} - E_{HOMO}) is an important factor for evaluation of inhibition potential. Inspection of Table 3.1.7, reveals that the value of E_{HOMO} for EPP-1is larger than that of EPP-2 and EPP-3, which suggests that EPP-1 has greater electron donating ability than EPP-2 and EPP-3. The highest E_{HOMO} value for EPP-1 is due to the presence of electron donating CH_3 group attached to phenyl ring while lowest E_{HOMO} is attributed to electron withdrawing NO_2 group. Furthermore, lowest value of E_{LUMO} suggests that EPP-1 has greater electron accepting capacity than EPP-2 and EPP-3.

The energy gap ($\Delta E = E_{LUMO} - E_{HOMO}$) is another important quantum chemical parameter which determines the reactivity and adsorption behaviour of the inhibitor molecules. Lower value of ΔE suggests easier adsorption of inhibitor molecules on the metal surface. The ΔE value of EPP-1 is lowest Table 3.1.7 and therefore it exhibits highest inhibition efficiency. Thus, the order of E_{HOMO}, E_{LUMO} and ΔE of the studied inhibitors is very well correlated with the experimentally observed inhibition efficiency, i.e. EPP-1 is better inhibitor than EPP-2 and EPP-3. The values of fraction of electrons transferred (ΔN) are reported in Table 3.1.7.In is reported that electron transfer from inhibitor to metal takes place easily when the ΔN value is greater than 0 and less than i.e. $\Delta N > 3.6$. Table 6 reveals that all the calculated ΔN values are positive and lower than 3.6, which suggests that the inhibitor molecules have strong tendency to donate electrons to the vacant d-orbital of metal. Also the value of ΔN in case of EPP-1 (0.364) is greater as compared to EPP-2 (0.350) and EPP-3 (0.268). Thus, EPP-1 can transfer more electrons and manifests higher efficiency than EPP-2 and EPP-3

Softness is also an important parameter which elucidates the adsorption ability of the inhibitor molecules. Higher the value of softness, greater would be the adsorption of inhibitor molecules over the metal surface. It is seen from Table 3.1.7 that the softness of EPP-1 (0.457) is more than EPP-2 (0.448) and EPP-3 (0.406). These results support superior corrosion inhibiting performance of EPP-1 than 2 and 3.

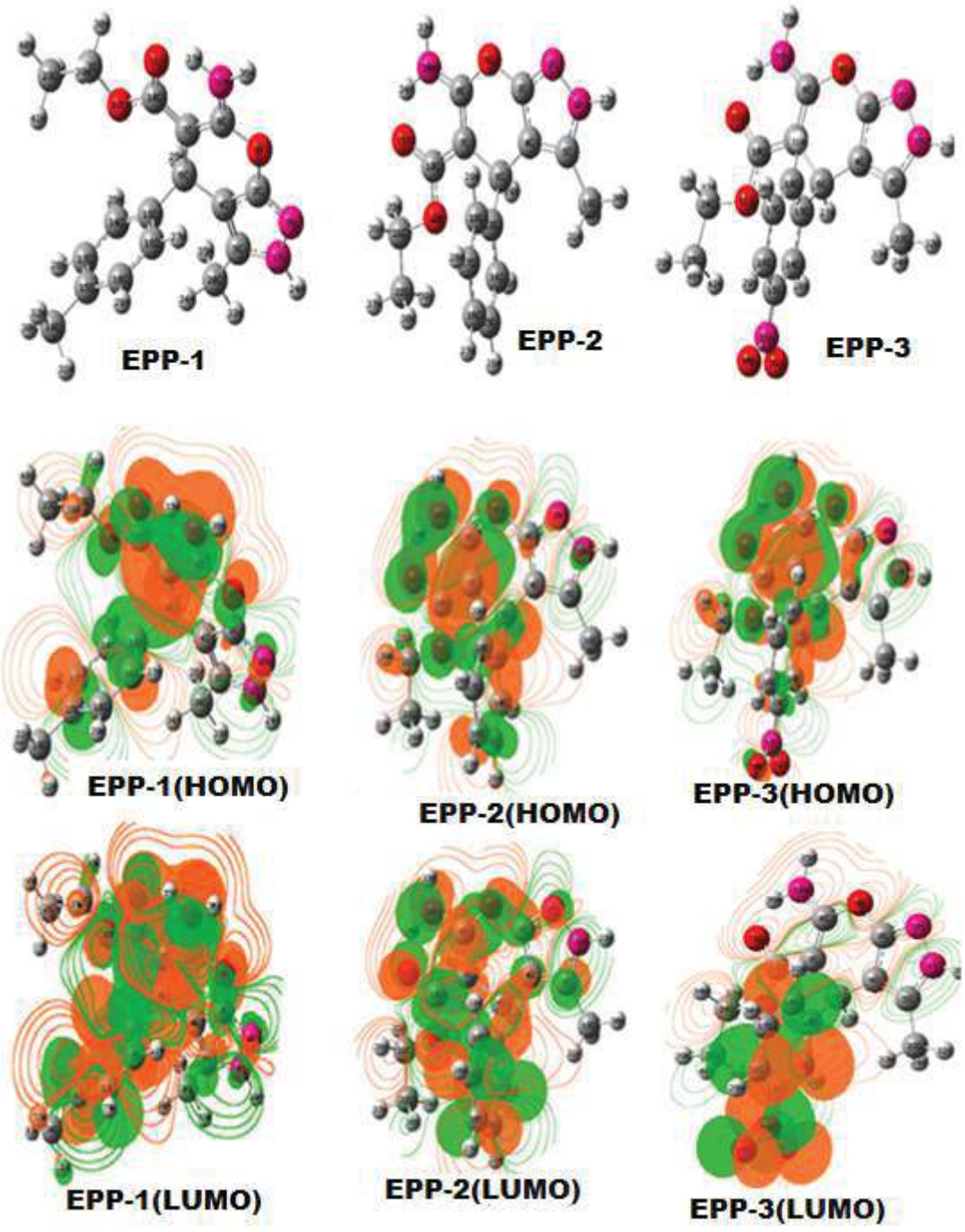

Figure 3.1.9: The gas phase optimized molecular structures, the HOMO, and the LUMO electron density distribution surfaces of EPP -1, EPP -2, and EPP -3.

3.1.8.1. Quantum chemical calculations of protonated inhibitor molecules

The heteroatom having most negative values of Mullikan charge is likely to undergo protonation easily. The optimized structures, HOMO and LUMO distribution are shown in Fig. 3.1.10. An observation of Table 3.1.7 reveals that after protonation, the E_{HOMO} values of all the inhibitors are shifted towards more negative side compared to that of E_{HOMO} values of neutral inhibitors. It suggests that after protonation, the electron donating capability of inhibitors decreased. Furthermore, Table 3.1.7, reveals that all the calculated ΔN values are negative, which means that the electron donation from inhibitor molecules to the metal surface is not possible. It is also noted that E_{LUMO} values of protonated inhibitors shift towards more negative side as compared to the neutral molecules, which suggests that the protonated inhibitors have higher electron accepting capability compared to the neutral molecules. Thus protonated molecules the bond formation between inhibitor and metal takes place by the acceptance of electrons by inhibitor molecules from metal.

Table 3.1.7. Quantum chemical parameters derived from the B3LYP/6-31+G (d,p) method of the studied compounds.

Parameters→ Compounds↓	E_{HOMO} **(eV)**	E_{LUMO} **(eV)**	ΔE **(eV)**	χ **(eV)**	η **(eV)**	$^{b}\sigma$ **(eV^{-1})**	ΔN **(eV)**
In Neutral							
EPP-1	-5.412	-1.038	4.374	3.225	2.187	0.457	0.364
EPP-2	-5.488	-1.027	4.461	3.257	2.230	0.448	0.350
EPP-3	-5.943	-1.023	4.920	3.483	2.46	0.406	0.268
In Protonated							
EPP-1	-7.676	-5.578	2.098	6.627	1.049	0.953	-0.861
EPP-2	-9.858	-5.513	3.572	7.685	2.172	0.460	-0.659
EPP-3	-9.773	-5.942	3.831	7.857	1.915	0.522	-0.792

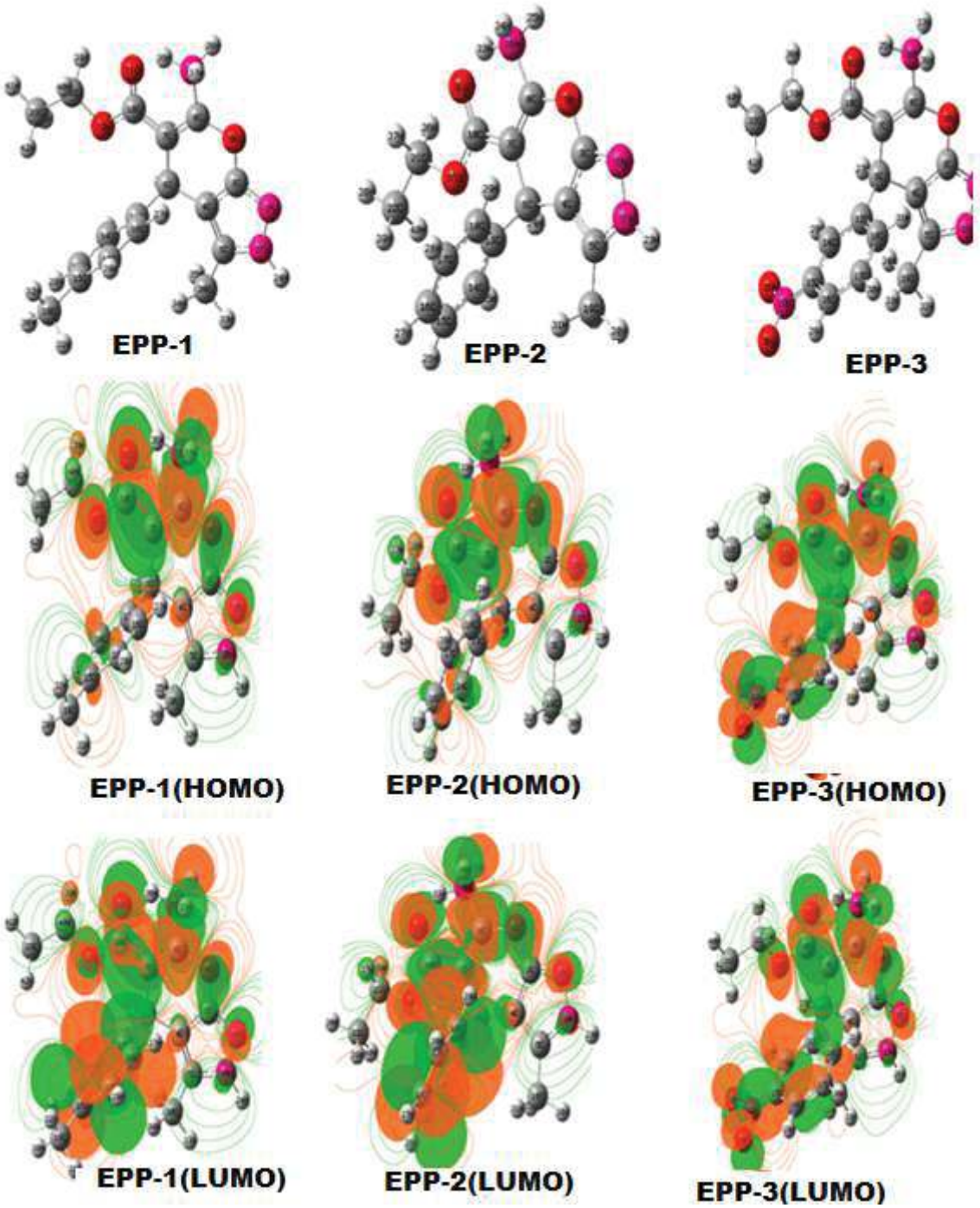

Figure 3.1.10: The Aqueous phase optimized molecular structures, the HOMO, and the LUMO electron density distribution surfaces of EPP -1, EPP -2, and EPP -3.

3.1.8.2. Fukui index analysis

The adsorption of the inhibitor molecules on the metallic surfaces takes place by the donor-acceptor interaction, which in turn depends upon the Fukui index of the inhibitor molecules. The Fukui indices are the measure of nucleophilic as well as electrophilic behaviour of the inhibitor molecules [Márquez et al (2014)]. The higher value of f_k^+ suggests acceptance of electron from the metal and higher value of f_k^- suggests higher electron donation ability of inhibitor molecules. The calculated Fukui indices are presented in Table 3.1.8: and the results show that N, O, C-atoms of the pyranopyrazole and phenyl rings are the most susceptible sites for electron acceptance or donation. In the case of EPP-1, the most susceptible sites for electrophilic attacks are N(1), N(2), C(3), C(4), C(5), C(7), O(9) and N(21) atoms respectively and the favourable sites for electron acceptance (f_k^+) are C (14), C (16), C(17) and C(18) respectively. In case of EPP-2, the favourable sites for electrophilic attacks are N(1), N(2), C(3), C(4), C(5), C(7), O(9) and N(20) atoms while, the favorable sites for nucleophilic attack are C(7), C(13), C(16) and C(18) atoms. Likewise, for EPP-3, the sites for electron acceptance are C(14), C(15), C(16), C(18), N(19), O(20) and O(21) atoms whereas, N(1), N(2), C(3), C(4), C(5), C(7), O(9) and N(23) are the electron donating atoms. The analysis of fukuii indexes reveals that pyranopyrazole and phenyl rings are the reactive sites for donor-acceptor interactions and thus facilitate the adsorption of inhibitors over the metallic surfaces.

Table 3.1.8: Calculated Fukui functions for the studied inhibitor molecules in neutral form

Atoms	EPP-1 f_k^-	EPP-1 f_k^+	EPP-2 f_k^-	EPP-2 f_k^+	EPP-3 f_k^-	EPP-3 f_k^+
C8	-0.0017	0.0042	-0.0017	0.0014	-0.0017	0.0003
O9	0.1563	-0.0001	0.1563	0.0002	0.1562	0.0000
C10	0.0009	0.0009	0.0009	0.0002	0.0009	0.0001
O11	0.0071	0.0001	0.0072	0.0001	0.0072	0.0000
O12	0.0025	0.0006	0.0024	0.0013	0.0024	0.0008
C13	0.0071	-0.0185	0.0071	0.1839	0.0071	0.0046
C14	0.0000	0.2456	0.0000	-0.0078	0.0000	0.1353
C15	0.0001	-0.0179	0.0002	0.2988	0.0002	0.0541
C16	0.0002	0.2654	0.0001	0.1868	0.0001	0.1451
C17	0.0002	0.2488	0.0001	-0.0026	0.0001	0.0044
C18	0.0001	0.2641	0.0003	0.3153	0.0002	0.2009
C19	0.0000	0.0019	-0.0037	0.0004	-----	-----
N19	-----	-----	-----	-----	0.0000	0.1855
N20	-----	-----	0.0104	0.0007	-----	-----
C20	0.0037	0.0002	-----	-----	-----	-----
O20	-----	-----	-----	-----	0.0002	0.1449
O21	-----	-----	-----	-----	0.0000	0.1455
N21	0.0105	0.0020	-----	-----	-----	-----
C21	-----	-----	0.0001	0.0006	-----	-----
C22	0.0001	0.0003	0.0000	0.0001	-0.0037	-0.0002
N23	-----	-----	----	----	0.0104	0.0003
C23	0.0000	0.0001	----	----	----	----
C24	-----	-----	----	----	0.0001	0.0002
C25	-----	-----	----	----	0.0000	0.0000

3.1.9. Monte Carlo simulation

The interaction between the inhibitor molecule and metal was studied by Monte Carlo simulation [Fu *et al* (2012)]. Fig.3.1.11. and 3.1.12 represents the adsorption behaviour of inhibitors molecules over the metal surface in vacuum and in aqueous phase respectively. It is clear that the studied inhibitor molecules are lying almost parallel to the metal. The calculated values of interaction energy ($E_{interaction}$) and binding energy ($E_{binding}$) are given in Table 3.1.9. All the values of $E_{interaction}$ in vacuum and aqueous phase are negative which suggest that adsorption is spontaneous [Sasikumar *et al* (2015)], [Verma *et al* (2016, **(b)**)]. Also EPP-1 has a maximum negative value of $E_{interaction}$ suggests that EPP-1 strongly adsorb on metal surface [Singh *et al* (2017)]. In aqueous phase the values of binding energy is more as compared to the vacuum (Table 3.1.9), which suggests that in aqueous phase inhibitors can strongly bind with the metal surface. The values of the binding energies ($E_{binding}$) in both vacuum and aqueous phase are as follows: EPP-1 > EPP-2 >EPP-3, which are in accordance with the order of their inhibition efficiencies obtained by experiment methods. The results are well correlated with experimental results.

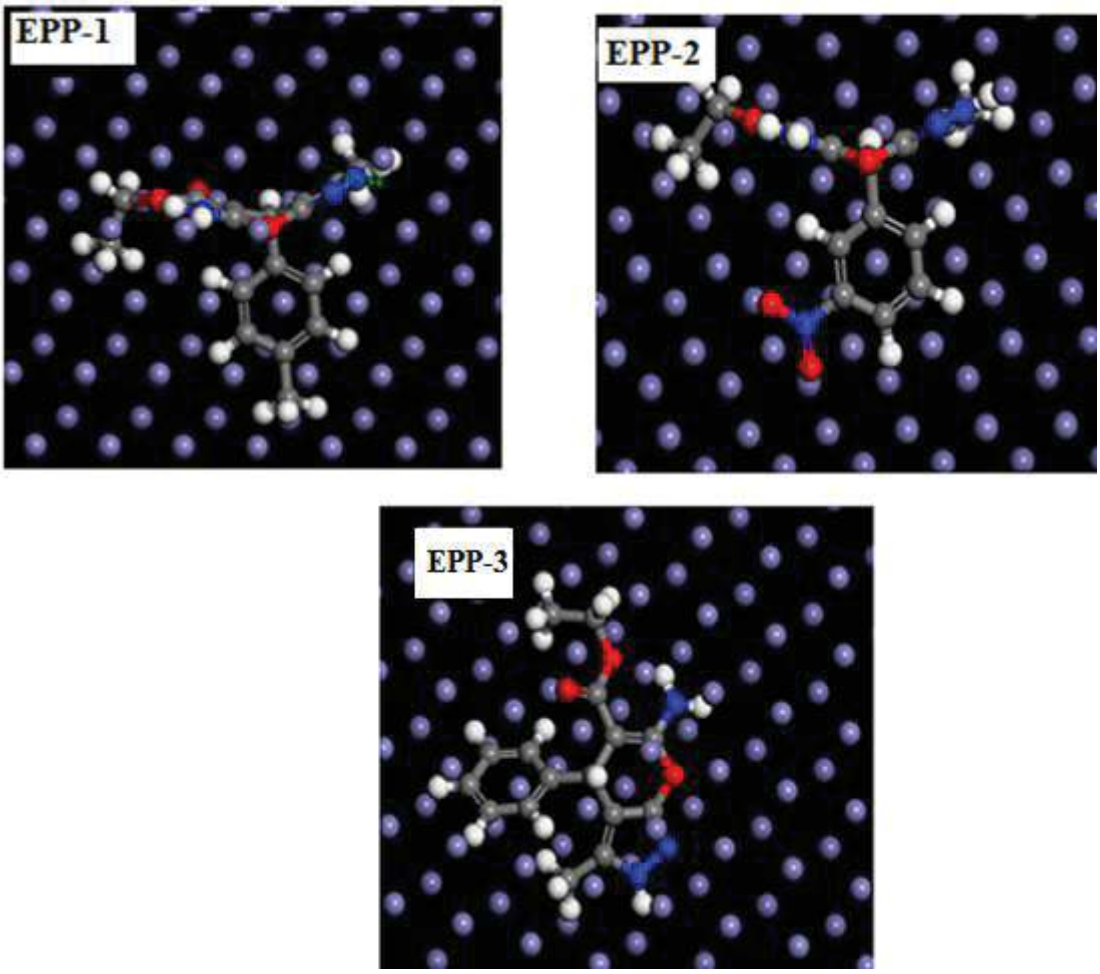

Figure 3.1.11: Side views of the most stable low energy configuration for the adsorption of (a) EPP-1, (b) EPP-2 and (c) EPP-3 on Fe (110) surface obtained by Monte Carlo Simulations in vacuum phase

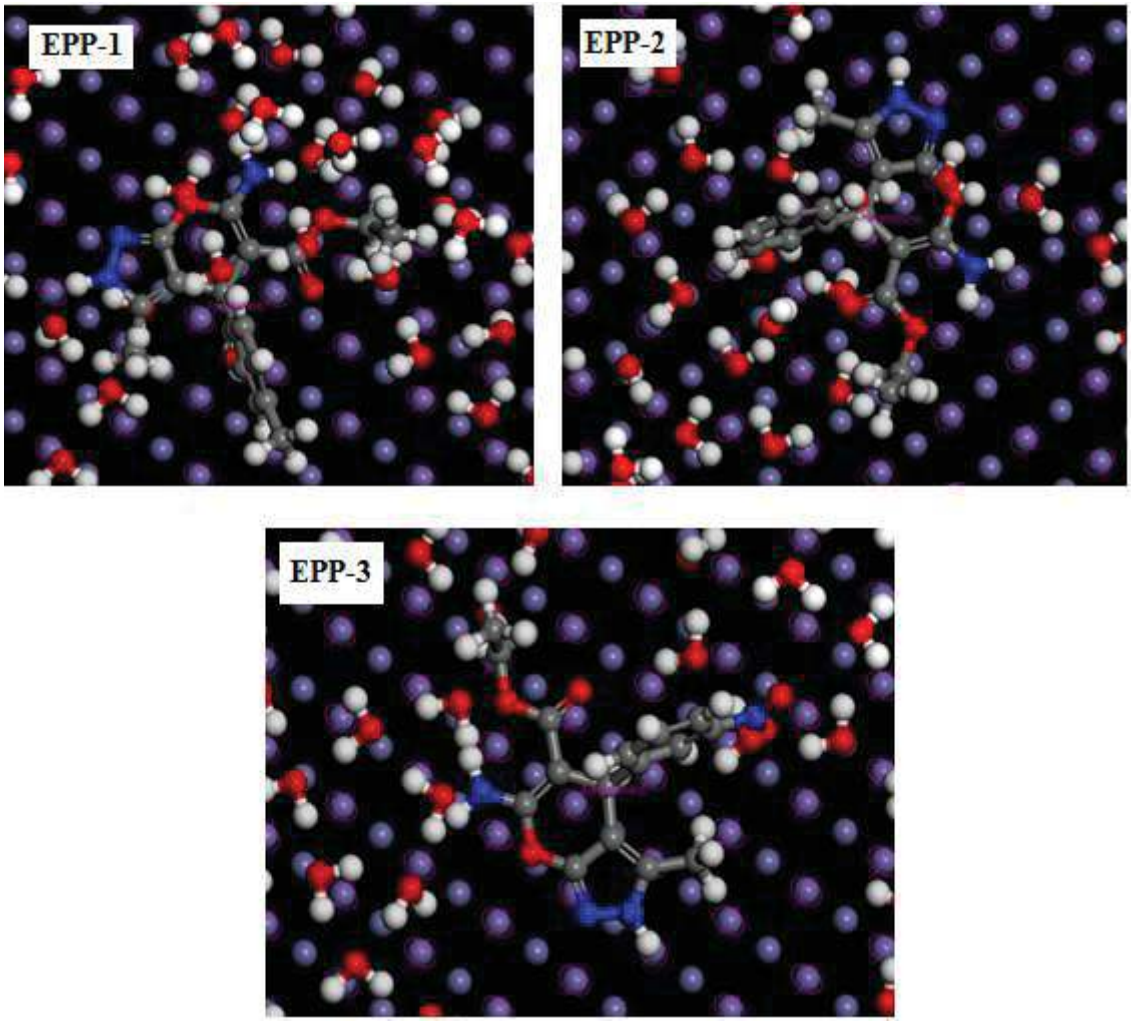

Figure 3.1.12: Side views of the most stable low energy configuration for the adsorption of (a) EPP-1, (b) EPP-2 and (c) EPP-3 on Fe (110) surface obtained by Monte Carlo Simulations in aqueous phase.

Table 3.1.9: Outputs and descriptors calculated by the Monte Carlo simulation for the most stable adsorption configurations of EPP-1, EPP-2 and EPP-3 on Fe (110) surface (all units in kJ/mol) in vacuum phase and aqueous phase.

Inhibitor	$E_{binding}$ **kJ/mol**	$E_{interaction}$ **kJ/mol**
vacuum phase		
EPP-1	820.60	-820.60
EPP-2	732.36	-732.36
EPP-3	672.22	-672.22
aqueous phase		
EPP-1	3748.45	-3748.45
EPP-2	3608.20	-3608.20
EPP-3	3594.17	-3594.17

3.2. 2, 6diaminopyridine as corrosion inhibitors

Schiff's bases are the reaction products of amine and carbonyl compounds and act as potential class of corrosion inhibitors [Silva *et al*. (2011)]. These compounds have wide applications in biological, clinical, industrial fields like corrosion inhibitors, as catalyst, dyes, pigments etc [Sılku et al. (2016)], [Small *et al.* (1998)], [Ulusoy *et al*. (2012)]. SBs act as efficient corrosion inhibitors for various metals in acidic solution. [Negm *et al.* (2012)] studied the corrosion inhibition behavior of four Schiff bases of amine as corrosion inhibitors on mild steel in IM HCl solution. These authors have reported 60-90% IE at 400mgL^{-1}. Sorkhabi *et al.* (2016)] investigated Schiff base derived from 2amino pyridine as corrosion inhibitors. These compounds exhibited maximum IE of 85-95% at 200 mg L^{-1}. [Yan Ji *et al.* (2016)] reported corrosion inhibition action of Schiff base derived from pyridin-2- ylmethyl-N, N-diethylaniline (BPMA) shows corrosion inhibition efficiency 88.1% at 450 ppm. [Hegazy *et al.* (2009)] derived Schiff bases from benzylidene thiourea give 80- 90% inhibition efficiency at very high concentration range (150 mgL^{-1}).The inhibition efficiency of Schiff bases have prompted us to synthesizes new Schiff bases to study their corrosion inhibition behavior. In the present investigation we have synthesized tree Schiff base derived from 2, 6 diaminopyridine namely N2, N6- bis(4-methylbenzylidene)pyridine-2,6-diamine (DAP-1), N2, N6-dibenzylidenepyridine- 2,6-diamine (DAP-2), N2, N6- bis(4-nitrobenzylidene)pyridine-2,6-diamine (DAP-3) and studied as corrosion inhibition for mild steel corrosion in 1M HCl medium. The survey of literature sows that these SB show wide biological activities like anti-cancer, anti-viral, anti- microbial etc [singh and Molotsi (2005)], [Navarro *et al.* (2005)], [Cheng *et al.* (2003)]. In addition to this they are likely to give good inhibition efficiency because of having nitrogen containing pyridine nucleus, two

(CH=N) azomethine and two substituted phenyl groups in the same molecule. These structural features favor adsorption of these molecules on metal surface. The corrosion inhibition tests were performed on mild steel in acidic medium using potentiodynamic polarization, electrochemical impedance spectroscopy, and gravimetric, surface SEM by scanning electron microscopy (SEM) and atomic force microscopy (AFM). The theoretical calculation using density functional theory (DFT) and the Monte Carlo simulation were also used to establish correlation between molecular structures and IE. The molecular structure and IUPAC name of the inhibitors used are given in Table 3.2.1.

Table 3.2.1: molecular structure and analytical data of DAPs

Inhibitor	Analytical data
N2, N6-bis(4-methylbenzylidene)pyridine-2,6-diamine **(DAP-1)** 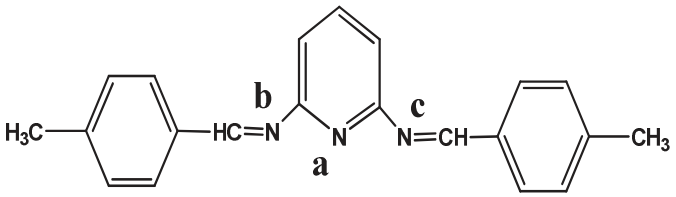	**$C_{21}H_{19}N_3$,** 313.40, 1H NMR (500 MHz, DMSO) 1H NMR (DMSO-d6,):7.91-8.03 (3 H;CH Pyridine), 7.11-7.56 (m,10H, CH benzene, 5.27(2H,2N-CH-C) 2.7-3.2 (6H,CH_3)
N2, N6-dibenzylidenepyridine- 2, 6-diamine **(DAP-2)** 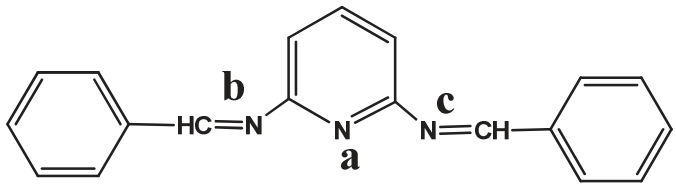	**$C_{19}H_{15}N_3$,** 285.13, 1H NMR (500 MHz, DMSO) 1H NMR (DMSO-d6,):7.88-8.16 (m,3 H;CH Pyridine), 7.11-7.56 (m,10H, CH benzene, 5.66(2H,2N-

	CH-C)
N^2, N^6- bis(4-nitrobenzylidene)pyridine-2,6-diamine **(DAP-3)** 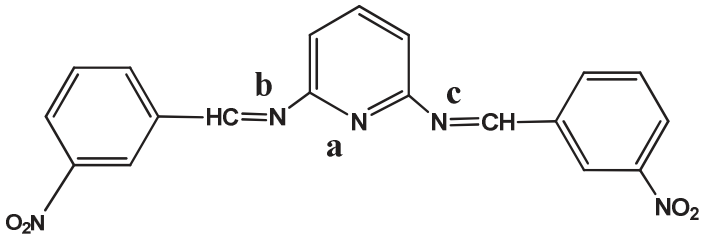	**$C_{19}H_{13}N_5O_4$,** 375.10, 1H NMR (500 MHz, DMSO) 1H NMR (DMSO-d6,):7.87-8.06 (3 H;CH Pyridine), 7.02-7.46 (10H, CH benzene, 5.26(2H,2N-CH-C)

3.2.1. Weight loss measurements

3.2.1.1. Effect of inhibitor concentration

The variation of inhibition efficiency with inhibitor concentrations is shown in Figure. 3.2.1(a), it is observed from figure that the inhibition efficiency increases as the concentration of inhibitors increases. The obtained results indicate that the corrosion inhibition efficiency of the DAPs is concentration dependent. The maximum inhibition efficiency was obtained for (DAP-1 showed 0maximum IE 98.5% among the three studied inhibitors at optimum concentration (40 mgL^{-1}). and no change observed in inhibition efficiency above this concentration, thus it was chosen as optimum. The superior performance of DAP-1 is attributed to the presence of electron donating methyl group and the low IE of DAP-3 is due to presence of electron withdrawing NO_2 group. Groups play important role in the inhibition efficiency [Wadhwani *et al.* (2015)]. The increase in IE is attributed to increase in the extent of surface coverage by the inhibitor molecules on the metal surface.

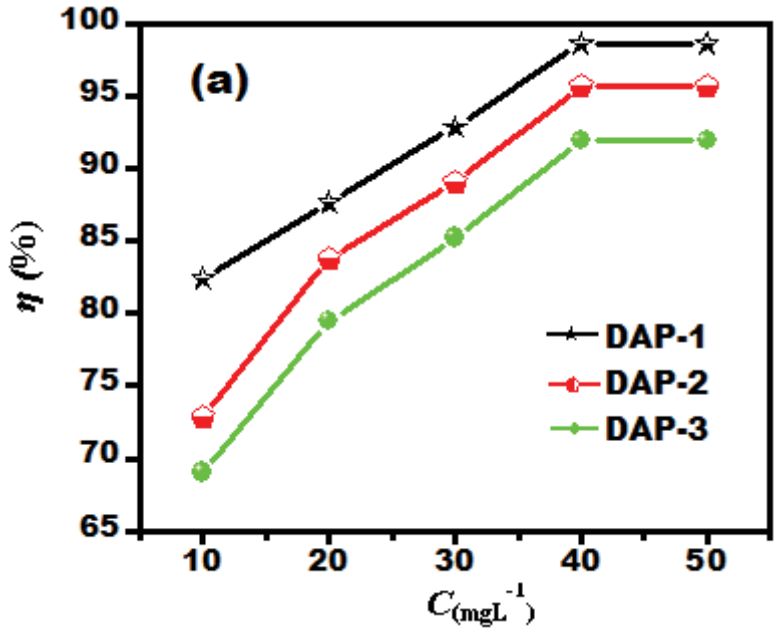

Figure.3.2.1: (a) Variation of the inhibition efficiency ($\eta\%$) with inhibitor concentration at 308 K

Table 3.2.2: gravimetric measurements (±SD) for MS in the Absence and Presence of DAPs in 1 M HCl at 308 K

Inhibitor	Conc (mgL^{-1})	C_R $mg\ cm^2h^{-1}$	Sur.cov (θ)	(η) %
Blank	--	7.00(0.03)	--	--
DAP-1	10	1.23 (0.01)	0.823	82.3
	20	0.86(0.01)	0.876	87.6
	30	0.50(0.02)	0.928	92.8
	40	0.10(0.02)	0.985	98.5
	50	0.10(0.02)	0.985	98.5
DAP-2	10	1.90(0.010	0.728	72.8
	20	1.13(0.01)	0.838	83.8
	30	0.76(0.03)	0.890	89.0
	40	0.30(0.03)	0.957	95.7
	50	0.30(0.03)	0.957	95.7
DAP-3	10	2.16 (0.03)	0.690	69.0
	20	1.43(0.02)	0.758	75.8
	30	1.33(0.12)	0.852	85.2
	40	0.56(0.14)	0.919	91.9
	50	0.56(0.14)	0.918	91.9

3.2.1.2. Effect of temperature

The variation in inhibition efficiency with temperature (308-338K) is shown in Figure. 3.2.1(b). From Figure 3.2.1(b), it is seen that I.E of the DAPs decrease with increase in temperature. The decrease in I.E is due to partial desorption of inhibitors molecule from the metal surface [Dohare *et al.* (2017**(a)**].

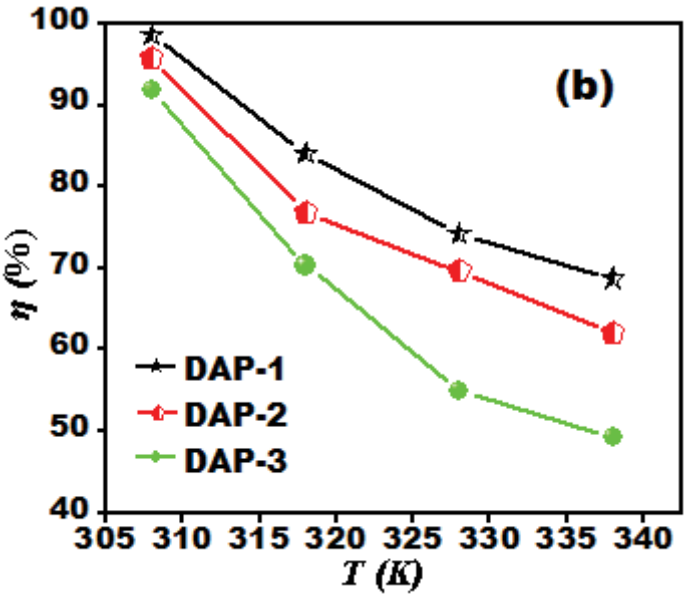

Figure.3.2.1: (b) Variation of inhibition efficiency ($\eta\%$) with solution temperature (308–338 K) at optimum concentration of inhibitor DAPs

3.2.1.3. Thermodynamic Parameters

The values of ΔS^* and ΔH^* were calculated from the plot of log C_R / T vs $1/T$ with a slope of ($\Delta H^* / 2.303R$ and an intercept of [log (R / Nh) + ($\Delta S^* / 2.303R$)] is straight line in both in absence the presence of inhibitor. The values of ΔH^* and ΔS^* are given in Table 3.2.3. Positive sign of ΔH^* reflected the endothermic nature of mild steel dissolution process, which suggested the slow dissolution of mild steel [Dohare *et al.* (2017) **(b)**]. The positive ΔS^* meaning that an increase in disordering takes place in going from reactants to the activated complex on metal/solution interface [Kumar *et al.* (2015)], which is driving force for the adsorption. The activation energies (E_a) values were calculated by plotting a graph between log C_R and $1/T$ at an optimum concentration of inhibitors and are shown Figure 3.2.1(c). The calculated values of E_a for in the absence and presence of inhibitor molecules are shown in Table 3.2.3 (Thermodynamic parameters for the adsorption of inhibitor on mild

steel in 1M HCl at optimum concentration (40 mgL^{-1}) DAPs). On the inspection of Table 3.2.3**,** the value of activation energy is higher in the presence of inhibitor than in the absence of the inhibitors is because of the inhibitors increase in the physical energy barrier associated with the corrosion reaction. The higher activation energy and decrease in the corrosion rate might be due to the formation of protective film of inhibitors on the metal surface [Zhang *et al.* (2009)].On inspection of Table 3.2.3, In the presence of DAPs, E_a and ΔH^*values change in a similar manner, which verify the known thermodynamic relationship between E_a and ΔH^*. Table 3.2.3 shows the ΔS^* values for uninhibited is large and negative and for the inhibited DAPs molecules it is large and positive. This variation is observed due to the disordering and ordering of the DAPs molecules on the mild steel surface. The higher value for the ΔS^* in the presence of inhibitors than the absence of inhibitors is due to the adsorption of DAPs molecules from the 1M HCl solution which may be due to the quasisubstitution process between the DAPs molecules in the aqueous phase and the water molecules in the mild steel surface [Guan et al (2004)], [Sahin *et al.* 2002)], [Larabi *et al.* (2005)]. By which the adsorption of DAPs molecule and desorption of water molecules from the mild steel surface.

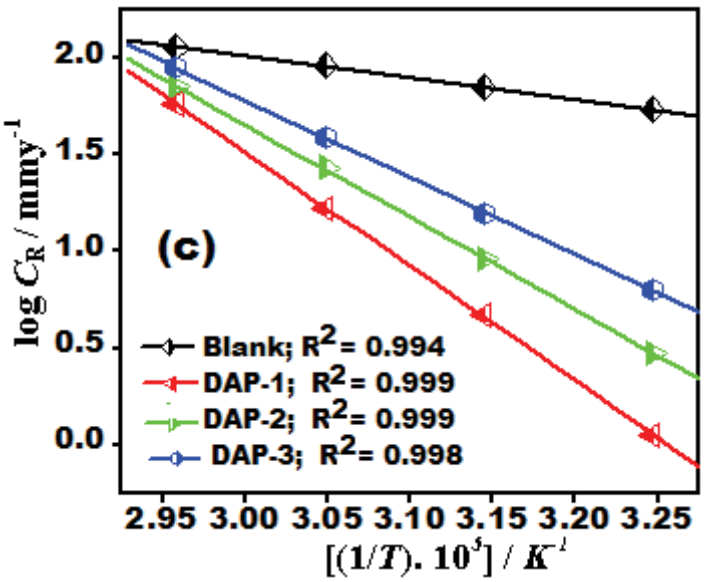

Figure.3.2.1(c) Arrhenius plots of the corrosion rate (C_R) of MS in 1 M HCl in the absence and presence of optimum concentration of DAPs;

Table 3.2.3: Thermodynamic parameters for the adsorption of inhibitor on mild steel in 1 M HCl at optimum concentration (40 mgL^{-1}) of DAPs at 308 K

Inhibitor	K_{ads} (10^4 M^-	$-\Delta G^\circ_{ads}$ (kJ mol^{-1})	E_a (kJ mol^{-1})	ΔH^* (kJmol^{-1})	ΔS^* (JK^{-1} mol^{-1})
Blank	----	----	28.74	24.89	-149.17
DAP-1	5.8	40.16	117.38	111.0	116.2
DAP-2	3.4	39.19	113.38	89.61	54.58
DAP-3	1.3	38.67	91.17	73.35	8.63

3.2.1.4 Adsorption isotherm

In order to understand the behaviour of DAPs on mild steel in 1M HCl, various adsorption isotherms namely Langmuir, Temkin and Frumkin were tested and calculated. Langmuir adsorption isotherm was found to be best fit among the studied isotherms. A straight line was observed by plotting a graph between $\log C_{inh}/\theta$ vs. C_{inh} as shown in Figure 3.2.1 (d), which

suggested the adsorption of inhibitor molecules on the metal surface obeys Langmuir adsorption isotherm. The values of K_{ads} and $\Delta G^{o}_{(ads)}$ are reported in Table 3.2.3. The calculated values of K_{ads} and ΔG^{0}_{ads} are given in Table 3.2.3. Generally, the higher value of K_{ads} is associated with strong adsorption and higher inhibition. In our present study, the value of K_{ads} obeys the order: DAP-1 >DAP -2 >DAP -3 which is accordance with the order of inhibition efficiency. The value of ΔG^{0}_{ads} for the present study varies from -38.17 to -40.16 kJ mol^{-1}, suggesting that the adsorption of inhibitors on the mild steel surface is by mixed mode [Hu *et al.* (2016)], [Solmaz (2014)].

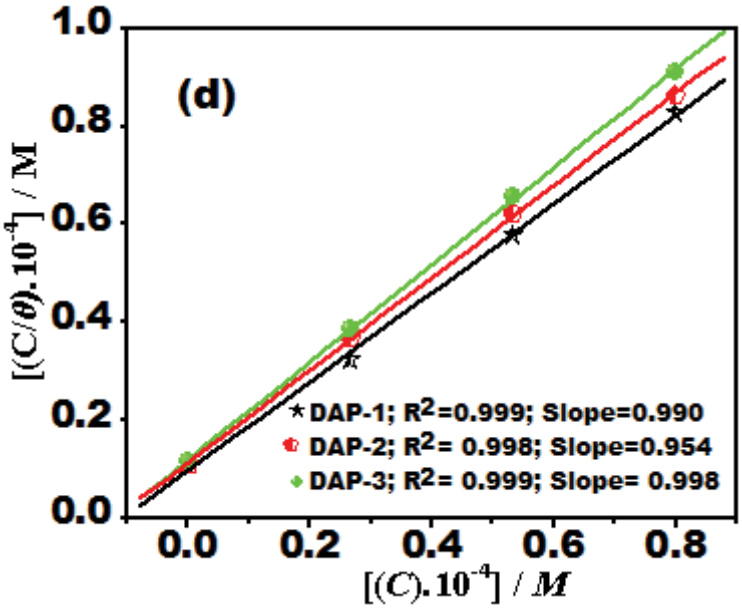

Figure.3.2.1 (d) Langmuir isotherm plot for adsorption of DAPs

3.2.2. Electrochemical impedance spectroscopy

The Nyquist plots were obtained for mild steel in 1M HCl without and with the optimum concentration (40mgL^{-1}) of the inhibitors are shown are Figure 3.2.2(a): The Nyquist plots are slightly depressed semi-circular shape; this feature is may be due to the different factors like surface roughness, discontinuity in the electrodes, impurities and the inhibitors

adsorption on the electrode surface. The shapes of uninhibited and inhibited mild steel in 1M HCl are same which suggest that DAPs reduce corrosion without changing the mechanism of corrosion [John *et al.* (2013)], [Daoud *et al.* (2014)], [Ehsani *et al.* (2014)]. The Figure 3.2.2(a) shows that the addition of DAPs increases the diameter of semicircle which signifies that corrosion is control by the charge transfer process and inhibition is attributed to the formation of protective film on mild steel surface. The fitted Nyquist plots of DAPs are shown in the Figure 3.2.2(c-e).

The equivalent circuit model is shown in Figure 3.2.2(b). The EIS data are tabulated in Table 3.2.4 shows that the R_p value increases with the increasing inhibitor concentration, which indicates the enhancement of surface resistance by the inhibitor molecules and the increasing inhibition of mild steel corrosion [Ehteshamzadeh *et al.* (2009)]. However the CPE values decrease with the increase in inhibitor concentration due to adsorption of inhibitor molecules on the metal surface [Moradi *et al.* (2013)]. The increase in the R_p value for the inhibited system is due to the formation of the protective film on the metal / solution interface [Bentiss *et al.* (2000)]. The value of C_{dl} decreases with increasing concentration of DAPs due to the decrease in local dielectric constant or an increase in the electrical double layer thickness at the metal surface [Tang *et al.* (2013)]. The imperfect semicircle of the Nyquist plots has been related to the deviation of n from unity (surface inhomogeneity), that is, the pure capacitive behaviour could not be achieved due to surface inhomogeneity caused by interfacial and structure origin. The double layer is usually considered as a constant phase element (*CPE*) rather than a pure capacitor. The values of "n" resulted in Table 3.2.4, which varies from 0.799 to 0.816 in the presence of the inhibitors, which is comparatively higher

than that of the blank, suggesting that surface heterogeneity decreases in the presence of inhibitors due to formation of protective film on the steel surface [verma *et al.* (2015) **(b)**].

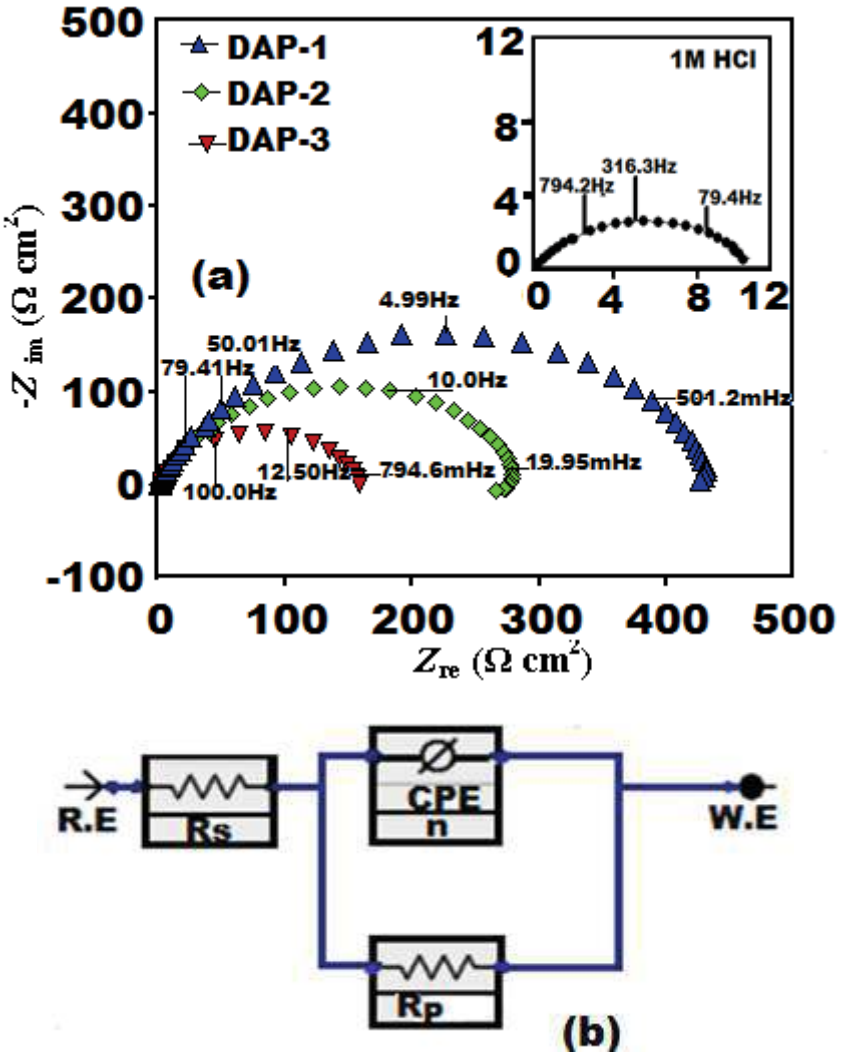

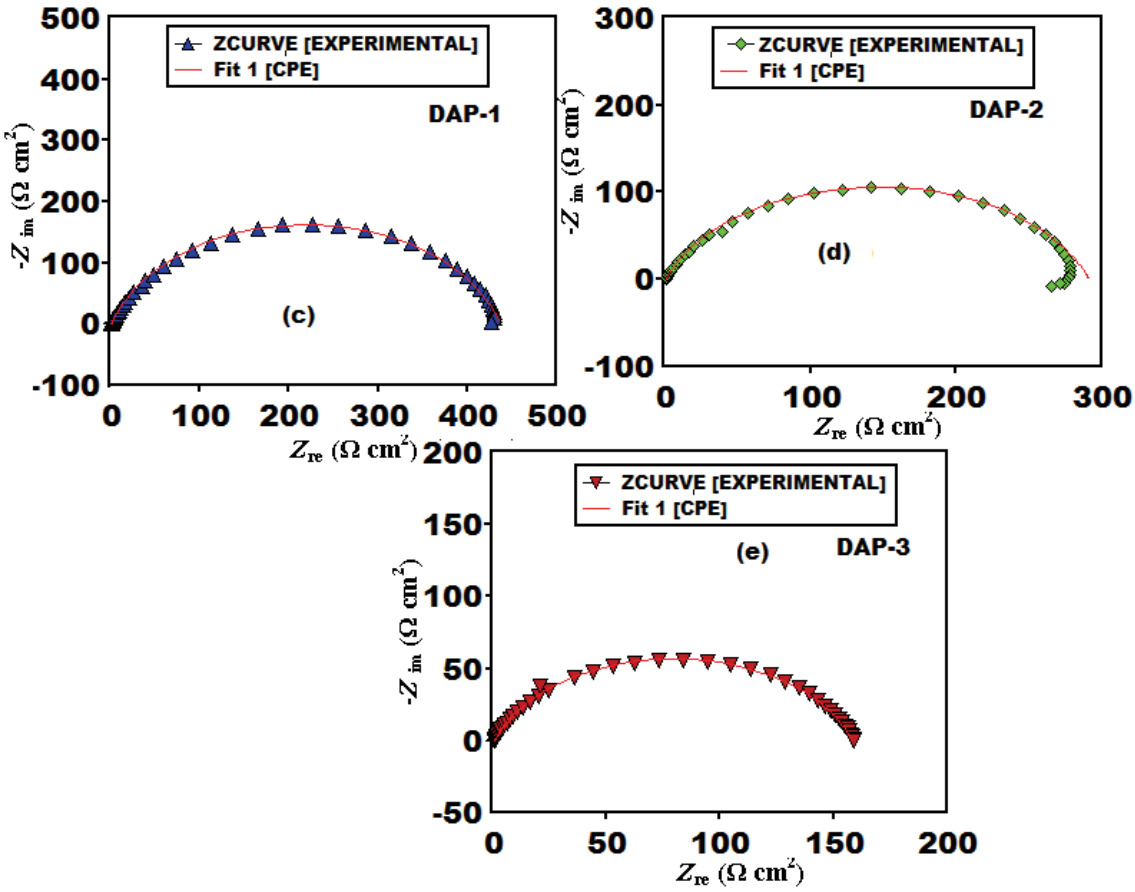

Figure 3.2.2:(a) Nyquist plots for the mild steel at optimum concentration of inhibitors DAP at 308 K; (b) Equivalent circuit model used to fit the EIS data; (c) (d) (e) fitted Nyquist plot for DAP-1, DAP-2, DAP-3 respectively

Bode plots are shown in Figure 3.2.3(f). It is seen that Bode plots involve only one phase maximum revealing that corrosion process takes place in one step, which corresponds to one time constant [Naderi *et al.(*2009)]. It is also seen that from Fig 3.2.3(f) that phase angle values is less than-90^{o}, which signified the non ideal behaviour of capacitor. The more negative value of phase angle and the high value of absolute impedance in the presence of DAPs indicate the superior performance of DAPs [Quraishi *et al.* (2007)], [Umoren *et al.* (2014)].The fitted Bode plots of DAPs are shown in the Figures 3.2.3(g-i).

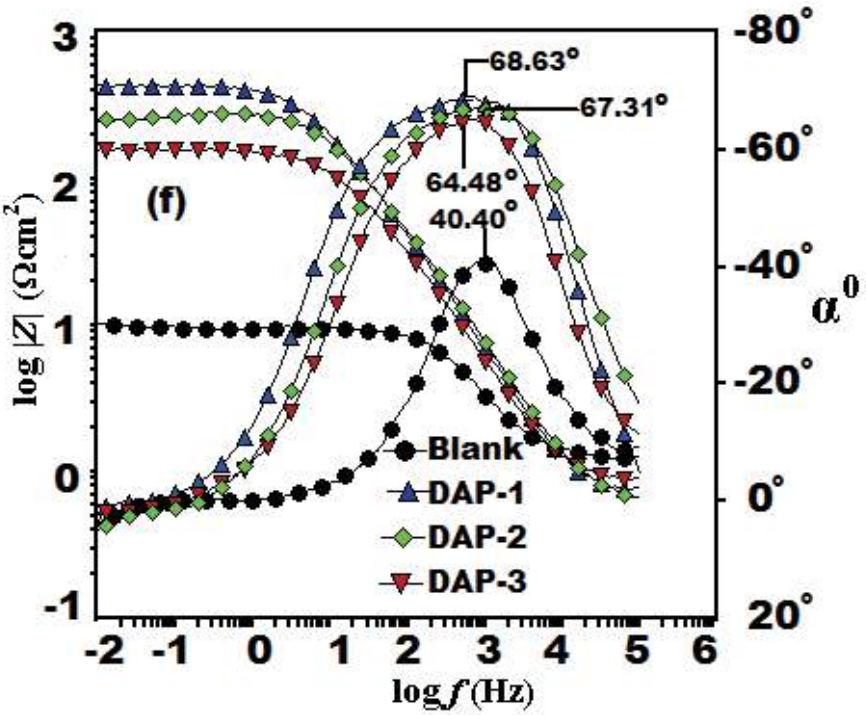
(f)
68.63°
67.31°
64.48°
40.40°
Blank
DAP-1
DAP-2
DAP-3
log |Z| (Ωcm²)
α⁰
log f (Hz)

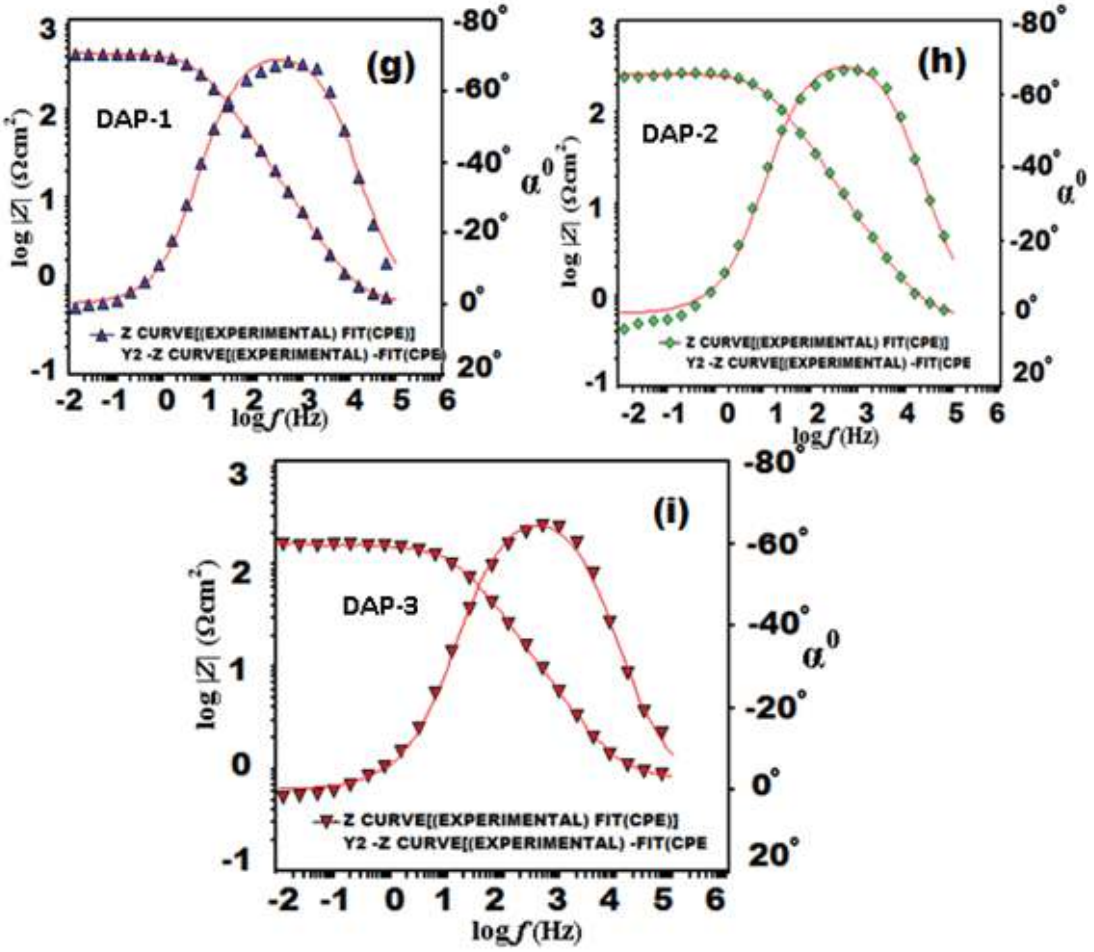
(g)
DAP-1
(h)
DAP-2
(i)
DAP-3
Z CURVE[(EXPERIMENTAL) FIT(CPE)]
Y2 -Z CURVE[(EXPERIMENTAL) -FIT(CPE
log |Z| (Ωcm²)
α⁰
log f (Hz)

Figure 3.2.2: (f) Bode (log f vs log |Z|) and phase angle (log f vs α) plots of impendence spectra for MS in 1 M HCl in the absence and presence of different concentrations of DAP at 308 K. (g) (h) (i) fitted bode plots for DAP-1, DAP-2, DAP-3 respectively.

Table 3.2.4: Electrochemical impedance parameters (±SD) for mild steel in 1M HCl in absence and presence of optimum concentration (40 mg L^{-1}) of DAPs at 308K

C_{inh} (mgL^{-1})	R_s (Ω)	R_p (Ω cm^2)	n	Y_0 (μFcm^{-2})	C_{dl} (μFcm^{-2})	η (%)
Blank	1.02(0.02)	7.4 (0.05)	0.798	481.2	137.9	----
DAP-1	0.65(0.02)	433.3(0.03)	0.816	120.7	52.35	98.0
DAP-2	0.56(0.02)	217.7 (0.05)	0.805	125.7	75.04	96.1
DAP-3	0.78(0.02)	157.0 (0.03)	0.799	174.8	104.9	94.5

3.2.3. Potentiodynamic polarizations study

The potentiodynamic polarisation plots (PDP) for MS in 1M HCl in the absence and presence of DAPs at the optimum concentration 40mgL^{-1} are shown in Figure 3.2.3. The calculated PDP parameters are given in Table 3.2.5. Figure 3.2.3, clearly shows that on addition of DAPs, causes reduction of i_{corr} without causing significant change in E_{corr}, thereby suggesting that all DAPs are good corrosion inhibitors and act as mixed inhibitors [Rehim *et al.* (2008)].The parallel cathodic Tafel lines (Figure. 3.2.3) suggests that the addition of inhibitors does not modify the mechanism of corrosion reaction [Poornima *et al.* (2011)]. On addition of the DAPs, the values for both anodic and cathodic Tafel slopes (β_a , β_c) slightly change, which indicates that the addition of the inhibitor reduces the anodic dissolution of

mild steel as well as retards the cathodic hydrogen evolution reaction, without affecting the reactions mechanism[Yadav *et al.* (2010)].

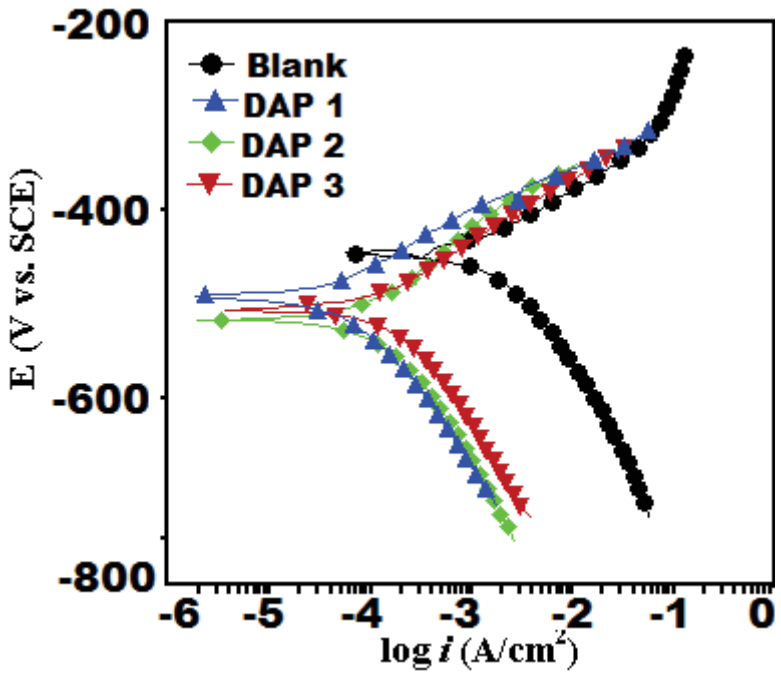

Figure 3.2.3: Polarization curves for corrosion of mild steel in absence and presence of optimum concentrations of inhibitors

Table 3.2.5: Potentiodynamic polarization parameters (±SD) for mild steel in 1M HCl in absence and presence of optimum concentration (40 mg L^{-1}) of DAPs at 308K

Inhibitor	E_{corr} (mV/SCE)	i_{corr} (μA/cm^2)	β_a (mV/dec)	β_c (mV/dec)	η (%)
Blank	-445	1320(0.03)	74.6	123.9	--
DAP-1	-492	29.3(0.02)	64.4	105.6	96.7
DAP-2	-517	79.8(0.02)	109.1	149.6	91.0
DAP-3	-505	109.4(0.03)	86.1	139.3	87.7

3.2.4. Surface analysis

For the surface characterization scanning electron microscopy (SEM) and atomic force microscopy (AFM) techniques become most powerful tool for analyzing the of corrosion surface related specimen. From the SEM, The morphology of the metal surface and the accumulation of the corrosion products on the metal can be examined. Figures3.2.4 (a-d) (SEM image of mild steel (a) Blank (b) DAP-1 (c) DAP-2 (d) DAP-3) respectively shows the SEM image of uninhibited and inhibited mild steel samples in 1M HCl for 24 h of the immersion period at the optimum concentration ($40mgL^{-1}$) of the inhibitors. The surface of the uninhibited mild steel specimen is highly corroded due to acid attack but in the presence of the inhibitors the surface is relatively smooth.

The AFM analysis was performed on steel surface after the immersion of samples in acid solutions up to 24 h. The micrograph of the mild steel samples in the absence and the presence of the inhibitors at the optimum concentration ($40mgL^{-1}$) are shown Figure3.2.5(a-d) (AFM image of mild steel (a) Blank (b) DAP-1 (c) DAP-2 (d) DAP-3) respectively. The micrograph of the mild steel surface in absence of inhibitor is 400 μm and in presence of inhibitors there is a significant improvement in the smoothness due to the adsorption of the inhibitors on the metal surface. The calculated average roughness for DAP-1 and DAP-2, and DAP-3 are 0.6μm, 5.2μm, 10.0 μm respectively.

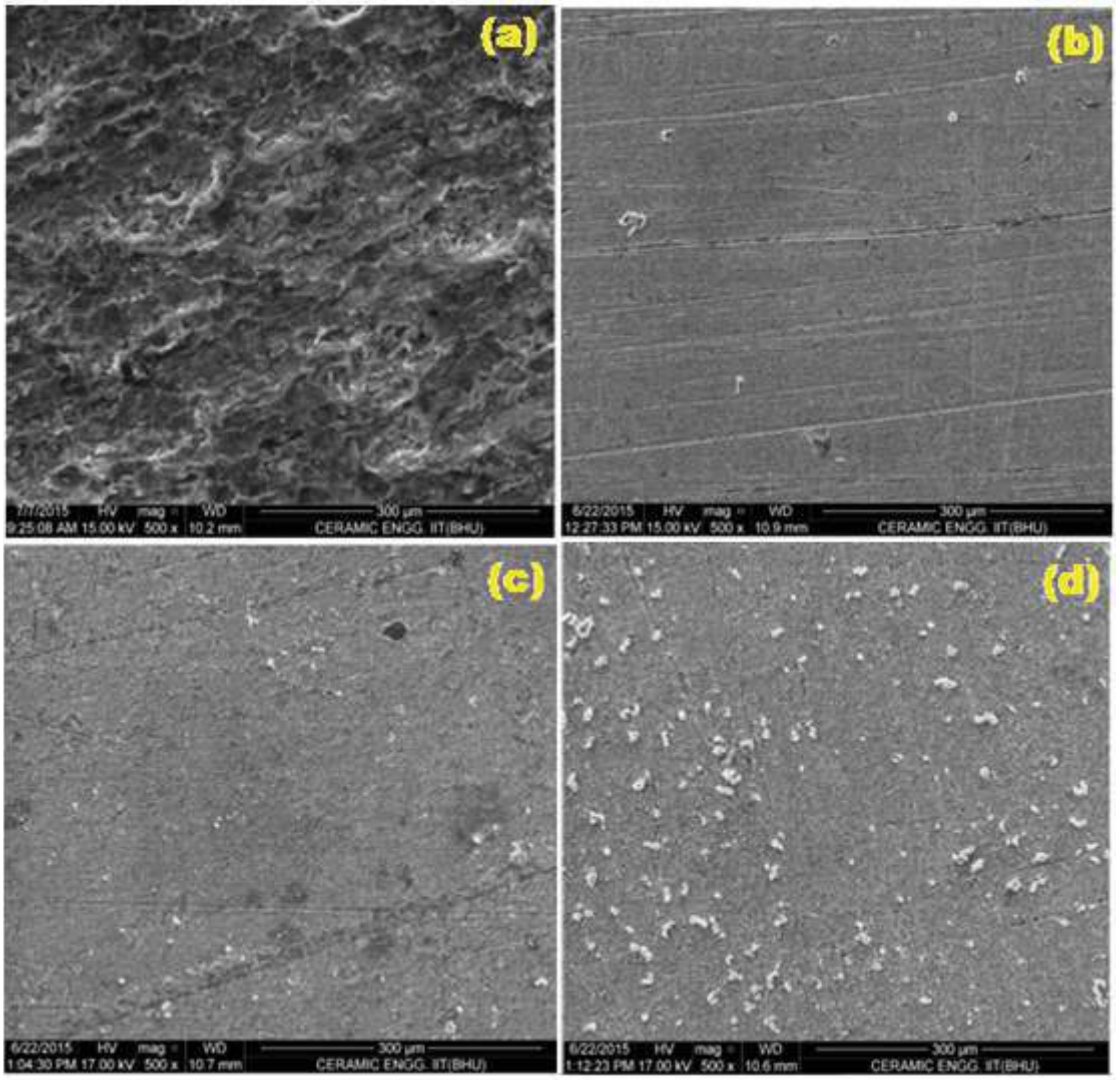

Figure 3.2.4: SEM image for (a) Blank (b) DAP-1 (c) DAP-2 (d) DAP-3

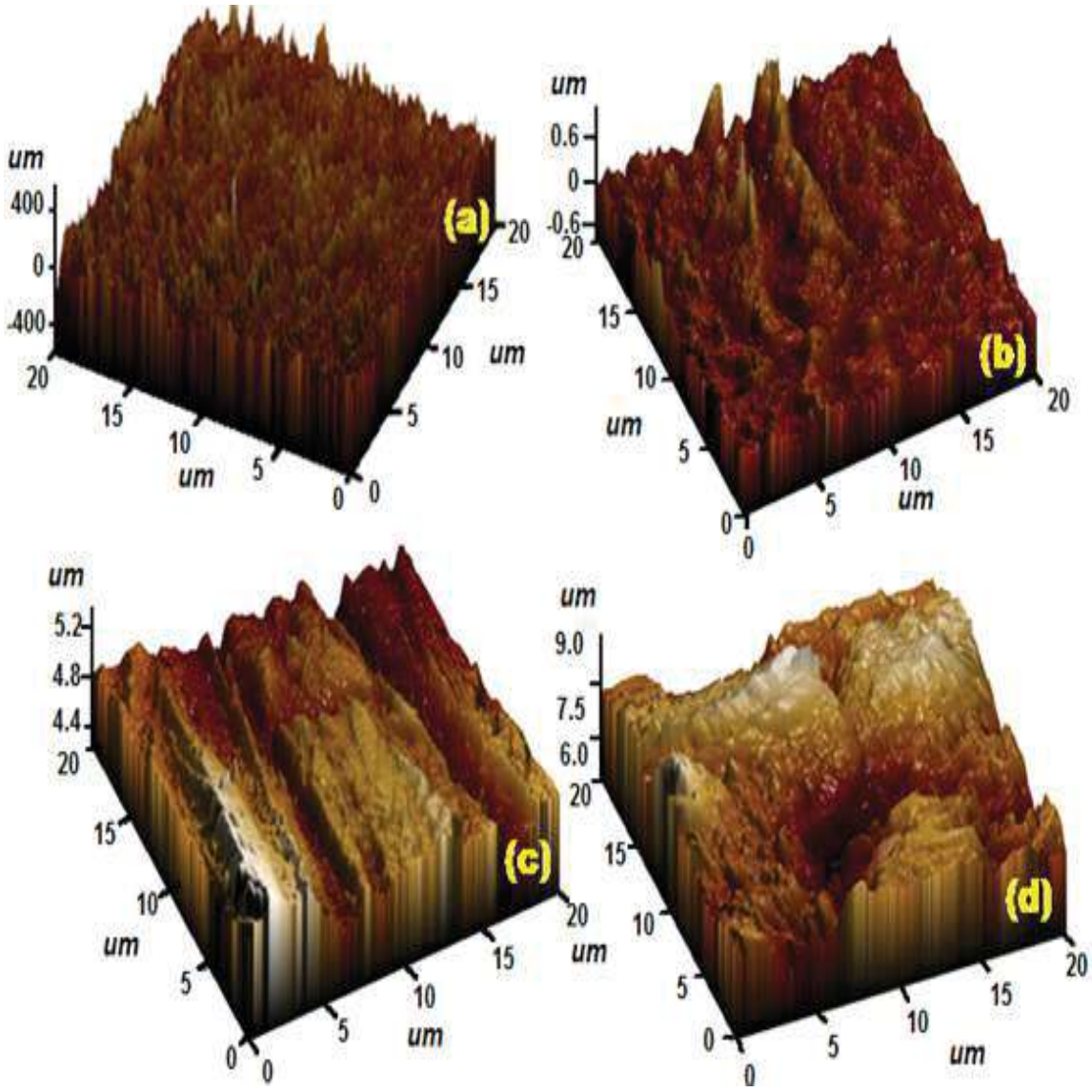

Figure 3.2.5: AFM images for (a) Blank (b) DAP-1 (c) DAP -2 (d) DAP -3

3.2.5. Quantum chemical calculations

3.2.5.1. Quantum chemical calculations of neutral inhibitor molecules

Figure 3.2.6 shows the (Optimized structure, HOMO, LOMO, electrostatic potential map (ESP) of neutral inhibitor molecules DAP-1, DAP-2, DAP-3 respectively. Generally HOMO and LUMO represents the electrons donation and electron acceptor capacity of the molecules [Dutta *et al.* (2015)]. Molecules with higher value of E_{HOMO} (less negative) and lower value of E_{LUMO} (more negative) show more donor and acceptor tendency of electrons with

appropriate metal d-orbital, respectively [Olasunkanmi *et al.* (2016)], [Lu *et al.* (2012)].It can be seen that in case of neutral inhibitor molecules (DAP-1, DAP-2 and DAP-3), the HOMO, electrons are spread over the phenyl ring and nitrogen atoms of the diaminopyridine ring. The LUMO regions for DAP-1, DAP-2, the electron density is resides all over the ring and in the case of DAP-3, the electron density is spread over the phenyl ring, nitrogen atoms of the diaminopyridine ring and over the nitro group.

The calculated quantum parameters like E_{HOMO}, E_{LUMO}, ΔE (E_{LUMO} - E_{HOMO}) are listed in Table 3.2.6 (Calculated quantum chemical parameters for DAPs derived from the B3LYP/6-31+G (d, p) method). The difference in energy level (ΔE= E_{LUMO} - E_{HOMO}) is an important factor and considered in the evaluation of inhibition potential. Generally, higher the value of E_{HOMO} suggests the better donor performance of inhibitor molecules. Table 3.2.6, reveals that the value of E_{HOMO} for DAP-1 is larger than that of DAP-2 and DAP-3, which supports the order of inhibition efficiencies obtained experimentally. The highest E_{HOMO} value for DAP-1 is due to the presence of electron donating CH_3 group attached to phenyl ring while lowest E_{HOMO} is attributed to electron withdrawing NO_2 group. Furthermore, lowest value of E_{LUMO} suggests that DAP-1 has greater electron accepting capacity than DAP-2 and DAP-3.

Softness is also an important parameter which elucidates the adsorption ability of the inhibitor molecules. Higher the value of softness and lower value of hardness (η) is associated with the strong interaction with metal and the high IE. Table 3.2.6, that the softness of DAP-1 (1.061) is more than DAP-2 (0.970) and DAP-3 (0.869), and the hardness order as follows; DAP-3> DAP-2> DAP-1, which is according to the experimentally obtained I.E. The values of fraction of electrons transferred (ΔN) are reported in Table 3.2.7.

In is reported that electron transfer from inhibitor to metal takes place easily when the ΔN value is greater than 0 and less than i.e. ΔN> 0.62. Table 3.2.6 reveals that all the calculated ΔN values are positive and lower than 3.6, which suggests that the inhibitor molecules have strong tendency to donate electrons to the vacant d-orbital of metal.

3.2.5.2. Quantum chemical calculations of protonated inhibitor molecules

Figure 3.2.7 shows the (Optimized structure, HOMO, LOMO, electrostatic potential map (ESP) of protonated inhibitor molecules DAP-1, DAP-2, DAP-3. From the inspection of Table 3.2.6, it founds that the energy gap between E_{HOMO} and E_{LUMO} is less as compared to the neutral molecules after the protonation. Table 3.2.6 reveals that all the calculated ΔN values are negative, which means that the electron donation from inhibitor molecules to the metal surface is not possible. It is also noted that E_{LUMO} values of protonated inhibitors shift towards more negative side as compared to the neutral molecules, which suggests that the protonated inhibitors have higher electron accepting capability compared to the neutral molecules. Thus protonated molecules the bond formation between inhibitor and metal takes place by the acceptance of electrons by inhibitor molecules from metal.

3.2.6.1. Molecular electrostatic potential

The colour region for the electrophilic and the nucleophilic attack to know the reactivity of the inhibitors molecule is studied molecular electrostatic potential (MEP) [Zhao et al (2005)]. The MEP map of the inhibitors molecule is calculate by the B3LYP/6-31G (d, p) chk file for the neutral and the protonated inhibitors molecules and are shown in the Figures 3.2.6 and 3.2.7 respectively. In the MEP map, the colour region is lies in order of .red, green blue. The colour region from red to green for the nucleophilic attack, and the colour region for green to blue is for the electrophilic attack. The MEP For the neutral molecules the colour region is

lies in between red and green which are more susceptible for the electrophilic attack. In the MEP map of neutral inhibitors the most negative potential (red colour) are around the N3, N7 and N8 atoms of the di amino-pyridine ring. The MEP map for DAP-3 has larger colour range due to the NO_2 group attached on both side than the other two inhibitors. From the MEP map of protonated DAP-1, DAP-2 and DAP-3, the whole molecule ready for nucleophilic attack. The nitrogen atoms of (N3, N7 and N8) the diamino-pyridine ring are having the most positive potential (blue colour). But in the case of DAP-3, it have both nucleophilic and electrophilic region due to having NO_2 groups on the both side of the ring. The colour range for the protonated species is larger than the neutral species which is accordance to the experimental result

3.2.6.2 Fukui index analysis of neutral inhibitor

The fukuii indices f_k^+ and f_k^- predicts the most probable atomic sites of the electrophilic and the nucleophilic activities of the inhibitor molecules [Martinez (2003)]. Higher the value of f_k^+ suggests acceptance of electron from the metal. While higher the value of f_k^- sites suggests more interactions with the electron deficient species. The calculated Fukui indices are presented in Table 3.2.7. In the case of DAP-1, the most susceptible sites for electrophilic attacks and for electron acceptance (f_k^+) are C(1), C(5), C(9), C(10), C(12), C(14), C(16), C(18), C(20), C(21), N(8) and for nucleophilic (f_k^-) attack are C(1), C(2), C(5), C(6), N(7), N(8) and C(20) respectively. In case of DAP-2, the active sites for electrophilic attacks are C(1), C(5), N(8), C(9), C(10), C(12), C(15), C(16), C(17),C(19), C(21)and C(23) atoms while, the favourable sites for nucleophilic attack are C(1), C(2), C(4), C(5), C(10), C(14), C(20), and, N(8) atoms. Likewise, for DAP-3, the sites for electron acceptance are N(3), N(8), C(10), C(12), C(14), C(16), C(1), C(23), and N(23) atoms

whereas, C(1), C(2), N(7), N(8), C(9), and C(20), O(26), O(27), O(28) are the electron donating atoms.

The analysis of fukuii indexes reveals that 2, 6diamino-pyridine ring along the with the phenyl ring are the reactive sites and more responsible for donor-acceptor interactions and thus facilitate the adsorption of inhibitors over the metallic surfaces.

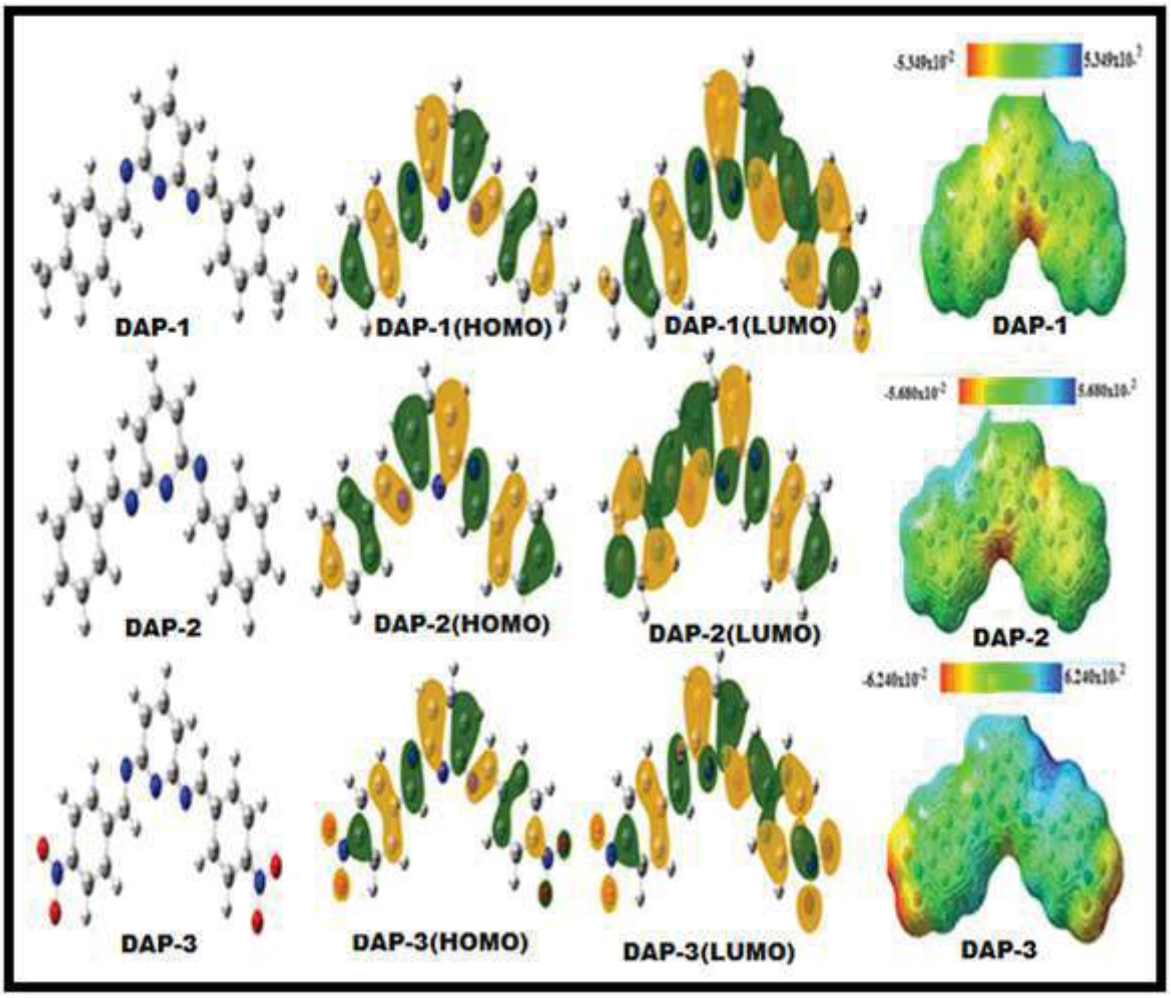

Figure 3.2.6: Optimized structure and Frontier molecular orbital's and ESP map for neutral inhibitors molecules (a-f) DAP-1 (b) DAP-2 (c) DAP-3

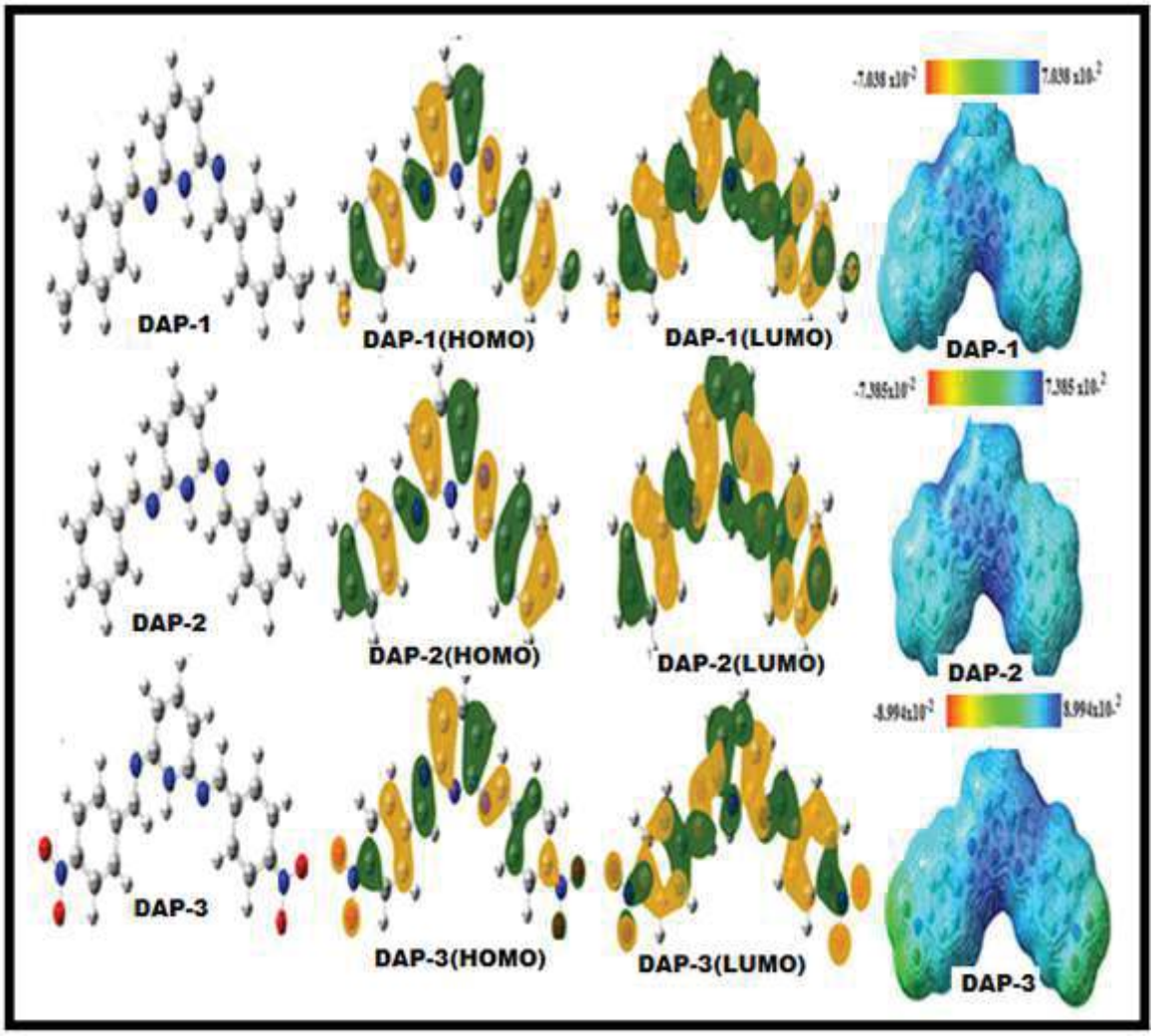

Figure 3.2.7: Optimized structure and Frontier molecular orbital's and ESP map for protonated inhibitors molecules (a-f) DAP-1 (b) DAP-2 (c) DAP-3

Table 3.2.6: Calculated quantum chemical parameters for DAPs derived from the B3LYP/6-31+G(d,p)method

Parameters→ Compounds↓	E_{HOMO} (eV)	E_{LUMO} (eV)	ΔE (eV)	η (eV)	$^{b}\sigma$ (eV^{-1})	$^{\Delta N}$ (eV)
In Neutral						
DAP-1	-4.216	-2.331	1.885	0.942	1.061	0.820
DAP-2	-4.223	-2.163	2.060	1.030	0.970	0.789
DAP-3	-4.312	-2.012	2.30	1.150	0.869	0.720
In Protonated						
DAP-1	-11.156	-5.881	5.275	2.637	0.379	-.701
DAP-2	-11.415	-5.579	5.836	2.918	0.342	-.630
DAP-3	-9.621	-5.105	4.516	2.258	0.442	-.563

Table 3.2.7: Calculated Fukui functions for the studied neutral inhibitor molecules

Atoms	DAP-1 f_k^-	DAP-1 f_k^+	DAP-2 f_k^-	DAP-2 f_k^+	DAP-3 f_k^-	DAP-3 f_k^+
C1	0.271	0.097	0.268	0.103	0.251	.0160
C2	.048	0.029	0.062	0.019	0.062	-.0018
N3	-.009	0.001	-.010	.0013	0.009	0.088
C4	0.035	0.007	0.043	0.013	0.043	0.022
C5	0.277	0.131	0.276	0.124	0.266	0.007
C6	0.042	0.004	-0.038	-.008	-0.037	0.008
N7	0.050	0.032	0.038	0.022	0.034	0.022
N8	0.060	-0.017	0.054	0.077	0.050	0.080
C9	0.054	0.138	0.066	0.093	0.067	0.030
C10	0.034	0.137	0.042	0.171	0.043	0.162
C11	0.016	-.0018	0.011	0.009	0.008	0.045
C12	0.022	0.0510	-.0238	0.064	0.023	0.073
C13	0.002	-.0034	-.0003	0.000	0.001	0.027

C14	0.041	0.0745	0.039	0.022	0.039	0.117
C15	-.002	-.0075	-.0038	0.077	-.0041	0.014
C16	0.023	0.0625	0.027	0.093	0.027	0.080
C17	0.021	0.0016	0.013	0.171	0.010	0.007
C18	0.030	0.059	0.032	0.0094	0.031	0.011
C19	0.0018	0.004	-.0012	0.064	-.0026	0.005
C20	0.055	-.0829	-.0523	0.000	0.051	0.019
C21	-0.002	0.0829	-.0045	0.098	-.0051	0.0018
C22	-0.009	0.0076	0.035	-0.007	0.035	0.013
C23	-0.010	0.0657	-.009	0.082	-.0022	0.038
C24	-0.000	-.0036	-.009	0.006	-.0029	0.006
N23	--	--	--	--	0.0058	0.057
N24	--	--	--	--	0.010	0.037
O25	--	--	--	--	0.007	0.009
O26	--	--	--	--	0.0130	0.006
O27	--	--	--	--	-.0096	-.0003
O28	--	--	--	--	-.0094	-.0001

3.2.7. Monte Carlo simulations

The adsorption behaviour of inhibitors molecules over the metal surface is shown in the Figure 3.2.8 in gas phase and aqueous phase for DAP-1, DAP-2, DAP-3 respectively. It is clearly seen that the orientation of the studied inhibitors molecular is in flat manner to the metal surface. The corresponding values for the outputs and descriptors are listed in Table 3.2.8. The parameters include total energy of the substrate–adsorbate configuration, which is defined as the sum of the energies of the adsorbate components, the rigid adsorption energy, and the deformation energy. The substrate energy (i.e., Fe (110) surface) is taken as zero. Moreover, adsorption energy reports the energy released (or required) when the relaxed adsorbate component was adsorbed on the substrate. The adsorption energy is defined as the

sum of the rigid adsorption energy and the deformation energy for the adsorbate component. The rigid adsorption energy reports the energy released (or required) when the unrelaxed adsorbate component (before the geometry optimization step) was adsorbed on the substrate. The deformation energy reports the energy released when the adsorbed adsorbate component was relaxed on the substrate surface. Finally, (dEad/dNi) reports the energy of substrate–adsorbate configurations where one of the adsorbate components has been removed.

From the Table 3.2.8, the large negative value adsorption energies suggest that the inhibitors molecule strongly adsorbs on to the on to the Fe (110) surface [Kaya et al. (2016)], [Obot *et al.* (2015)], [Ramaganthan *et al.* (2015)]. The maximum negative value of adsorption energy for DAP-1 (-2530.7) suggest that DAP-1 strongly adsorb on the metal surface than DAP-2 and DAP-3 -808.2, -691.3 in kJ/mol respectively. This follows the order of the inhibition efficiency obtained by the experimental methods. The order of the rigid adsorption energy is also according to the experimental results which are as follows: (-794.13), (-786.48), (692.66) for DAP-1, DAP-2, DAP-3 respectively. However, there is change in the regular trends in the deformation energy value. It does not follow the experimental result. DAP-3 has high adsorption energy than DAP-2 in aqueous phase from the Monte Carlo simulation result even though the reverse is the trend in inhibition efficiency. This is because of the presence of excess oxygen atoms in the NO_2 group which can bond strongly with water in a hydrogen type of bonding. (O---H). This increases the interaction of the inhibitor molecule with Fe surface. In the gas phase such hydrogen bonding interaction is not present, therefore the adsorption of DAP-2 is greater than DAP-3. This shows that in aqueous phase apart from adsorption of inhibitor on metal surface, many processes such as hydrogen bonding, protonation of inhibitor molecules in acid solution, pH of the solution etc can lead to a

discrepancy in simulation results. In order to get the real corrosive environment, it is necessary to conduct the MC simulations in the presence of water. Figure 3.2.8 shows the inhibitors (DAP-1, DAP-2, DAP-3) configuration in the aqueous phase. Table 3.2.8 reveals the adsorption energies values in the aqueous phase for studied inhibitors DAP-1, DAP-2 and DAP-3. It is generally noticed that the metal-inhibitors interaction is depicted by the adsorption mechanism. High negative adsorption energy values indicate the most stable and the stronger adsorption. On inspection of Table 3.2.8, we see that all the calculated values like total energies, adsorption energies, rigid adsorption energies and deformation energies are very high in the aqueous phase than the vacuum phase. This proves that the inhibitors is stable in the aqueous phase and strongly bind with the metal surface. All the calculated energies follows the order DAP-1> DAP-2> DAP-3 which is according to the experimental results. From the Table 3.2.8, (dE_{ad}/dNi) energy of the water from the metal surface gives the information on the ease of water removal on the metal surface which can protect the metal surface from the corrosive aqueous environment.

Table 9: Interaction energies between the inhibitors and Fe (110) surface (kJ/mol)

Inhibitors	**(Total energy) kJ/mol**	**Adsorption Energy kJ/mol**	**Rigid adsorption Energy**	**Deformation energy**	**dEad/dNi: Inhibitor'**	**dEad/dNi: H_2O**
(gas phase)						
DAP -1	-1030.8	-2530.79	-794.13	-1744.30	-2530.79	----------
DAP-2	-860.78	-808.20	-786.48	0.7238	-808.20	----------
DAP-3	-767.88	-691.93	-692.66	-14.07	-691.39	----------
(aqueous phase)						
DAP -1	-6325.20	-6082.86	-6324.36	241.50	-846.42	-24.01
DAP-2	-5921.07	-5745.38	-5988.39	243.00	-755.50	-28.91

DAP-3	-5965.29	-5989.77	-6249.34	259.53	-929.14	-44.22

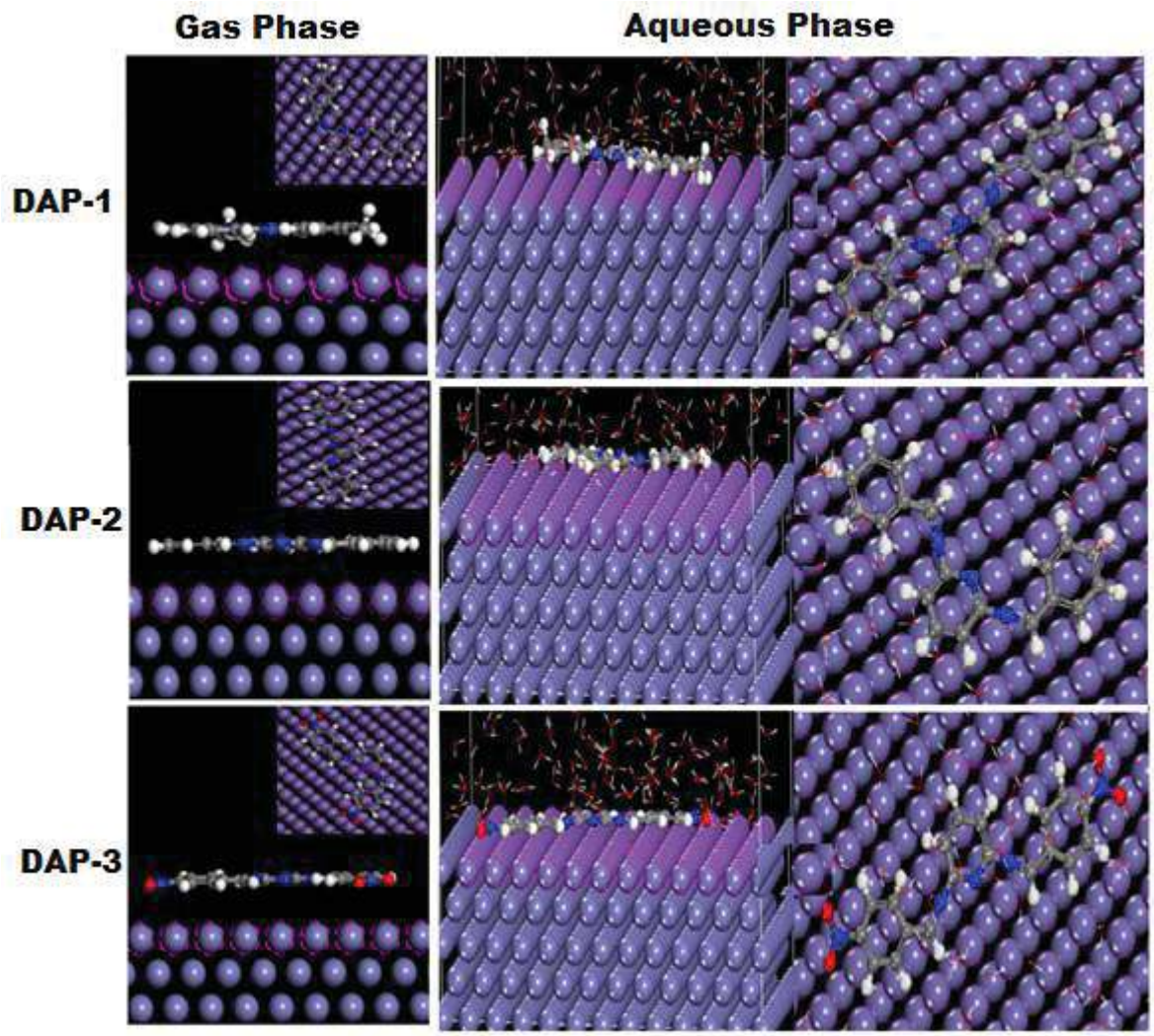

Figure.3.2.8: Side views and top views of the most stable configurations for adsorption of (a) DAP-1 (b) DAP-2 and DAP-3 on Fe (110) surface calculated using Monte Carlo simulations in gas phase and aqueous phase

3.3. Imidazole derivatives as corrosion inhibitors

Imidazole is a class of heterocyclic compounds which have attracted more attention because of their wide biological activities like analgesic, fungicidal, antitumor activities [Sathe *et al.* (2011)], [Roongpisuthipong *et al.* (2010)], [Sondhi *et al.* (2008)] and corrosion inhibition properties [El-Haddad *et al.* (2015)], [Xua *et al*. (2016)], [Li *et al* (2014)], [Negm *et al.*(2012)]. The non toxic nature and significant anticorrosion properties of imidazole derivatives have prompted us to investigate the corrosion inhibition properties of some new imidazoles derivatives. In view of this, we have synthesized, three substituted imidazoles namely 2, 3, 5 triphenyl imidazole derivatives namely 2-(3-methoxyphenyl)-4, 5-diphenyl-1H-imidazole (IM-1), 2,4,5-triphenyl-1H-imidazole (IM-2), and2-(3-nitrophenyl)-4,5-diphenyl-1H-imidazole (IM-3) to study their corrosion inhibition performance on mild steel corrosion in HCl using chemical and electrochemical methods. These inhibitors contain one imidazole ring, 2 nitrogen atoms, 3 phenyl rings, and one electron donating methoxy group. For surface characterization, scanning electron microscopy (SEM), atomic force microscopy (AFM) techniques have been used. The experimental results were supported by the quantum chemical investigation and MD simulations. The molecular structure and IUPAC name of the inhibitors used are given in Table 3.3.1.

Table 3.3.1: IUPAC name, molecular structure, abbreviation and analytical data of the studied inhibitor molecules (IMs)

Inhibitor	Inhibitor	Structure	Analytical data
1	2-(3-methoxyphenyl)-4,5-diphenyl-1H-imidazole (IM-1)	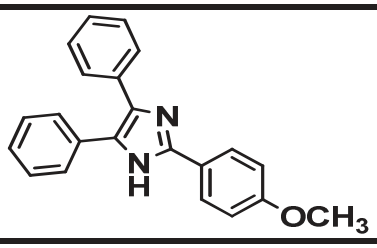	**$C_{22}H_{18}N_2O$;326.14;** Off white crystallinepowder; m.p= 190^oC
2	2,4,5-triphenyl-1H-imidazole	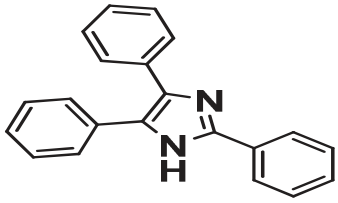	**$C_{21}H_{16}N_2$;** 296.13; Off white crystalline powder; m.p= 223^oC;
3	2-(3-nitrophenyl)-4,5-diphenyl-1H-imidazole (IM-3)	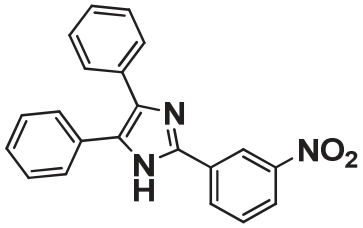	**$C_{21}H_{15}N_3O_2$; 341.12,** Pale yellow crystalline powder ; m.p= 321^oC;

3.3.1. Gravimetric measurements

3.3.1.2. Effect of Inhibitor concentration

The results obtained from the gravimetric measurements, such as, corrosion rates(C_R), corrosion inhibition efficiency(η%), are listed in the Table 3.3.2, which shows that on the addition of the different concentration of IM-1, IM-2 and IM-3, the inhibition efficiency increases and the corrosion rate decreases, which is attributed to the maximum surface coverage of metal by inhibiting molecules. The maximum inhibition efficiency observed, in the present case for IM-1- , IM-2- and for IM-3- 97.6%, 94.2%, 91.8% respectively at 100 mgL^{-1}. The inhibition efficiency profile is shown in the Figure 3.3.1. The difference on inhibition efficiency is attributed to the substituent's groups attached to the imidazole ring of

IM-1, IM-2 and IM-3(-OCH_3, -H, and NO_2) respectively. The IM-1 shows highest inhibition efficiency due to the presence of the electron releasing group (- OCH_3).

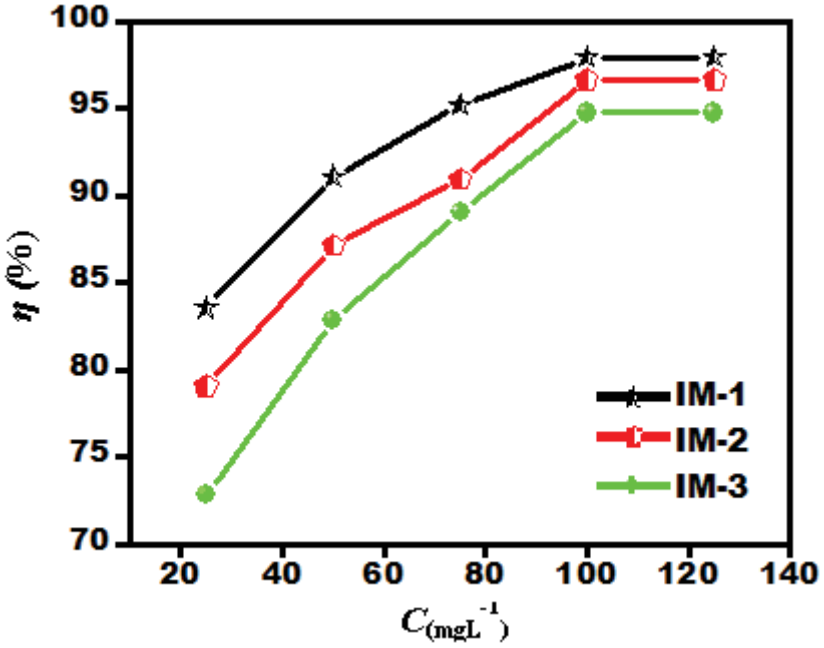

Figure 3.3.1 Variation of inhibition efficiency (η%) with inhibitor concentration at 308 K for MS in 1 M HCl.

Table 3.3.2: The weight loss parameters obtained for mild steel in 1 M HCl containing different concentrations of IMs

Inhibitor	Concentration (mgL^{-1})	C_R (mm/year)	sur.coverage (θ)	(η) %
Blank	--	77.91(0.03)	--	--
IM-1	25	5.565 (0.01)	0.928	83.5
	50	4.08 (0.01)	0.947	91.0
	75	2.59 (0.02)	0.966	95.9
	100	1.11 (0.02)	0.985	97.2
IM-2	25	8.90 (0.01)	0.885	79.0
	50	5.93 (0.01)	0.923	87.1
	75	4.08 (0.03)	0.947	90.9
	100	3.33 (0.03)	0.957	96.6
IM-3	25	10.0 (0.02)	0.871	72.8
	50	7.42 (0.03)	0.904	82.8
	75	5.93 (0.02)	0.923	89.0
	100	4.08 (0.03)	0.947	94.7

3.3.1.2. Effect of temperature

The variation of inhibition efficiency (IE) with solution temperature (308-338 K) at optimum concentration of IMs is shown in Fig. 3.3.2. It is clearly seen from the graph that, inhibition efficiency for all the studied imidazoles decreases upon the rise in the temperature. The decrease in inhibition efficiency may be attributed to desorption of IMs molecules from the metal surface at elevated temperature [Dohare *et al.* (2017**(a)**], [Chaubey *et al* (2017)].

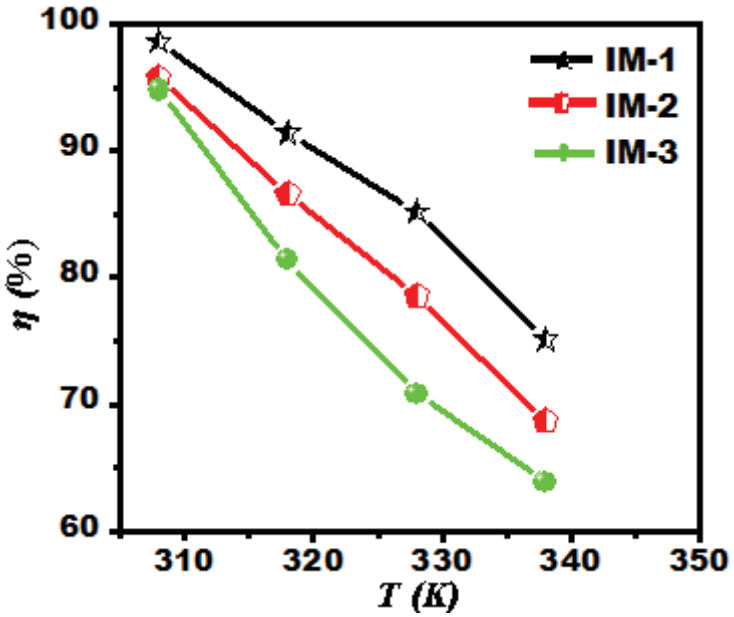

Figure 3.3.2: Variation of inhibition efficiency (η %) with solution temperature (308-338 K) at optimum concentration of IMs.

The temperature effect on corrosion rate (C_R) for mild steel in the absence and presence of IMs are shown in Fig 3.3.2. The values of ΔH^*, ΔS^*, activation energy (ΔE_a), K_{ads} and $\Delta G^o_{(ads)}$ are given in Table 3.3.3. The values of ΔG^0_{ads} varies from -41.84 to -38.59 kJmol^{-1}, signifying that inhibitors are adsorbed on mild steel surface by mixed mode mechanism, predominately by chemical mode of adsorption [Singh *et al*. (2017)].

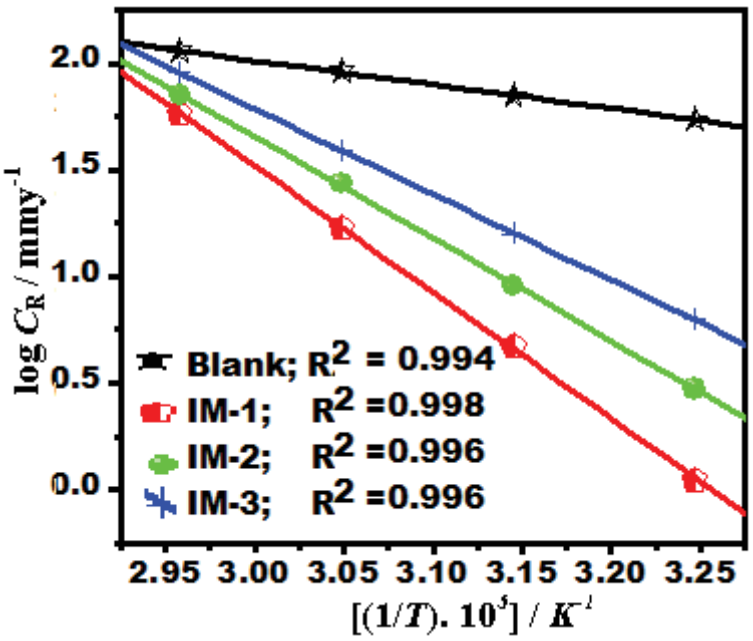

Figure 3.3.3: Arrhenius plots of the corrosion rate (C_R) of mild steel in absence and presence of optimum concentration of IMs

Table 3.3.3: Thermodynamic parameters for mild steel dissolution in 1M HCl in the absence and presence of optimum (100 mgL^{-1}) concentration of inhibitors

Inhibitor	K_{ads} (10^4 M$^-$	$-\Delta G^{\circ}_{ads}$ (kJ mol^{-1})	E_a (kJ mol^{-1})	ΔH (kJmol^{-1})	ΔS (JK^{-1} mol^{-1})
Blank	----	----	27.9	-18.60	-151.5
IM-1	10.4	41.84	113.39	111.04	116.24
IM-2	8.34	39.74	90.16	89.61	54.58
IM-3	6.76	38.51	76.66	73.35	8.63

3.3.4. Adsorption isotherm

Various adsorption isotherms, such as Frumkin, Langmuir, Temkin, and Flory–Huggins isotherms have been tested and for the present case, the best fitted adsorption isotherm is Langmuir adsorption isotherm which is shown in the Figure 3.3.4, because in this case the values of R^2 are most close to unity for all inhibitors whereas for Frumkin and Temkin isotherms, the values of R^2 were much apart from unity. The data calculated are given in the Table 3.3.4. Further, although the values of R^2 in Langmuir adsorption isotherm were close to one. However, slight deviation of the slope from unity indicated that the Langmuir isotherm could not be strictly applied.

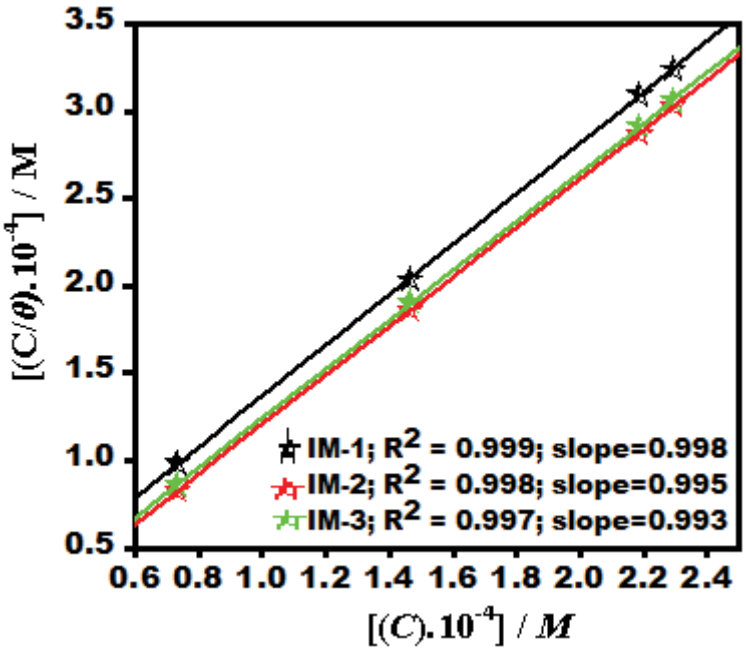

Figure 3.3.4: Langmuir adsorption isotherm plots

Table 3.3.4: Adsorption parameters for IMs calculated from the different isotherms for mild steel in 1M HCl solution.

Adsorption isotherm	Inhibitor	Correlation coefficient	Slope
Langmuir	IM-1	0.997	1.042
	IM-2	0.999	0.964
	IM-3	1.00	0.966
Temkin	IM-1	0.998	0.737
	IM-2	0.996	0.825
	IM-3	0.994	0.872
Frumkin	IM-1	0.822	0.882
	IM-2	0.981	0.373
	IM-3	0.415	0.441
Flory & Huggins	IM-1	0.265	0.623
	IM-2	0.327	0.543
	IM-3	0.328	0.601

3.3.5 Electrochemical impedance spectroscopy (EIS) study

The Nyquist plots obtained for mild steel in 1 M HCl in the absence and presence of the studied inhibitors IMs at the optimum concentration 100mgL^{-1} are shown in Figure 3.3.5 (a). And the fitted Nyquist plots for IMs molecules are given in Figure 3.3.5 (c-e), fitted Nyquist plots for the IM-1, IM-2, and IM-3 at optimum concentration respectively). On careful examination of Nyquist plots (Figure. 3.3.5(a), reveals that the diameter of capacity loop is higher in the presence of the imidazoles than in their absence which indicate that the corrosion of mild steel in 1M HCl solution is controlled by polarization resistance [Yıldız *et al* (2015)], [Youse *et al* (2015)]. EIS data were analyzed using equivalent circuit Fig 3.3.5

(b). On the inspection of Table 3.3.5 shows that on increasing the inhibitor concentration R_p increases due to the formation of protective film on the metal surface[Solmaz, *et al* (2008)], and the value of C_{dl} decreases which is attributed to increase in electrical thickness of electrical double layer on metal/solution interface. Or decrease in the local dielectric constant. Table 3.3.5, It is seen that the inhibition efficiency of the IMs molecules is as follows the order as; IM-1> IM-2> IM-3. EIS results depicted in Table 3.3.5 revealed that the value of "n" for the present case lies in between 0.798 to 0.830 which signifies that *CPE* behaves as non ideal capacitances.

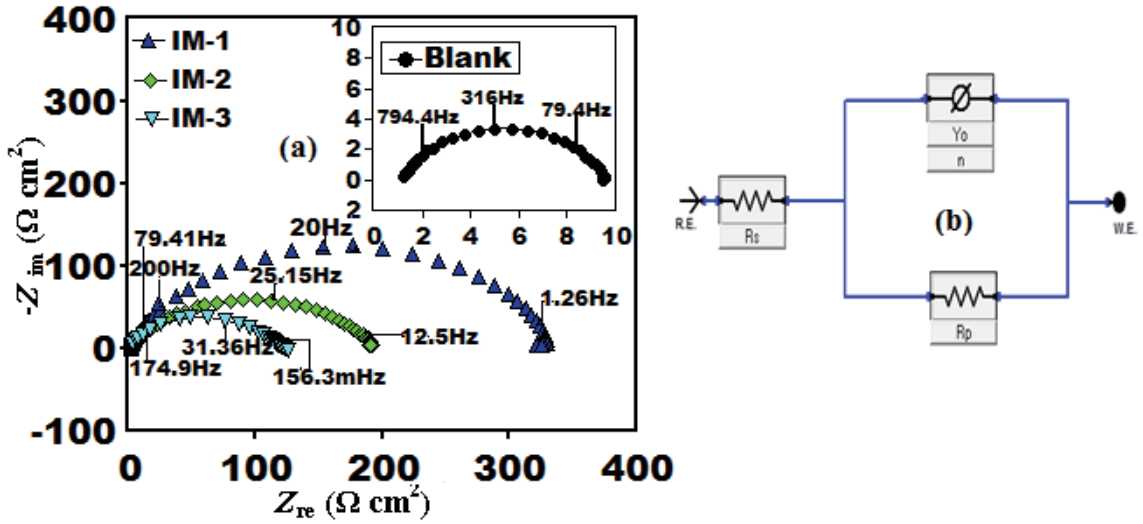

Figure 3.3.5 (a): Nyquist plots for the mild steel at optimum concentration of IMs.

Figure 3.3.5 (b): Equivalent circuit model used to fit the EIS data

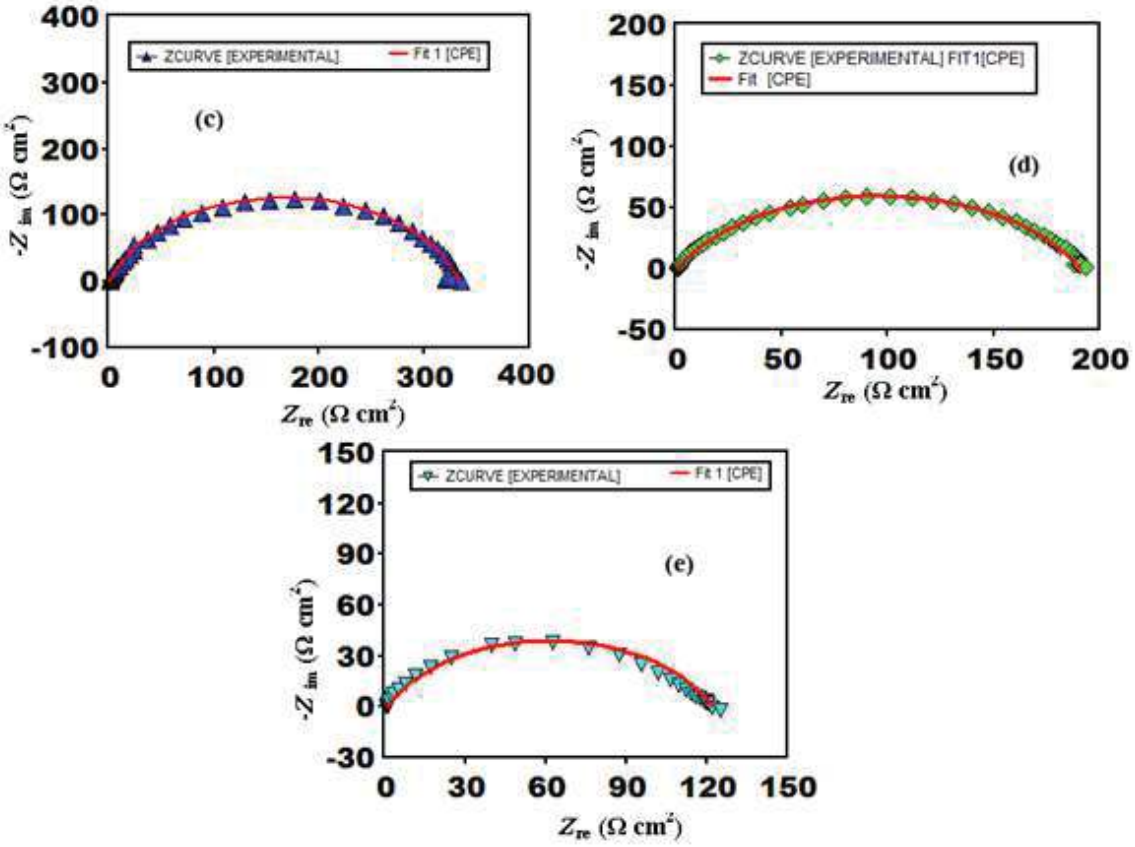

Figure 3.3.5: (c, d, e): fitted Nyquist plots for the IM-1, IM-2, and IM-3 at optimum concentration respectively

Table 3.3.5: Electrochemical impedance parameters (±SD) for mild steel in 1M HCl in absence and presence of optimum concentration (100 mg L^{-1}) of inhibitors

C_{inh} (mgL^{-1})	R_s (Ω)	R_p (Ω cm^2)	n	Y_0 ($\mu F/cm^2$)	C_{dl} ($\mu F/cm^2$)	η (%)
Blank	1.02(0.02)	7.44 (0.05)	0.798	481.2	137.9	----
IM-1	0.650 (0.02)	332.9(0.03)	0.830	131.6	39.8	97.45
IM-2	0.564(0.02)	187.2 (0.05)	0.768	126.7	44.9	95.46
IM-3	0.739(0.02)	121.7(0.03)	0.724	185.3	57.7	93.00

Fig 3.3.5(f) represents Bode plot for uninhibited and inhibited mild steel specimen. The fitted Bode plots for IMs are given in the Fig 3.3.5 (g-i) in absence and presence of optimum concentration of IM-1, IM-2, and IM-3 respectively at 308 K). Generally for the ideal capacitor slope and the phase angle (α^0) values should be -1 and -90^0 respectively. However, in present case the corresponding values of slope and the phase angles are as follows: -0.503, -40.780 for blank, -0.825, -71.240 for IM-1, -0.739, -70.000 for IM-2, and -0.733, -62.940 for IM-3. This deviation in slope and phase angle is due to surface heterogeneity resulted due to structural and interfacial origin [Verma, *et al.* (2015)], [Singh *et al.* (2015)]. However, in presence of IMs (Fig.3.3.5 (f) values of phase angles have been enhanced indicating significant improvement in the surface smoothness due to the formation of protective film of imidazoles over the metallic surface which protects metal surface from corrosion[Yadav *et al.* (2012)], [Umoren *et al.* (2010)].

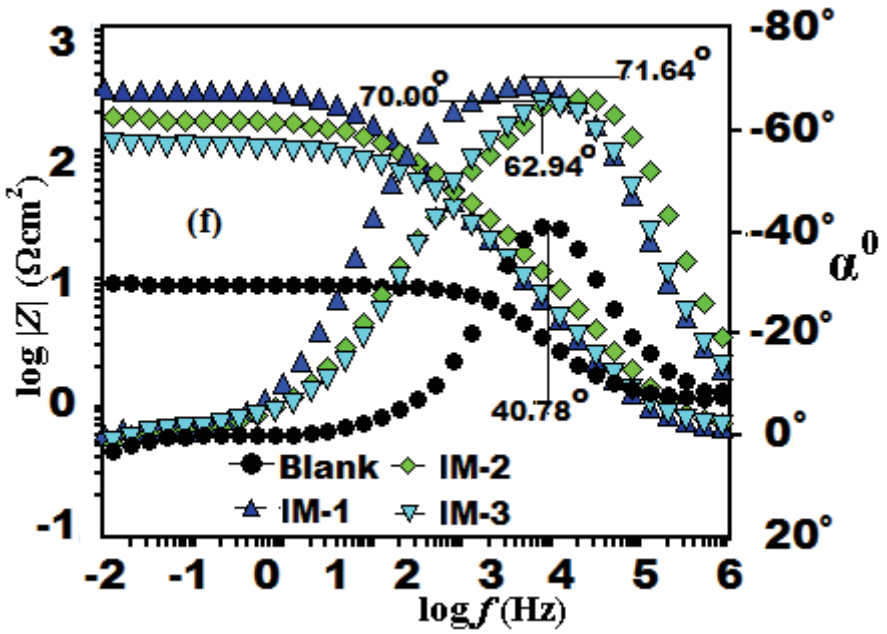

Figure 3.3.5.f: Bode (log f vs. log |Z|) and phase angle (log f vs. α◦) plots of impendence spectrain absence and presence of optimum concentration of IMs at 308 K

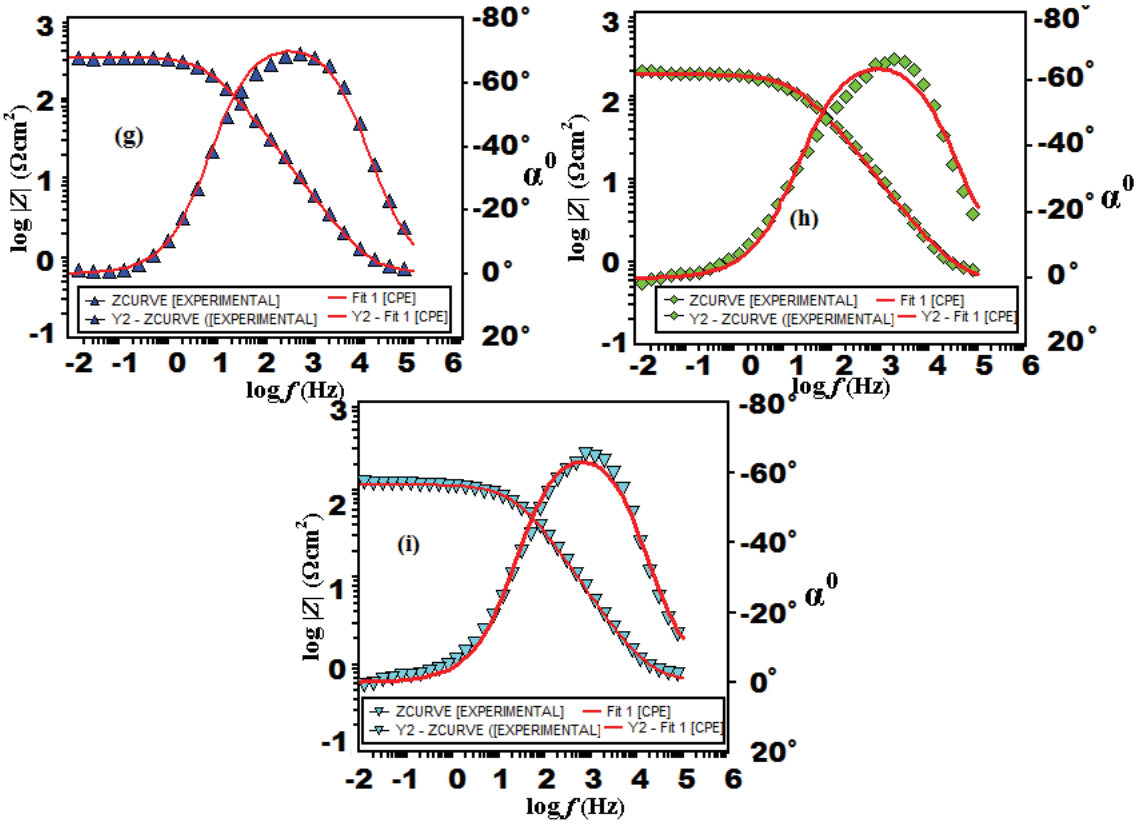

Figure. 3.3.5.(g, h, i): fitted Bode (log f vs. log |Z|) and phase angle (log f vs. α◦) plots of impendence spectra in absence and presence of optimum concentration of IM-1, IM-2, and IM-3 at 308 K

3.3.6. Potentiodynamic polarization study

The potentiodynamic polarization curves of mild steel in 1 M HCl solution at 308K at the optimum concentration (100mgL^{-1}) of imidazoles molecules are shown in Fig. 3.3.6 and the potentiodynamic polarization parameters are given in Table 3.3.6. The polarization results showed that corrosion current density is significantly reduced in presence of IMs without any change in appearance of polarization curves. This reveals that IMs inhibit the corrosion by blocking active sites of the metallic surface without any change in the corrosion mechanism [Yıldız *et al*. (2014)]. The maximum displacement in the E_{corr} values for inhibited specimen with respect to the uninhibited specimen is 67 mV towards cathodic side, which is

less than 85 mV. This clearly suggests that investigated IMs are mixed type inhibitors and predominately act as cathodic inhibitors. Figure 3.3.6 reveals that on addition of IMs decreases both anodic and cathodic reactions which suggest that inhibiting molecules are adsorbed on anodic and cathodic sites. The values of both anodic and cathodic tafel slopes (βa, βc) are slightly change on the addition of IMs which indicated the reduction of anodic dissolution of MS and cathodic hydrogen evolution reactions without affecting in the reaction mechanism [Qian *et al.* (2013)].

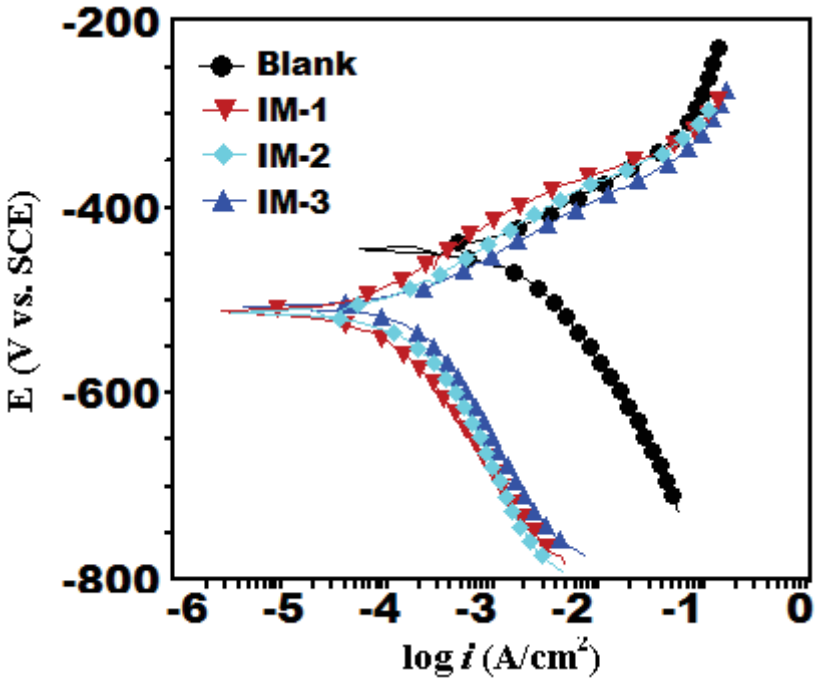

Figure 3.3.6: Polarization curves for corrosion of mild steel in absence and presence of optimum concentrations of IMs

Table 3.3.6: Potentiodynamic polarization parameters (±SD) for mild steel in 1M HCl in absence and presence of optimum concentration (100mgL^{-1}) of inhibitors

Inhibitor	E_{corr} (mV/SCE)	i_{corr} (μA/cm^2)	β_a (mV/dec)	$-\beta_c$ (mV/dec)	η (%)
Blank	-445	1320(0.003)	74.6	123.9	----
IM-1	-512	74.3(0.002)	89.3	133	97.67
IM-2	-513	116.0(0.002)	81.1	143.9	96.37
IM-3	-507	190.0(0.003)	71.3	186.6	94.06

3.3.7 Surface characterization

3.3.7.1. Scanning electron microscopy

The MS surface which has been immersed in the uninhibited test solution is rough and damaged due to metal dissolution (Figure 3.3.7.1.(a), however the surface of the inhibited MS specimen (Figure 3.2.7.1.(b-d) (IM-1, IM-2, IM-3) shows relatively smooth surface, which reveals the formation of protective inhibitor film on the MS surface[Zhang *et al* (2009)].

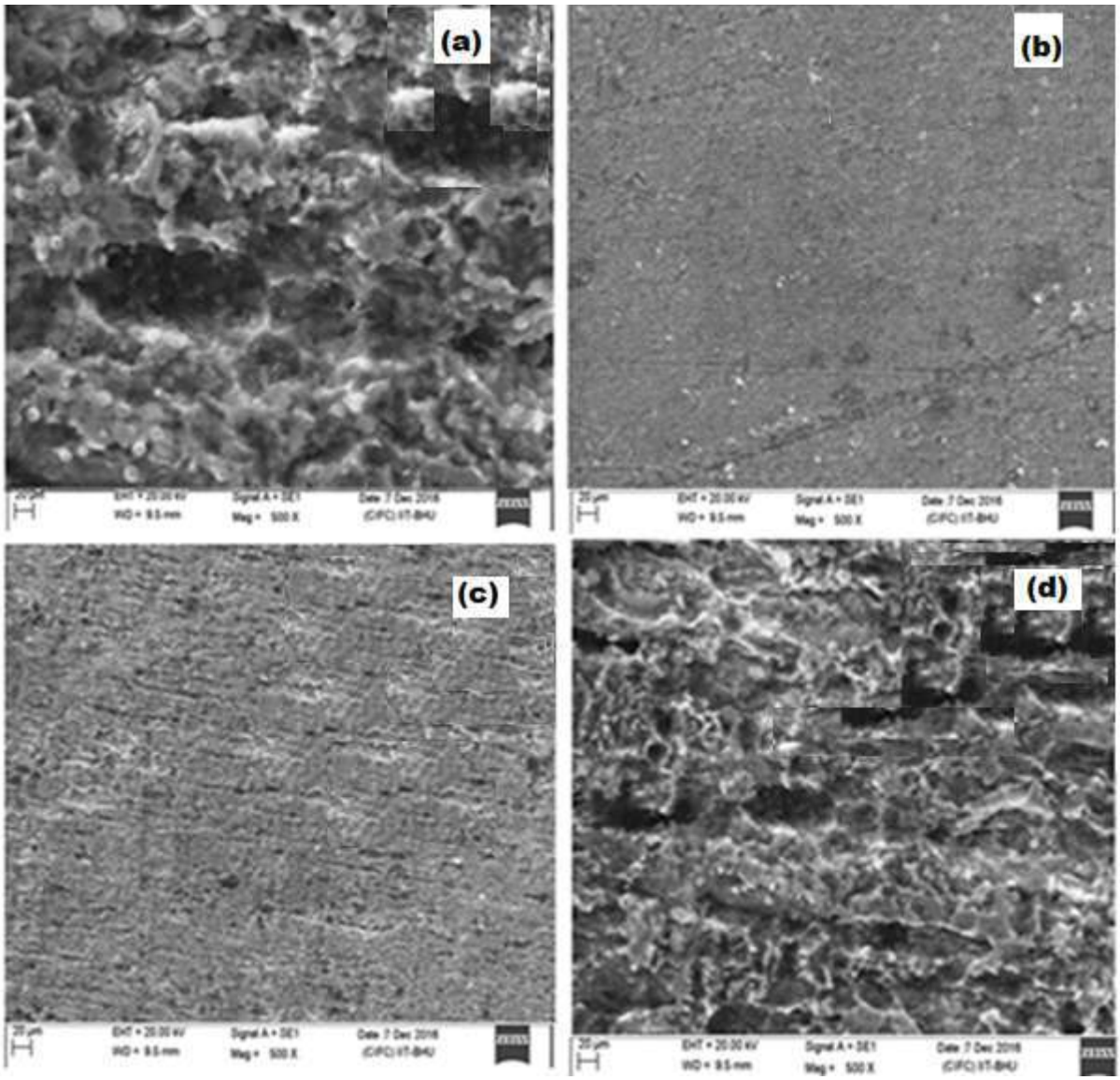

Figure 3.3.7.1: SEM image of mild steel (a) Blank (b) IM-1 (c) IM-2 (d) IM-3

3.3.7.2. Atomic force microscopy

The three-dimensional AFM images of uninhibited and inhibited MS samples are shown in Figure. 3.3.7.2(a-d) (AFM (a) Blank (b) IM-1 (c) IM-2 (d) IM-3). The average roughness of MS sample in 1M HCl solution without inhibitor (Figure. 3.2.7 a) was 400 *um*. However, in the presence of optimum concentration (100mgL^{-1}) of IM-1, IM-2 and IM-3 as shown in Figure. 3.3.7.2 (b-d), the average roughness was reduced to 30 *um*, 100 *um* and 150 *um*

respectively. The lower value of roughness for imidazoles reveals the presence of protective film on metal surface.

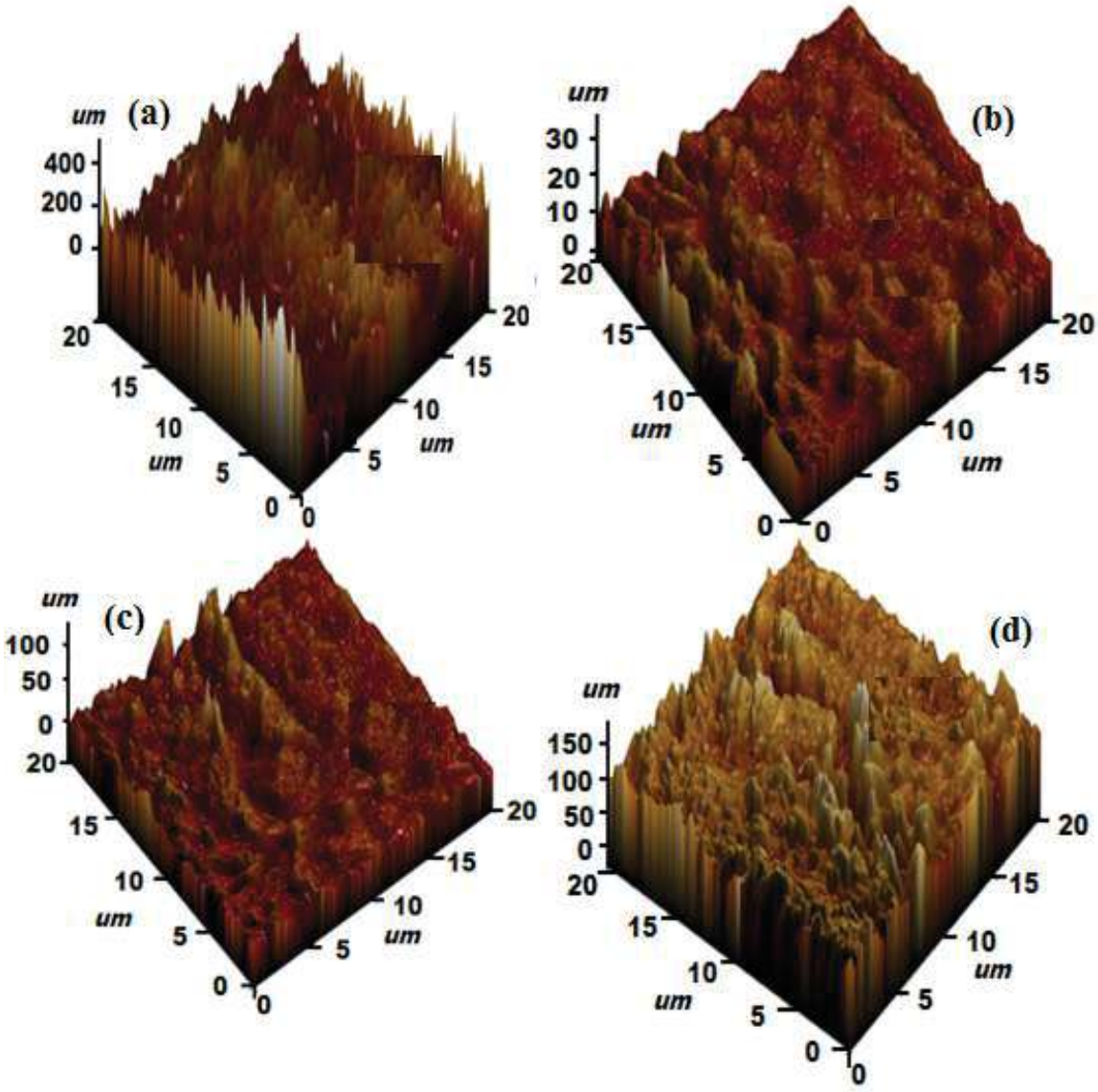

Figure 3.3.7.2: AFM (a) Blank (b) IM-1 (c) IM-2 (d) IM-3

3.3.8. Quantum chemical calculations

The optimized geometry, E_{HOMO} and E_{LUMO} of IMs for neutral and protonated inhibitors are shown in Figure. 3.3.8.1 and Figure 3.3.8.2 In the present study energy of highest occupied molecular orbital (E_{HOMO}), energy of lowest unoccupied molecular orbital (E_{LUMO}) and

energy gap (ΔE) (ΔE_{LUMO}-E_{HOMO}), dipole moment (μ), electronegativity (χ), and the hardness (η), softness (σ), and the fraction of the electron transfer (ΔN) were calculated for neutral and protonated molecules in gas phase are given in Table 3.3.7.

3.3.8.1. Neutral IMs

Figure 3.3.8.1, it could be observed that HOMO regions of IM-1 and IM-2 are delocalized over the imidazole ring, but in the case of IM-3 HOMO is distributed over the NO_2 group and the imidazole ring. LUMO regions of IM-1 and IM-2 are localized over the imidazole ring and the methoxy substituted phenyl ring. In IM-3 these regions are spread over the NO_2 substituted phenyl ring. Table 3.3.7 shows that the order of energy gap (ΔE) among the three IMs is as follows: IM-1< IM-2< IM-3 respectively [Zhang *et al.* (2016)], [Chiter *et al.* (2015)]. A chemical species with high value of softness (σ) and lower value of hardness (η) is associated with the strong interaction with metal and the high IE. In the present study the values of softness follows the order IM-1> IM-2> IM-3 and the order of hardness is as IM-1< IM-2< IM-3 respectively, which is in accordance to the order of IE obtained experimentally. The relative performance of inhibiting molecules can also be predicted on the basis of their ΔN values (fraction of electron transfer). It is reported that higher value ΔN associated with the high IE [Tehrani and Niazi (2015)], [Verma *et al.* (2015**(a)**]. In the present study the value of (ΔN) for imidazole is not followed the regular trends. Generally dipole moment (μ) is a measure of polarisibility of any organic molecule. Chemical species with high value of μ is more polarisable and covers larger surface of the metal surface, thereby act as a good corrosion inhibitor as compared to molecule with lower value of μ [Petkova and Peyerimhoff (2002)], [Geerlings *et al.* (2009)]. In the present case the order of dipole moment is IM-1> IM-2> IM-3, thereby suggesting that IM-1 is the best inhibitor among the three imidazoles.

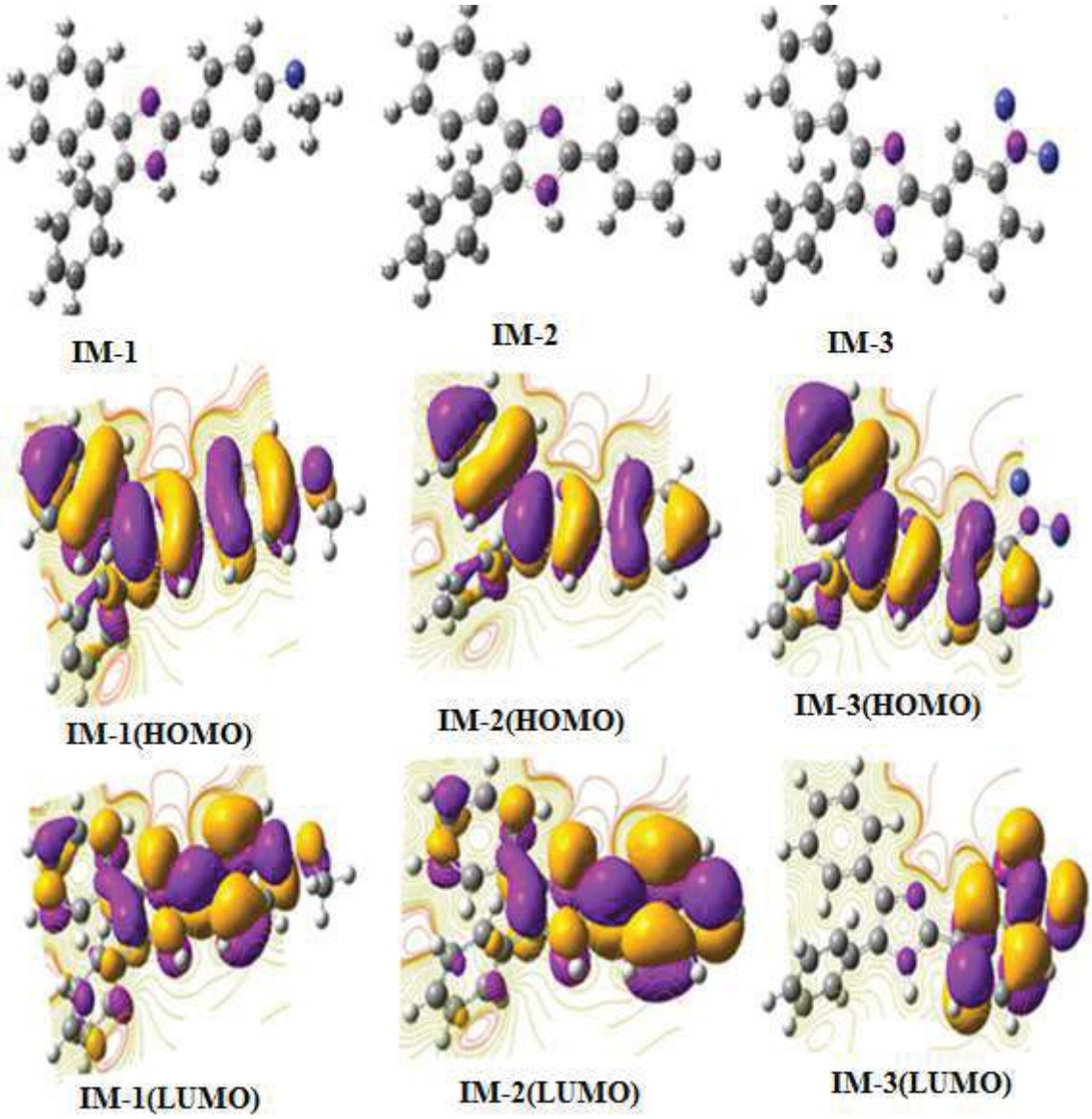

Figure 3.3.8.1: The gas phase optimized molecular structures, the HOMO, and the LUMO electron density distribution surfaces of IM-1, IM-2, and IM-3 for neutral inhibitors.

3.3.8.2 Protonated IMs

Figure 3.3.8.2 represents the optimized, HOMO and LUMO of the protonated imidazole inhibitors. HOMO regions of protonated IM-1 and IM-2 are distributed over the of the 3,4 substituted phenyl rings of imidazole while in the case of IM-3 HOMO regions are distributed over 4 substituted phenyl ring of the imidazole. The LUMO regions of IM-1 and

IM-2 are distributed over the methoxy substituted phenyl ring of imidazole ring. And in the case of IM-3, the LUMO regions are distributed over the imidazole ring and the NO_2 substituted phenyl ring. From Table 3.3.7, ΔE values are lower in case of protonated inhibitors than the neutral imidazoles which suggest that protonated molecules readily adsorb on the MS surface than the neutral inhibitors. The predominant cathodic behaviour of imidazole molecules supports the high IE of the protonated molecules

The values of hardness for the protonated molecules are given Table 3.3.7 which follows the order IM-1<IM-2 <IM-3 respectively. And the softness of the protonated imidazole molecules follows the order; IM-1> IM-2> IM-3. Table 3.3.7 reveals that all the calculated ΔN values are negative, which means that the electron donation from inhibitor molecules to the metal surface is not possible [Dohare *et al* (2017**(a)**]. The values of ΔE for protonated IMs are less as compared to the neutral molecules, which suggests that protonated IMs are more reactive than the neutral molecules. And readily accept electrons from the metal surface and thereby form a strong bond between metal and inhibitor.

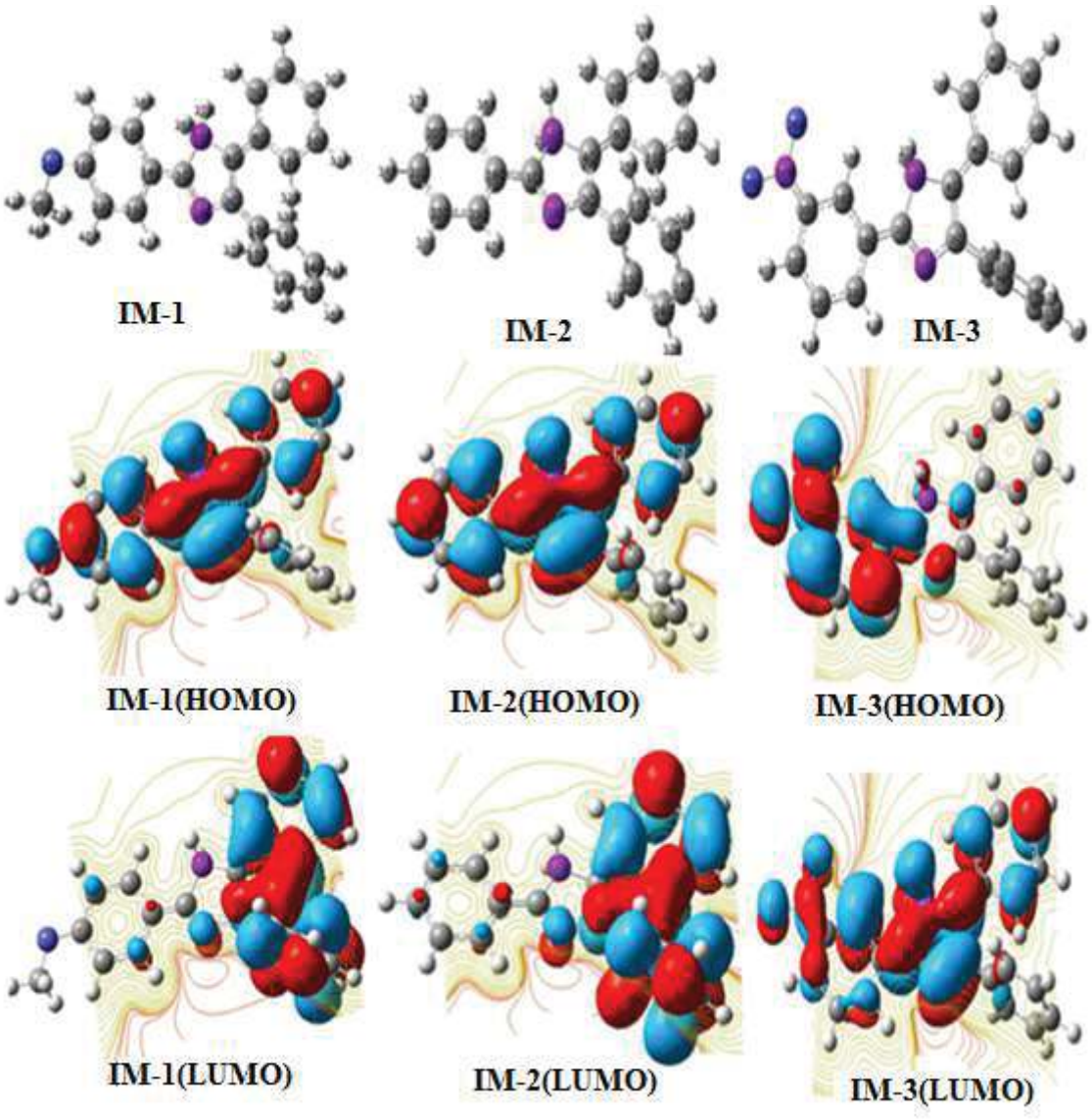

Figure 3.3.8.2: Optimized structure and the frontier molecular orbital density distributions for protonated IMs (d-e) IM-1 (f-g) IM-2 (h-i) IM-3 respectively

Table 3.3.7: Calculated quantum chemical parameters of neutral and protonated IMs in gas phase.

Inhibitors	μ (Debye)	E_{HOMO} (eV)	E_{LUMO} (eV)	ΔE (eV)	η (eV)	$^{b}\sigma$ (eV^{-1})	ΔN (eV)
Neutral form							
IM-1	7.16	-4.83	-3.45	1.38	0.69	1.44	0.48
IM-2	4.59	-4.59	-1.65	2.93	1.46	0.68	0.57
IM-3	3.02	-4.51	-1.47	3.03	1.53	0.65	0.60
Protonated form							
IM-1	6.78	-7.98	-6.86	1.12	0.56	1.77	-2.31
IM-2	4.39	-7.75	-5.43	2.32	1.16	0.86	-0.76
IM-3	2.53	-7.67	-5.22	2.44	1.22	0.81	-0.72

3.3.9. MD simulations

Figure 3.3.9 (a, b) (Temperature (a) and Energy (b) equilibrium curves of studied inhibitors adsorbed on the Fe (1 1 0) surface in solution) shows that both the temperature and energy were balanced. The interaction and the binding energies of the inhibitor molecules have been calculated. Figure 3.3.9(c) represents the top and the side view adsorption of IMs inhibitors on the Fe surface. To maximize the contact surface area, the inhibitors molecules moved gradually in the parallel mode to the Fe surface which could enhance the degree of surface coverage by forming a protective film. There are significant interactions between studied compounds and iron atoms mostly due to the presence of π-bonds in phenyl rings as well as nitrogen atoms in imidazole ring. Table 3.3.8, shows that the interaction and the binding energies are higher for IM-1 than the IM-2 and IM-3, which suggest that IM-1 is strongly bonded to iron atoms compared to (IM-2 and IM-3). It is reported in the literature, that more

negative interaction energy value suggests highest adsorption ability of an inhibitor on the Fe surface [Kaya *et al.* (2016)], [Saha *et al.* (2014**(a)**]. Furthermore, the higher magnitude of binding energies means the easier adsorption of inhibitor molecules onto the metal surface and the higher stability of adsorptive system [Saha *et al.* (2014**(b)**]. The lowest IE of IM-3 is attributed to the presence of electron withdrawing ($–NO_2$) [Yan *et al* (2013)] while highest IE of IM-1 due to presence of the electron donating group ($–OCH_3$) [Fouda *et al* (2008)].

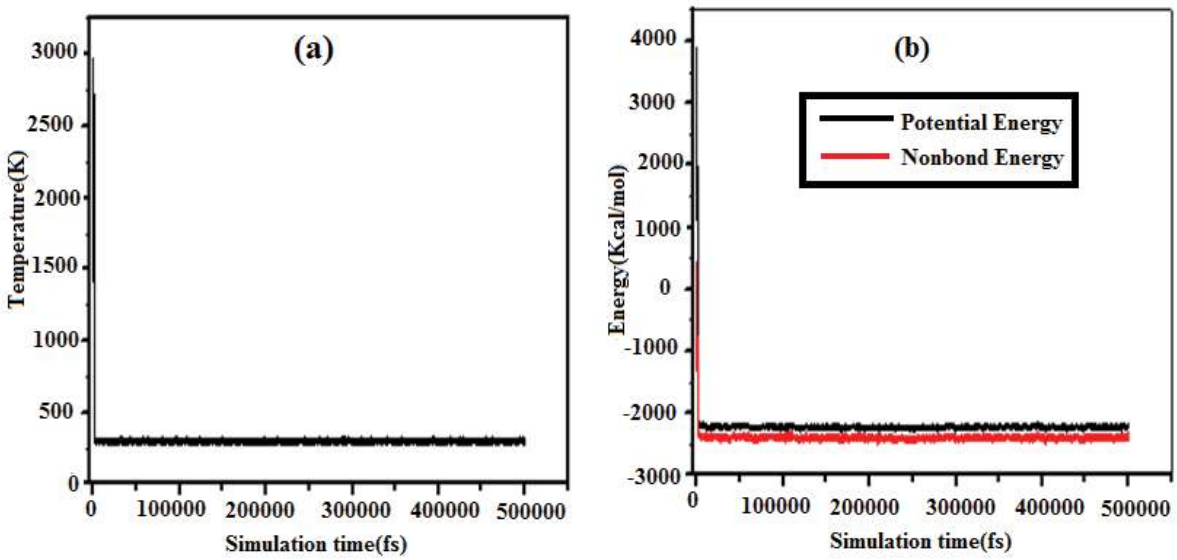

Figure 3.3.9 (a, b): Temperature (a) and Energy (b) equilibrium curves of studied inhibitors adsorbed on the Fe (1 1 0) surface in solution.

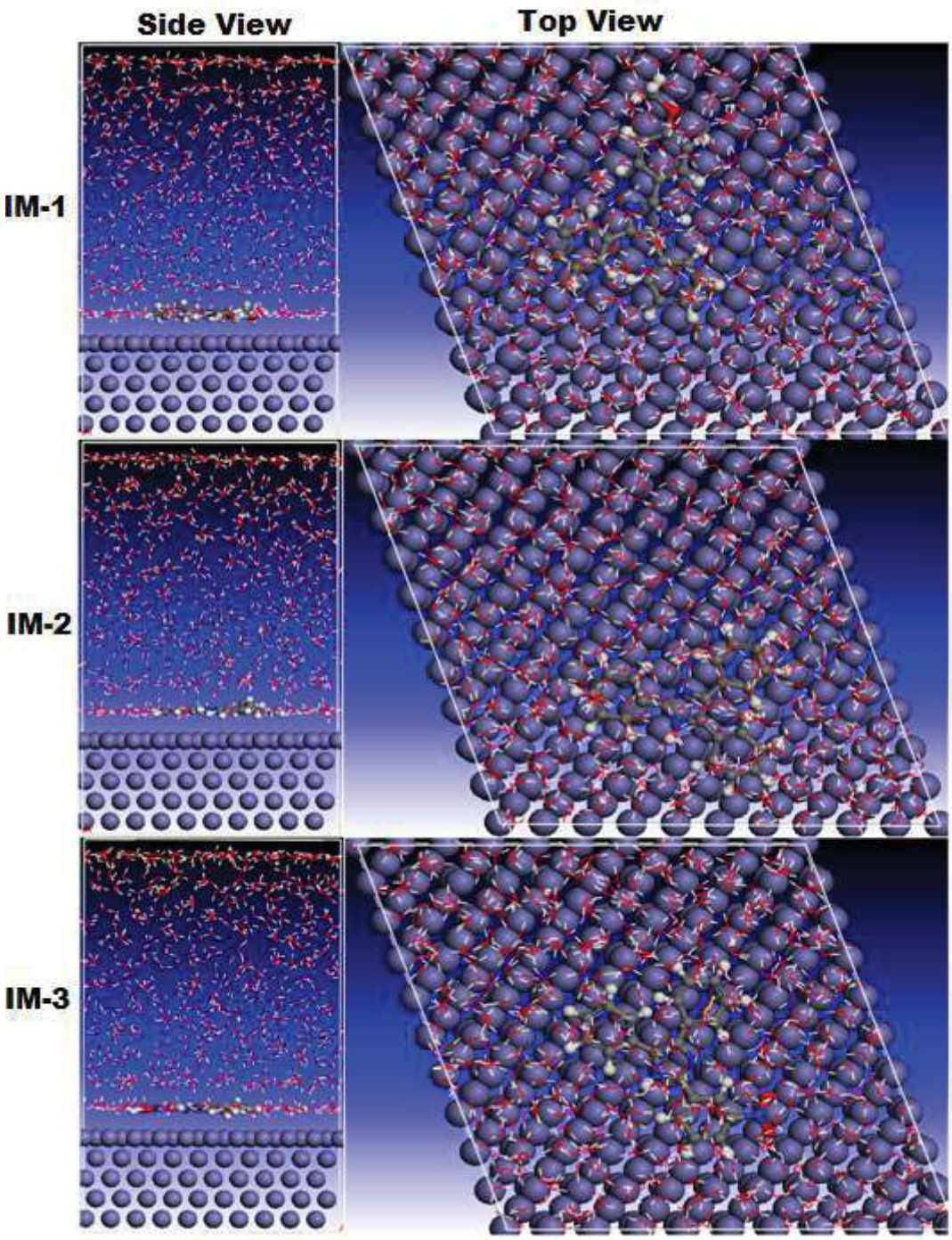

Figure 3.3.9 (c): Side and top views of the final adsorption of the neutral inhibitors on the Fe (110) surface in solution.

Table 3.3.8: Selected energy parameters obtained from MD simulations for adsorption of inhibitors on Fe (110) surface.

System	Neutral form	
	$E_{\text{Interaction}}$ (kJ/mol)	E_{Binding} (kJ/mol)
Fe + **IM-1**+500H_2O + $5H_3O^+$ + $5Cl^-$	-1060,343	1060,343
Fe + **IM-2**+500H_2O + $5H_3O^+$ + $5Cl^-$	-987,014	987,014
Fe + **IM-3**+500H_2O + $5H_3O^+$ + $5Cl^-$	-956,111	956,111

In the present study, we have also examined the different interactions between the inhibitor and iron atoms using radial distribution functions (RDFs). [Zhang, *et al* (2016)]. The RDF is widely used as useful method to investigate the bond length between the metal and inhibitor. The RDFs were calculated from the MD simulations trajectories [Wu *et al* (2017)]. The RDF, *g(r)*, is defined as the probability of finding particle B within the range $r + dr$ around particle A. Is defined as follows [Wu *et al* (2017)]:

$$g_{AB}(r) = \frac{1}{\langle \rho_B \rangle_{\text{local}}} \times \frac{1}{N_A} \sum_{i \in A}^{N_A} \sum_{j \in B}^{N_B} \frac{\delta(r_{ij} - r)}{4\pi r^2} \qquad (3.1)$$

Where $\rho_{B\,\text{local}}$ represents the particle density of *B* averaged over all shells around particle *A*. The peak distance in RDFs indicates how much meaningful are interactions with iron surface [Benzon *et al*. (2017)]. The peak within 3.5 Å, it's an indication of small bond length which indicates the chemisorptions, while the peak greater than 3.5 Å shows the physical interactions [Xie *et al.* (2015)]. Figure 3.3.9 (d) (RDF of neutral forms of IM-1 on the Fe (110) surface in solution) shows the RDF curves for neutral IM-1 molecule. The bond length

of IM-1 atoms (Fe-N, Fe-O and Fe-C) are around 3.22, 3.25 and 3.25 Å respectively, which is less than the $3.5A^{O}$ suggesting a strong chemical interaction between metal and IM-1. The results are consistence with experimental findings.

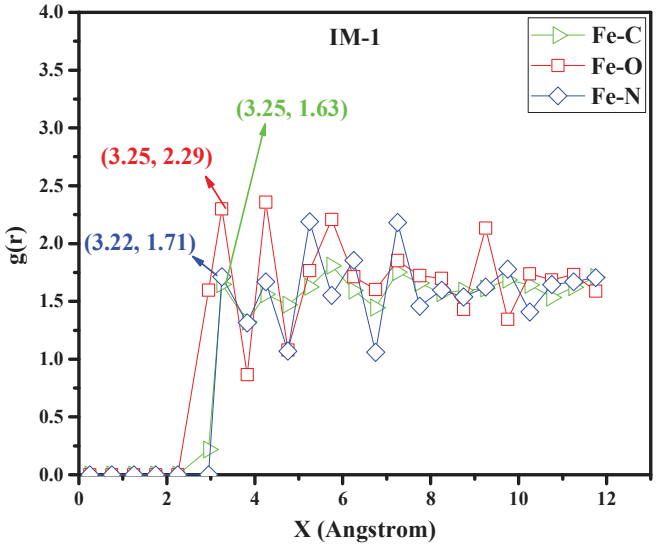

Figure 3.3.9(d): RDF of neutral forms of IM-1 on the Fe (110) surface in solution.

3.3.10. Mechanism of inhibition:

On the basis of experimental and theoretical results following adsorption and inhibition mechanism can be proposed (Fig. 3.3.10Physio-chemical mechanism of IM-1 on the MS surface):

The protonated inhibitor molecules in chloride containing solutions gets adsorb on chloride ion through electrostatic interaction (physical adsorption).

$$[IM] + x\,H^{+} \rightleftharpoons [IM_{x}]^{x+}$$

(2) At cathodic site this protonated molecules accept electrons and become neutral. These neutral inhibitor molecules are chemically adsorbed on metal surface through their lone pair of electron present on heteroatoms.

(3) Inhibitors molecules can also accepts electrons in their antibonding orbital from d orbital of the Fe through reterodonation and thereby strengthen the adsorption on the metal surface.

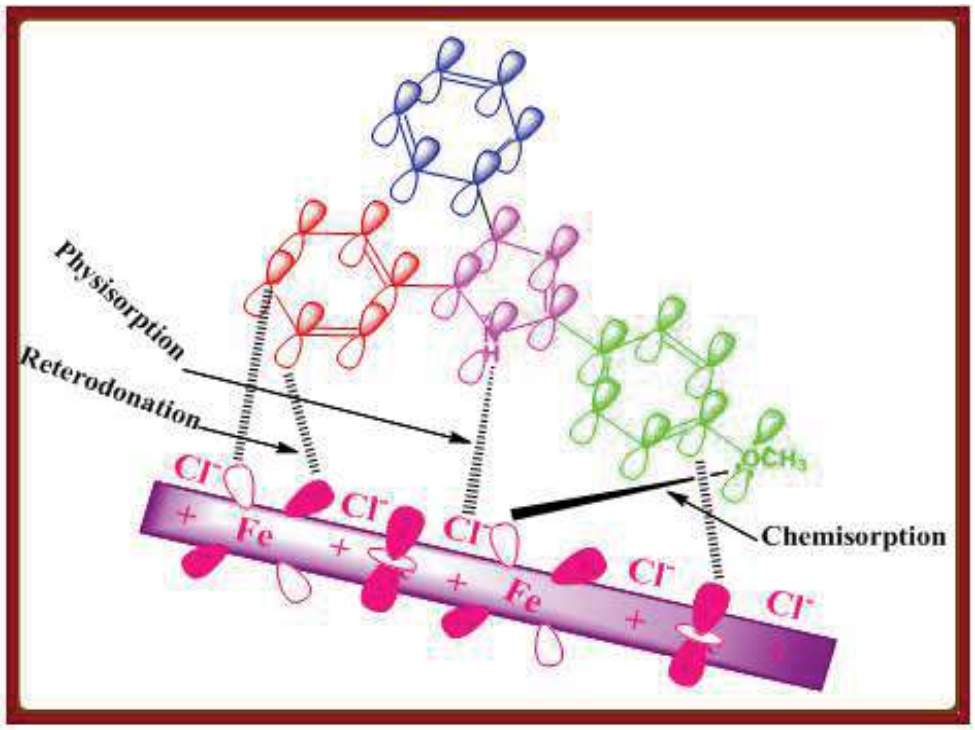

Figure 3.3.10: Physio-chemical mechanism of IM-1 on the MS surface.

3.4. Pyrazolopyridine as corrosion inhibitors

The condensed Pyrazolopyridine are heterocyclic compounds containing pyrazole ring fused with pyridine ring. This section reviews the inhibitive effect of Pyrazolopyridine as corrosion inhibitors. Until now, very few Pyrazolopyridine have been investigated [Mhammedi *et al.* (2007)], [Singh and Quraishi *et al* (2016)].

The present section describes the efficiency of three condensed pyrazole-pyridines namely, (4-(4-methoyphenyl)3,5-dimethyl-1,4,7,8-tetrahydro-dipyrazolopyridine) (PP-1), 3,5dimethyl-4-phenyl-1,4,7,8-tetrahydrodipyrazolopyridine (PP-2) and (3,5-dimethyl-4-(3-nitrophenyl)-1,4,7,8-tetrahyddrodipyrazolopyridine) (PP-3) and studied their corrosion inhibition performance on mild steel in 1M HCl. These compounds have been selected as corrosion inhibitors because they are non-toxic and exhibited various biological activities such as anti-allergic, anxiolytic and anti-herpetic properties etc [Chevalier *et al* (2014)], [Liu *et al* (2009)], [Dilger *et al* (2002)]. The corrosion inhibition tests were performed on mild steel in 1M hydrochloric acid medium using weight loss method, potentiodynamic polarization measurements and electrochemical impedance spectroscopy. The surface morphology of the inhibited MS specimens were examined by scanning electron microscope (SEM), atomic force microscopy (AFM). The experimental findings were supported by the quantum chemical and Molecular dynamics investigations of mild steel specimens. The survey of literature reveals that these pyrazolo-pyridine derivatives (PPs) have not been investigated as corrosion inhibitors. The molecular structure and IUPAC name of the inhibitors used are given in Table 3.4.1.

Table 3.4.1: IUPAC Name, molecular structure and abbreviation of the condensed Pyrazolopyridine used

S. NO	Inhibitor	Structure	Analytical data
1	(4-(4-methoyphenyl) 3,5-dimethyl-1,4,7,8-tetrahydrodipyrazolo pyridine) (PP-1)	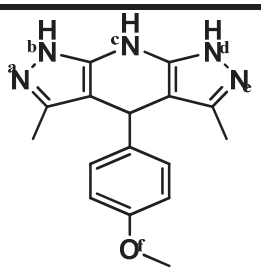	White crystalline powder; m.p= 321-323^{o}C; ^{1}H NMR (500 MHz, DMSO) δ (ppm): 1.48, 3.77, 4.38, 4.63, 6.87-7.32, 10.93, 11.96
2	3,5dimethyl-4-phenyl-1,4,7,8-tetra hydro dipyrazolopyridine (PP-2)	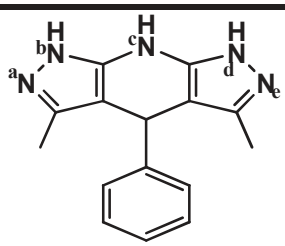	White crystalline powder; m.p= 271-273oC; 1H NMR (500 MHz, DMSO) δ (ppm): 1.49, 4.65, 4.41, 7.12-7.56, 6.87-7.32, 10.96, 11.99
3	(3,5-dimethyl-4-(3-nitrophenyl)-1,4,7,8-tetrahyddrodipyrazolo pyridine) (PP-3)	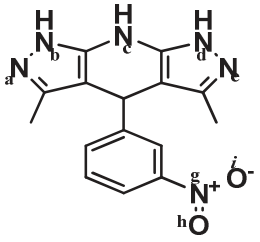	Pale yellow crystalline powder ; m.p= 271-273oC; 1H NMR (500 MHz, DMSO) δ (pp): 1.93, 4.0, 5.34, 7.53-8.16, 7.59 12.62

3.4.1. Gravimetric measurement

Table 3.4.2 shows the values of inhibition efficiencies and corrosion rates obtained from gravimetric measurements in absence and presence of different concentrations of PPs in 1 M HCl after 3h immersion at 308 K. The variation of inhibition efficiency (η %) with inhibitor concentration is shown in Figure 3.4.1(a). From Figure. 3.4.1 (a) it is revealed that on increasing the inhibitor concentration, the inhibition efficiency increased. The maximum

inhibition efficiency (IE) was obtained for PP-1 97.5% among the three studied inhibitors at optimum concentration 100 mgL^{-1}.The inhibition efficiency of PPs follows the order: PP-1> PP-2> PP-3 respectively at 100 mgL^{-1}. The maximum inhibition efficiency for PP-1 was 97.5%. The better performance of PP-1 was due to the presence of electron donating methoxy group, and lower I.E of PP-3 is attributed to the presence of electron withdrawing NO_2 group.

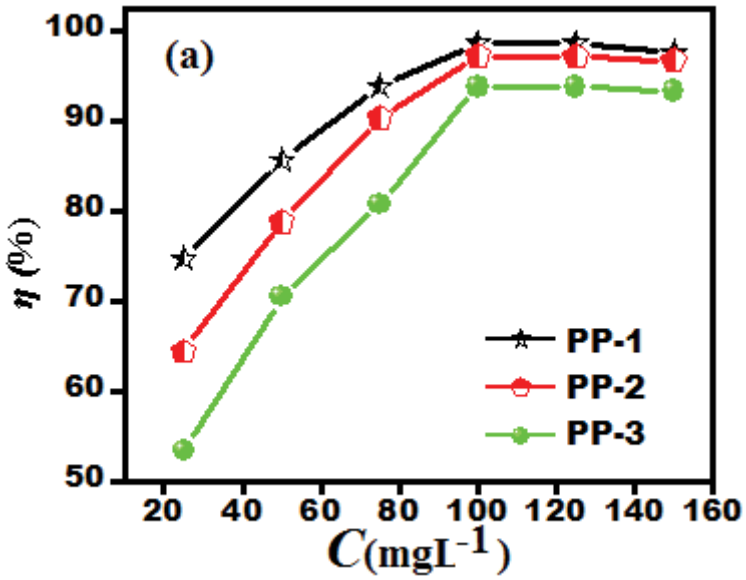

Figure 3.4.1 (a): Variation of inhibition efficiency (η%) with inhibitor concentration at 308 K

Table 3.4.2: Corrosion parameters for the mild steel in 1 M HCl containing various concentrations of the PPs at 308 K obtained from gravimetric measurements

Inhibitor	Concentration (mgL^{-1})	Wt Loss	C_R (mm/year)	(η) %
Blank	--	210	7.0000	--
PP-1	25	37	1.23	74.6
	50	21	0.71	85.6
	75	9	0.43	93.8
	100	2	0.06	98.5
	125	2	0.1	98.3
	150	5	0.16	97.6
PP-2	25	52	1.73	64.38
	50	31	1.03	78.76
	75	14	0.46	90.41
	100	4	0.13	97.26
	125	6	0.20	97.14
	150	7	0.23	96.66
PP-3	25	68	2.26	53.42
	50	43	1.43	70.54
	75	28	0.93	80.82
	100	9	0.30	93.83
	125	13	0.43	93.80
	150	14	0.46	93.33

(iii) The effect of temperature on the performance of the PPs at their optimum concentrations on mild steel in 1M HCl was studied using gravimetric tests at 308, 318, 328 and 338 K. The inhibition efficiency of PPs decreased with increasing temperature both in free acid and inhibited acid solutions as shown in Figure. 3.4.1(b).

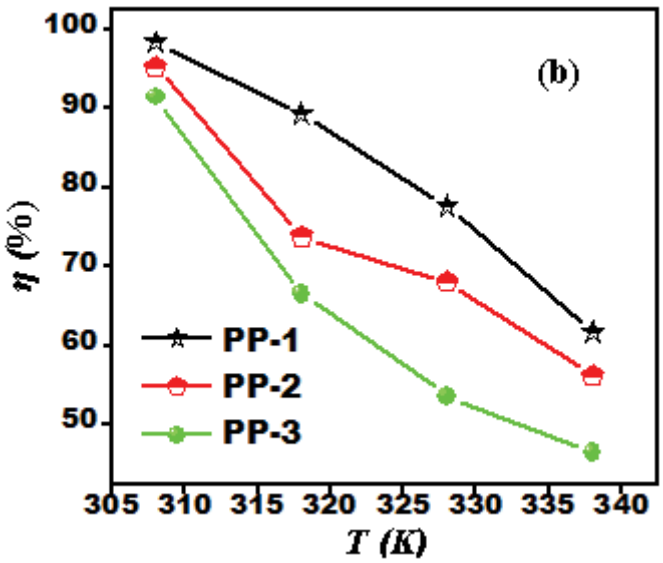

Figure 3.4.1(b): Variation of inhibition efficiency (η%) with solution temperature (308-338 K) at optimum concentration of PPs

3.4.2. Thermodynamic Parameters and Adsorption Considerations

The apparent activation energy (*E*a) value was determined from the plot of log C_R versus 1000/T as shown in Fig. 3.4.1(c). Inspection of Table 3.4.3 shows that the values of E_a are higher in inhibited solution than the inhibitor free solution. The higher values of *E*a indicate that high energy barrier for the corrosion reaction in presence of the inhibitor is attained [Chaubey *et al*. (2009)], [Noor *et al* 2008]. This indicates that as the temperature increased there is an appreciable decrease in the adsorption of inhibitors, which in turn increases the corrosion rate because more metal steel surface area is now exposed to the acidic environment.

Table 3.4.3: Thermodynamic parameters for the adsorption of inhibitor on mild steel in 1M HCl at optimum concentration of PPs

Inhibitor	K_{ads} (10^4 M^{-1})	$-\Delta G^{\circ}_{ads}$(kJ mol^{-1})	E_a(kJ mol^{-1})
Blank	----	----	28.74
PP-1	2.5	36.26	120.04
PP-2	1.8	35.38	95.54
PP-3	1.2	34.51	83.06

Attempts were made to fit the θ values to various isotherms, including Langmuir, Temkin and Frumkin. By far, the best fit is obtained with the Langmuir isotherm. Fig. 3.4.1 (d) shows the plots of log (θ/1-θ) versus log C and the expected linear relationship is obtained for all the four PPs. The values of equilibrium constant of adsorption (K_{ads}) and standard free energy of adsorption ($\Delta G°_{ads}$) are listed in Table 3.4.3. The calculated values of $\Delta G°_{ads}$ for studied inhibitors range from -36.26 to -34.51 $kJmol^{-1}$ which indicate their mixed mode of adsorption on to the MS surface[Li *et al* (2011)], [Shuduan *et al* (2014)]. The higher values of K_{ads} suggesting that higher inhibition effect [Yuce *et al.* (2012)].

Table 3.4.4: Adsorption parameters for PPs calculated from different adsorption isotherm for mild steel in 1M HCl solution at 308K

Adsorption isotherm	Inhibitor	Correlation coefficient	Slope
Langmuir	PP-1	0.996	0.997
	PP-2	0.998	0.987
	PP-3	0.999	0.945
Temkin	PP-1	0.884	0.048
	PP-2	0.897	0.037
	PP-3	0.897	0.014
Frumkin	PP-1	0.885	4.367
	PP-2	0.886	4.369
	PP-3	0.875	0.602

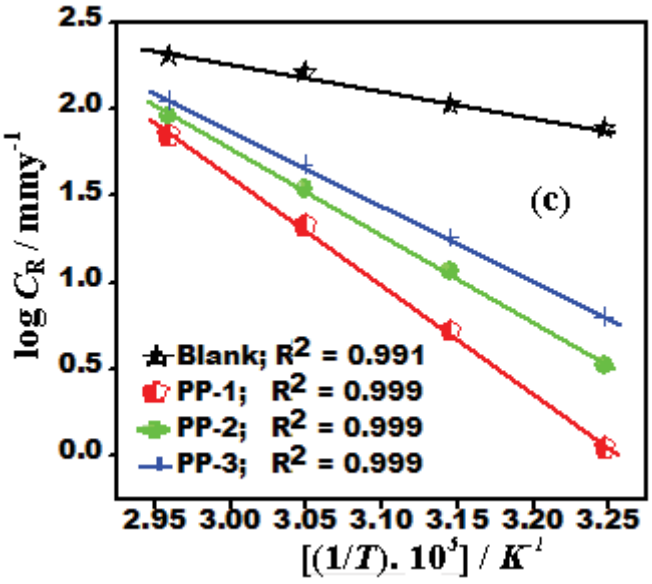

Figure 3.4.1(c): Arrhenius plots of the corrosion rate (C_R) of mild steel in absence and presence of optimum concentration of PPs

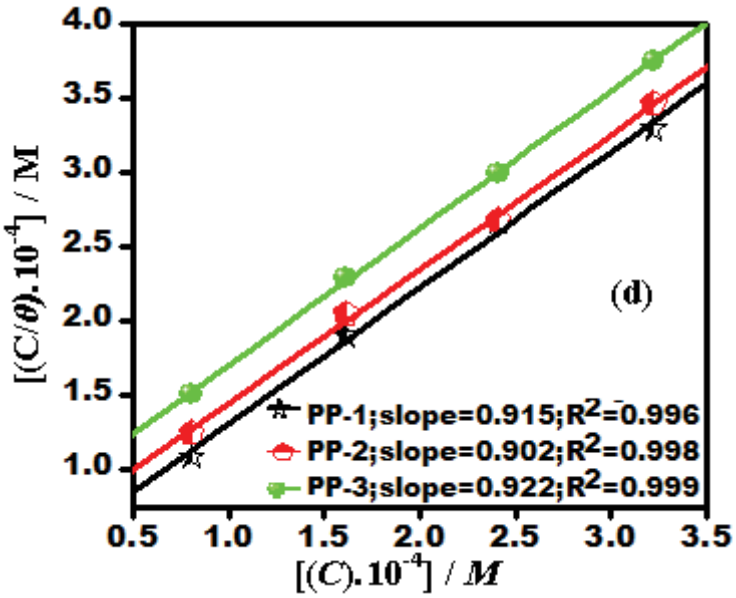

Figure 3.4.1(d): Langmuir adsorption isotherm plots

3.4.3. Electrochemical Impedance Spectroscopy

The electrochemical impedance measurements in the absence and presence of PPs at their optimum concentration (100 mgL^{-1}) are shown in Figure. 3.4.2(a), it is observed from Figure. 3.4.3(a), that the diameter of semicircle significantly increases on the addition of the PPs [Oguzie *et al*(2010)]. The Nyquist plots show single capacitive semi-circles loop which indicates that corrosion inhibition is governed by the charge-transfer process. Also these semi circles loops are depressed with their canters under the real axis, which is due to the surface roughness and frequency dispersion [Krishnaveni *et al* (2014)], [Khamis *et al* (2014)]. All the impedance parameters were calculated from the equivalent circuit model shown in Fig-3.4.2(b), which consists of (R_s) is the solution resistance, (R_p) is the polarization resistance and *CPE* is the constant phase element. The fitness accuracy of the used equivalent circuit is shown by the fitted Nyquist plots of PPs [Figure. 3.4.2(c-e)]. The impedance parameters calculated are listed in Table 3.4.5. The *R*p values are high in inhibited solution (86-221 Ωcm^2) than the uninhibited solution (7.44Ω cm^2) indicated the formation of insulated

adsorption layer of inhibitors on mild steel surface in inhibited solutions. For a circuit including a *CPE*, the double layer capacitance (C_{dl}) can be calculated from *CPE* parameter values Y_0 and n. The decrease in *C*dl in inhibited solution than uninhibited solution is due to the gradual replacement of water molecules by inhibitor molecules at the metal/solution interface, leading to the formation of a protective inhibitor film on the steel surface [Yadav *et al.* (2013)]. The value of n increases in inhibited systems indicating reduction of surface inhomogeneity due to the adsorption of inhibitor molecules on the mild steel surface [Liao *et al*. (2011)].

Fig. 3.4.2 (f) shows the Bode impedance magnitude and phase angle plots recorded for mild steel electrode immersed in 1M HCl in the absence and presence of optimum concentration of PPs at its OCP. An ideal capacitive behavior would result in if a slope value attains -1 and a phase angle value attains -90° [Odewunmi *et al*. (2015)]. The slope values of Bode impedance magnitude plots in intermediate frequency zone, *S*, and the maximum phase angle, $\alpha°$, exhibited deviation from the values of -1 and 90°, respectively. The more negative value of phase angle and the high value of absolute impedance in the presence of PPs indicate the superior performance of PPs. The fitness accuracy of the used equivalent circuit is shown by the fitted bode plots of PPs [Figure. 3.4.2(g-i)]

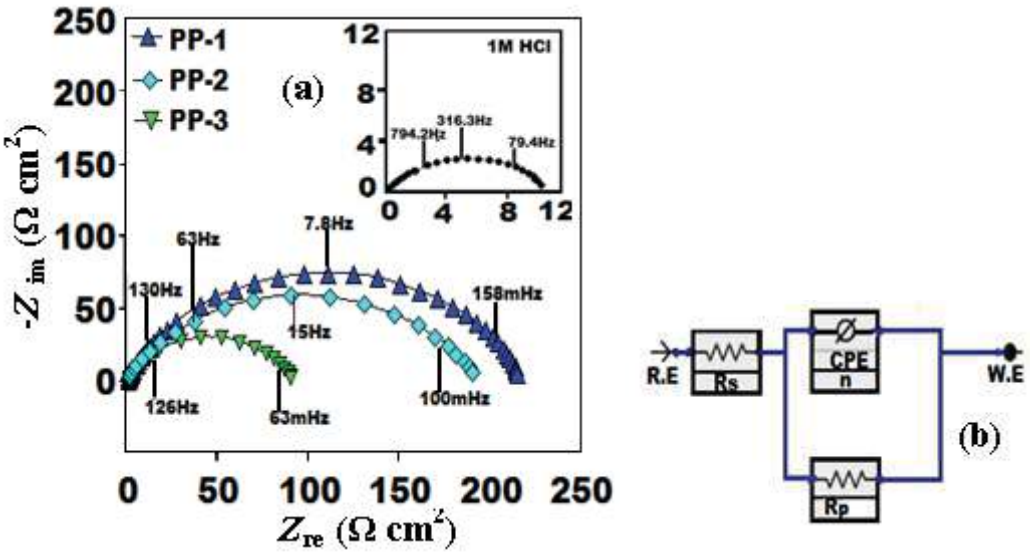

Figure 3.4.3: (a): Nyquist plots for the mild steel at optimum concentration of PPs

Figure 3.4.3: (b): Equivalent circuit model used to fit the EIS data.

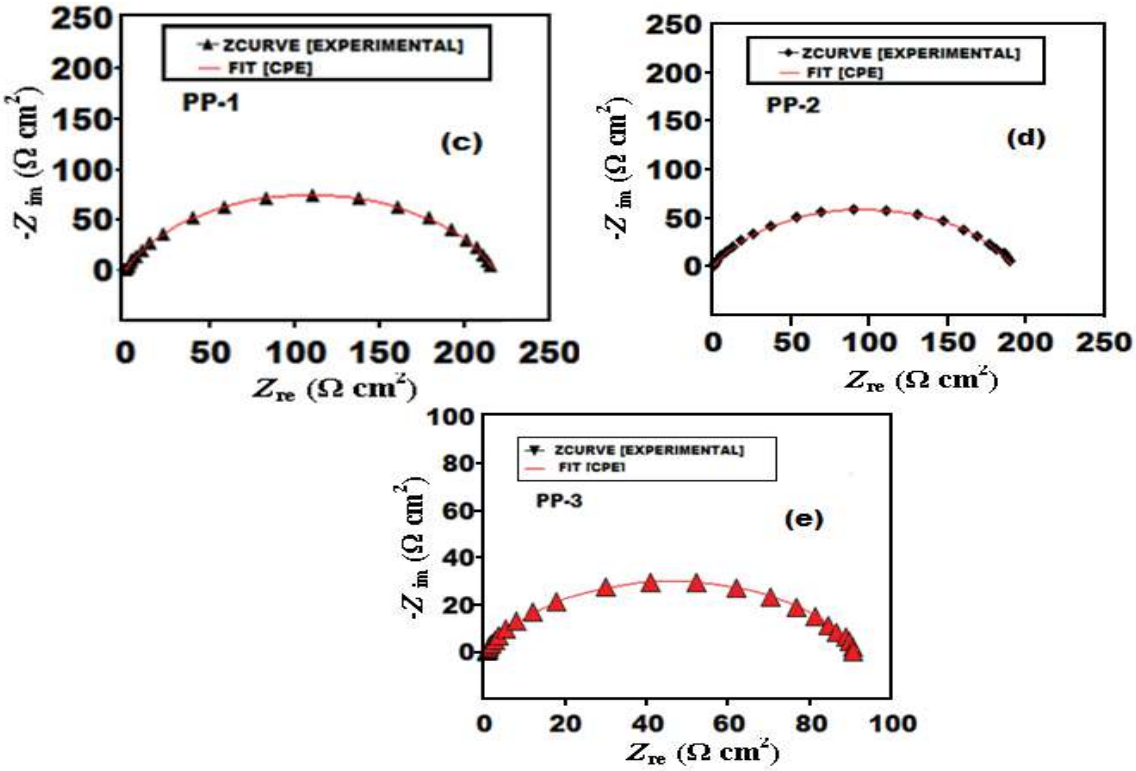

Figure 3.4.3: (c -e) Fitted Nyquist (c) PP-1 (d) PP-2 (e) PP-3 (f-h):

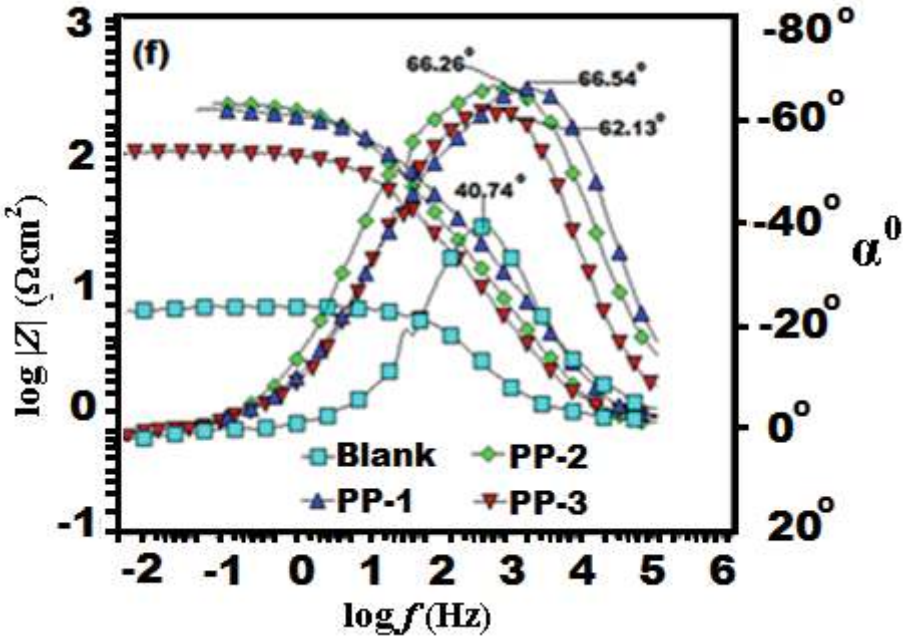

Figure 3.4.3: (f): Bode (log f vs. log |Z|) and phase angle (log f vs. α◦) plots in absence and presence of optimum concentration of PPs at 308 K

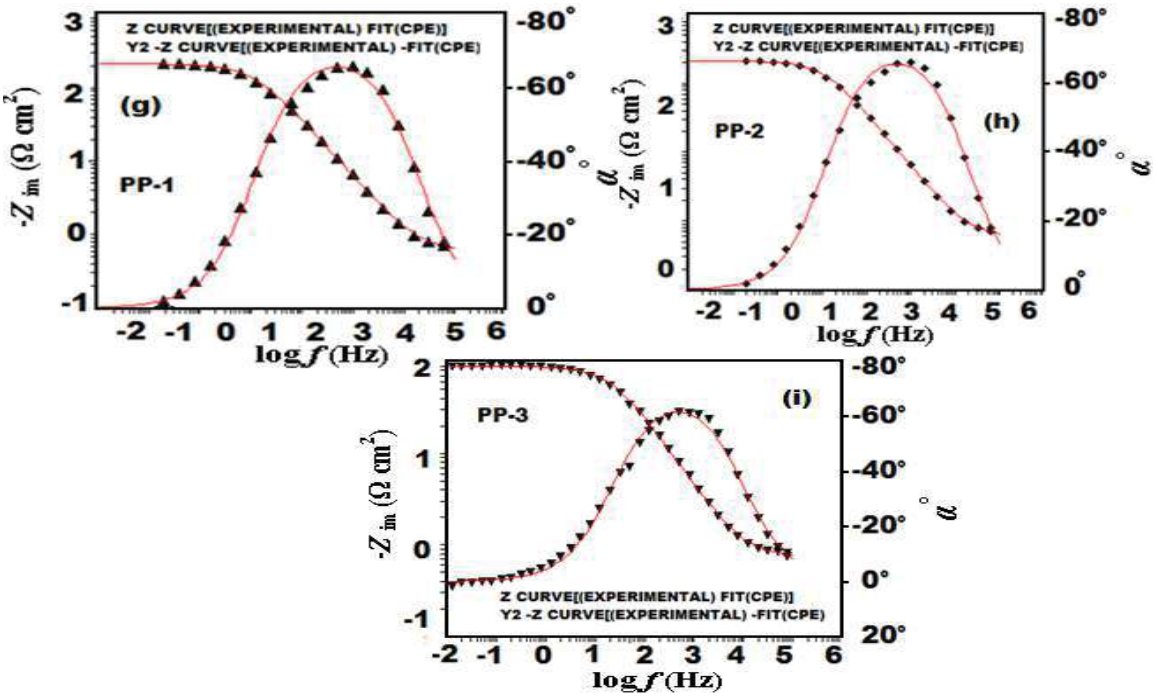

Figure 3.4.3: (g-i): Fitted Bode plot (f) PP-1 (g) PP-2 (h) PP-3(i)

Table 3.4.5: Electrochemical impedance parameters (±SD) for mild steel in 1M HCl in absence and presence of optimum concentration (100 mg L^{-1}) of PPs at 308K

C_{inh} (mgL^{-1})	R_s (Ω)	R_p (Ω cm^2)	n	Y_0 (μF/cm^2)	C_{dl} (μF/cm^2)	η (%)
Blank	1.02 (0.02)	7.44 (0.02)	0.798	481.2	137.9	----
PP-1	0.615 (0.02)	221.4(0.02)	0.853	85.9	48.0	96.5
PP-2	0.653(0.02)	165.2(0.02)	0.818	170.2	76.8	95.2
PP-3	0.758(0.02)	86.4 (0.02)	0.807	250.5	103.2	91.3

3.4.4. Potentiodynamic Polarization study

Fig. 3.4.3 shows the cathodic and anodic polarization curves for mild steel immersed in 1M HCl at 308 K in absence and presence of optimum concentration (100 mgL^{-1}) of PPs. Table 3.4.6 contains Potentiodynamic polarization parameters obtained from the Tafel extrapolation of the polarization curves. The results show that the inhibition efficiency (η %) increased, while the corrosion current density (i_{corr}) decreased (49-74) with the addition of inhibitors than in its absence (1320 μA/cm^2) The decrease in i_{corr} (74 μA/cm^2) is highest in case of PP-1 and its η % is highest (97.5%) among all the three inhibitors. From the Figure 3.4.3, it could be observed that both the anodic and cathodic Tafel curves are shifting towards lower current density, indicating that the PPs reduced both the anodic and cathodic corrosion reactions. Table 3.4.6 further reveals that very slight change occurs in the values of β_a in the presence of inhibitors but a more pronounced change occurs in β_c values. This indicates that in presence of inhibitors both the anodic and cathodic reactions are affected but the effect is more pronounced on the cathodic reactions. Thus, the inhibitors are mixed type, but predominantly cathodic [Singh *et al.* (2016)], [verma *et al.* (2016**(b)**]. Also the shift in E_{corr} is

towards more negative sides i.e. cathodic with respect to blank suggesting their predominant cathodic behaviour. It is clear from Table 3.4.6 that the values of corrosion current density (i_{corr}) significantly decreased in presence of inhibitors than in their absence, suggesting their effectiveness as corrosion inhibitors.

Table 3.4.6: Potentiodynamic polarization parameters (±SD) for mild steel in 1M HCl in absence and presence of optimum concentration (100 mg L^{-1}) of PPs at 308K

Inhibitor	E_{corr} **(mV/SCE)**	i_{corr} **(µA/cm^2)**	β_a **(mV/dec)**	$-\beta_c$ **(mV/dec)**	η **(%)**
Blank	-445	1320(0.03)	74.6	123.9	----
PP-1	-513	49.9 (0.04)	84.3	174.3	96.4
PP-2	-512	68.0(0.04)	83.9	170.3	94.2
PP-3	-506	74.7 (0.13)	69.5	153.6	91.1

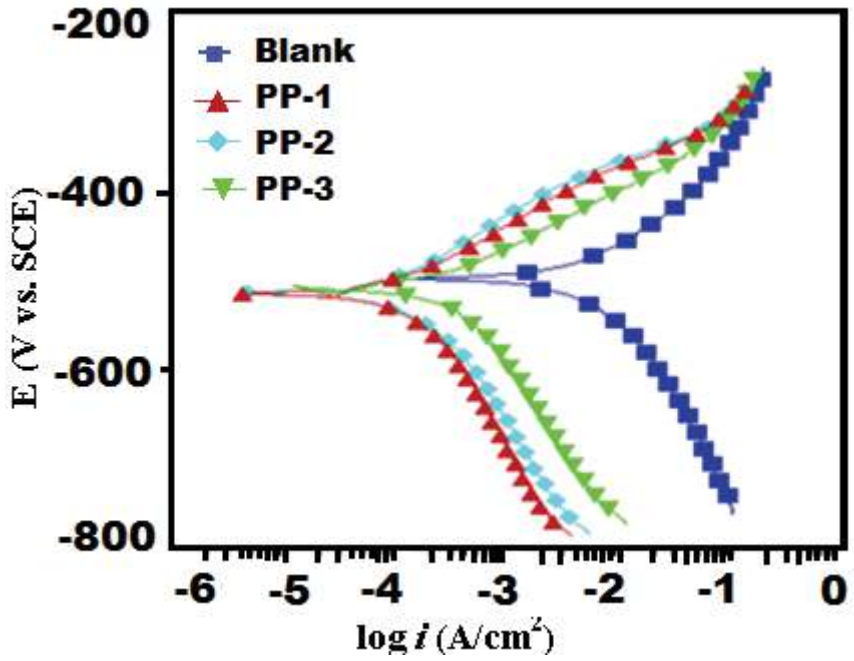

Figure 3.4.3: Polarization curves for corrosion of mild steel in absence and presence of optimum concentrations of PPs

3.4.5. Surface study

Scanning electron microscopy (SEM) study was used for determining the surface morphology of mild steel. On the inspection of SEM micrograph, the surface of uninhibited specimen is rough and damaged due to the dissolution of metal [Fig 3.4.4.1(a)]. However in the presence of optimum concentration (100 mgL^{-1}) of PP-1, PP-2 and PP-3 the specimens surface becomes relatively smooth (Fig 3.4.4.1. b-d), which indicates the presence of protective film of PPs [Mamosemh *et al* (2013)] on the metal surface.

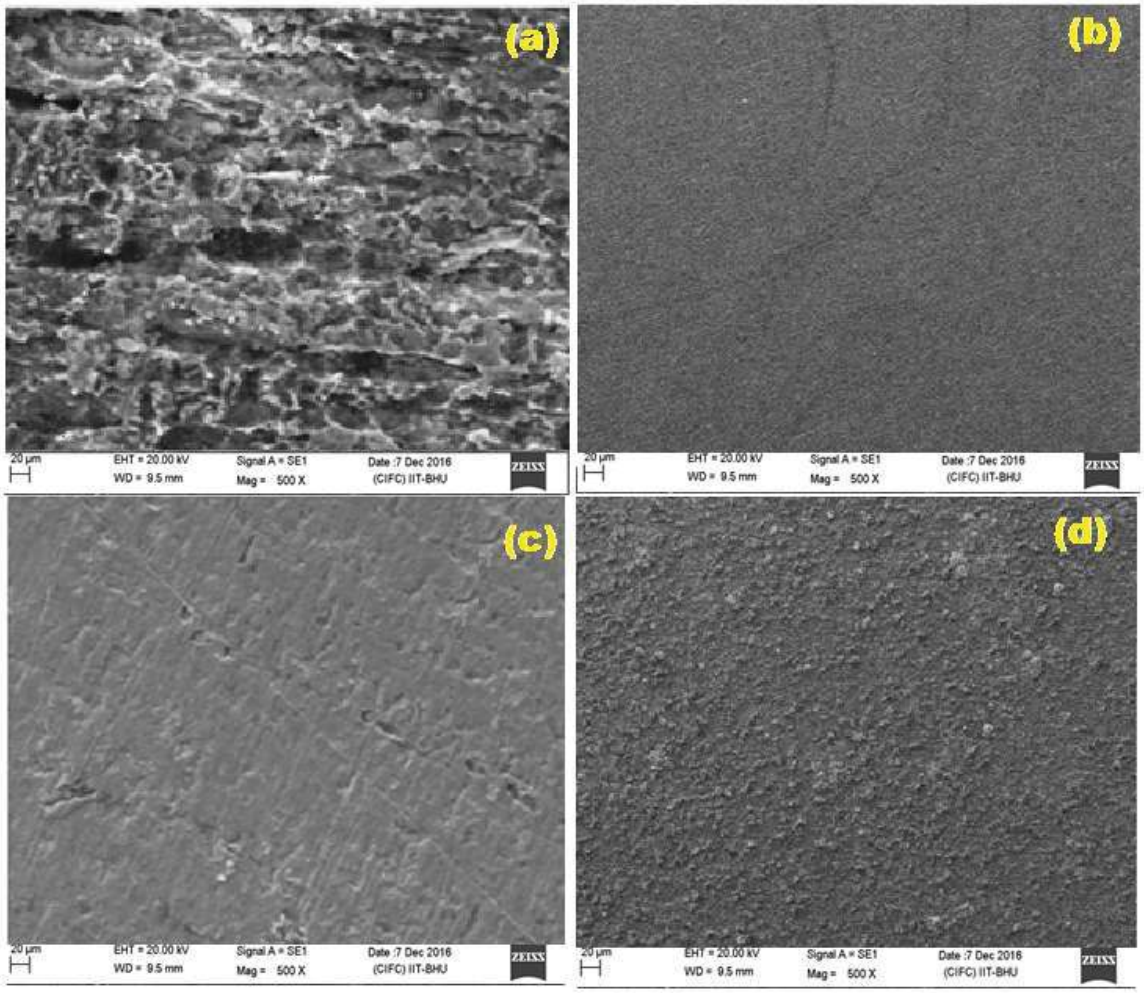

Figure 3.4.4.1: SEM image for (a) Blank (b) PP-1 (c) PP-2 (d) PP-3

The three dimensional (3D) AFM morphologies for uninhibited and inhibited samples are shown in Fig. 3.4.4.2(a-d). The average roughness in absence of inhibitor (Fig.3.4.6 a) is 400 µm. The AFM images in the presence of inhibitors are shown in Fig. 3.4.4.2(b-d) and their average roughness are reduced to 20 µm, 60 µm and 100 µm for PP-1, PP-2, and PP-3 respectively. The maximum reduction in surface roughness was observed for PP-1.

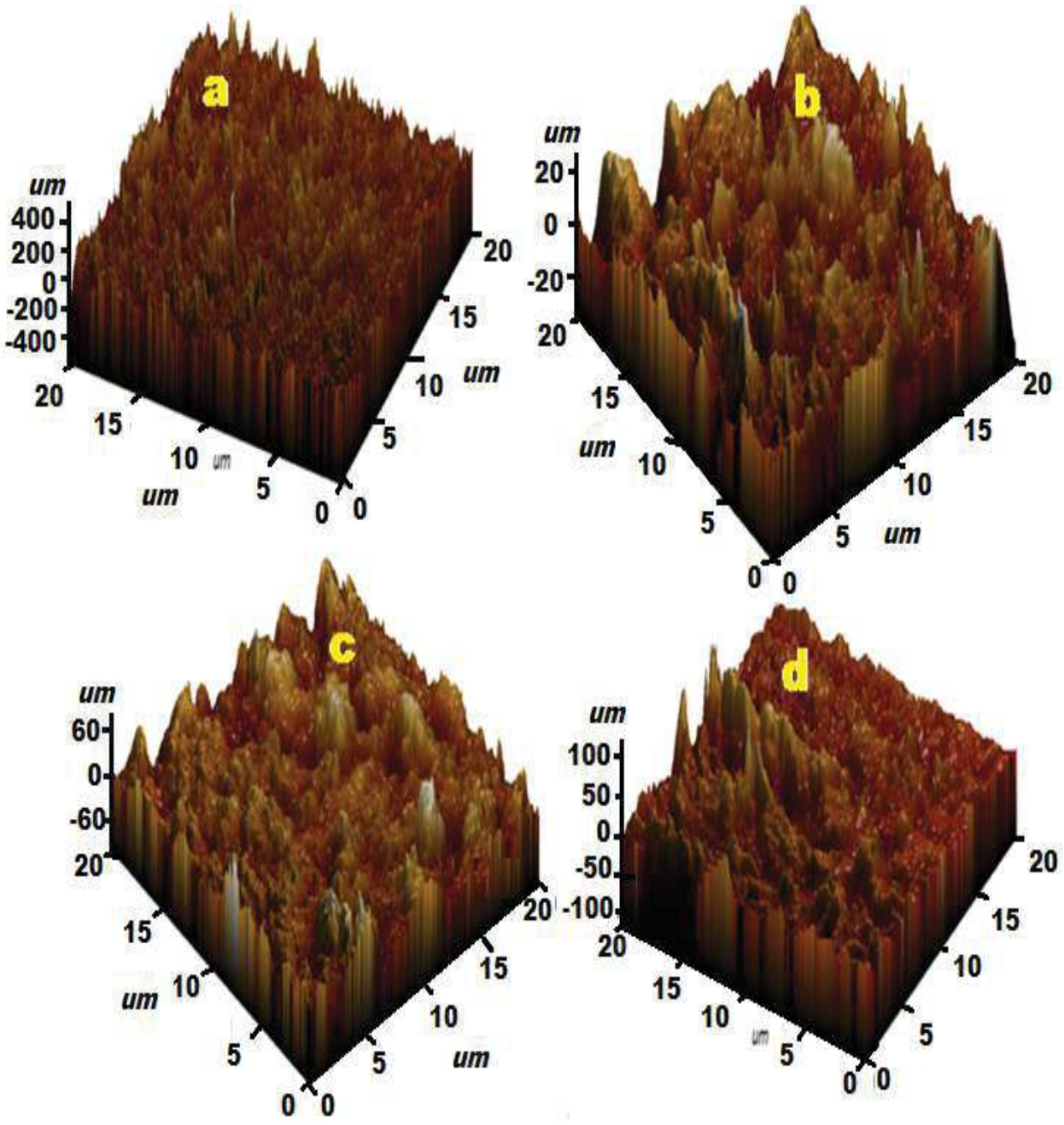

Figure 3.4.4.2: AFM images for (a) Blank (b) PP-1 (c) PP-2 (d) PP-3

3.4.6. Quantum chemical calculations

3.4.6.1. Quantum chemical calculations of neutral inhibitor molecules

Figure 3.4.5.1 shows full optimised geometry, HOMO and LUMO electron distribution of neutral PPs derivatives. From the Fig 3.4.5.1, it is clear that the HOMO regions of PP-1, PP-2, PP-3, delocalized over the pyrazolo-pyridine ring and LUMO regions of PP-1 reside over the pyrazolo-pyridine as well as substituted methoxy-phenyl ring except methoxy group and PP-2 LUMO regions reside over the pyrazolo-pyridine, and in the case of PP-3, it resides both over the pyrazolo-pyridine ring and the substituted NO_2 phenyl ring. From Table 3.4.7, it is clear that, PP-1 is the best inhibitor due to its lowest ΔE value as compared to PP-2 and PP-3. The value of E_{HOMO} for the studied inhibitors follows the order; PP-1> PP-2> PP-3. The other quantum parameters have also been calculated and are given in the Table 3.4.7. In the present case the order of the softness (σ) is as follows: PP-1> PP-2>PP-3 and the hardness (η) follows the order: PP-3>PP-2>PP-1. The global electronegativity (χ) indicates the extent to which a molecule can retains its electrons, molecule having higher value of electronegativity associated with the lower electron donation tendency. From the Table 3.4.6, it follows the order, PP-3>PP-2>PP-1. Fraction of electron transferred (ΔN) have also been calculated and for the studied PPs derivatives ΔN values are less than 3.6. Here the maximum ΔN value is obtained for PP-1 and lowest is for the PP-3.

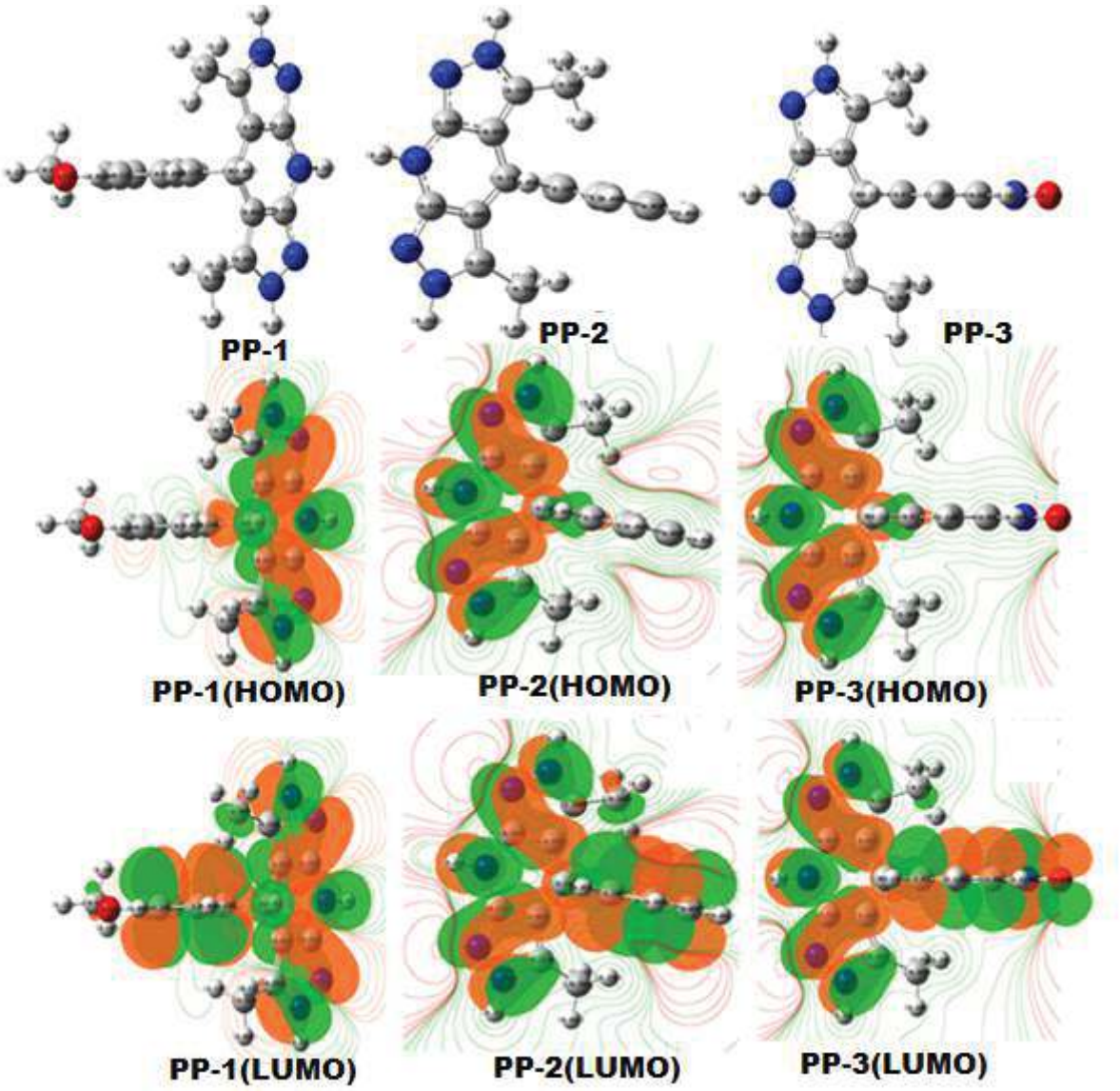

Figure 3.4.5.1: The gas phase optimized molecular structures, the HOMO, and the LUMO electron density distribution surfaces of PP-1, PP-2, and PP-3.

3.4.6.2. Quantum chemical calculations of protonated inhibitor molecules

The optimized structures, HOMO and LUMO distribution are shown in Fig. 3.4.5.2. An observation of Table 3.4.7 reveals that after protonation, the E_{HOMO} values of both inhibitors are shifted towards more negative side compared to that of E_{HOMO} values of neutral inhibitors. It suggests that after protonation, the electron donating capability of inhibitors

decreased. Furthermore, Table 3.4.7 reveals that all the calculated ΔN values in case of inhibitors are negative, which means that the donation of electrons from inhibitor molecules to metal surface is not possible. It is also noted that E_{LUMO} values of protonated inhibitors shift towards more negative side as compared to the neutral, which further suggests that the protonated inhibitors have higher electron accepting capability compared to the neutral form. All these factors cause the change in HOMO and LUMO distribution as compared to the neutral form.

Table 3.4.7: Calculated quantum chemical parameters of neutral and protonated PPs DFT (6-31G, d, p)

Inhibitors	μ **(Debye)**	E_{HOMO} **(eV)**	E_{LUMO} **(eV)**	ΔE **(eV)**	η **(eV)**	$^{b}\sigma$ **(eV^{-1})**	χ **(eV)**	ΔN **(eV)**
Neutral form								
PP-1	2.85	-5.32	-1.04	4.27	2.13	0.46	3.18	0.38
PP-2	3.00	-5.421	-1.03	4.38	2.19	0.45	3.22	0.36
PP-3	3.38	-5.81	-1.02	4.78	2.39	0.41	3.42	0.29
Protonated form								
PP-1	11.1	-7.54	-5.46	2.07	1.03	0.96	6.50	-0.80
PP-2	8.02	-9.73	-5.32	4.41	2.20	0.45	7.52	-0.61
PP-3	7.29	-9.68	-5.14	4.54	2.27	0.44	7.41	-0.57

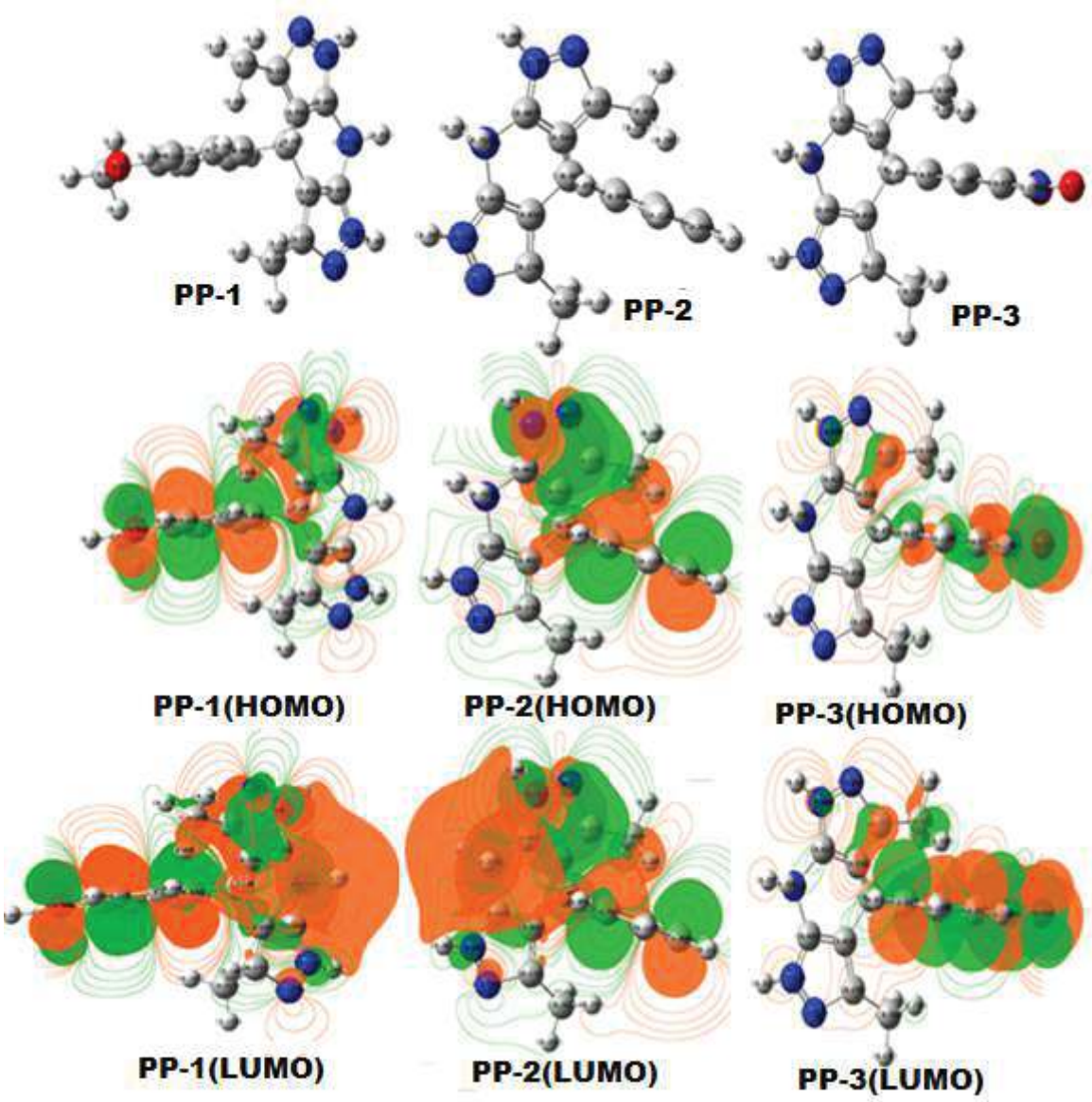

Figure 3.4.5.2: The protonated phase optimized molecular structures, the HOMO, and the LUMO electron density distribution surfaces of PP-1, PP-2, and PP-3.

3.4.6.3. Molecular electrostatic potential

The MEP map of the inhibitors molecule for the neutral and the protonated inhibitors molecules and are shown in the Fig 3.4.5.3(a-f) respectively. The red colour shows the region of the most negative sites and the green colour for the zero electrostatic potential. The blue

region gives the most positive site of the inhibitor molecules. Fig 3.4.3 (a-c) shows MEP map for neutral molecules for all the three PP-1, PP-2 and PP-3 respectively, the colour region lies in between red - green and blue. The red region occupied by the N atom of the pyrazole-pyridine ring which is the most electronegative sites in the case of PP-1 and PP-2. But in the case of PP-3 the red color region is found over the N atoms of the pyrazole-pyridine rings as well as the NO_2 group of the substituent benzene ring. In the case of 3.4.5.3(d-f) for protonated PP-1, PP-2 and PP-3 the deep blue colour region is spread all over the ring which indicates the deficiency of electrons, also tells about that there is no tendency of donating the electrons by all the three inhibitors. These data very well correlates with the data of the ΔN calculated from DFT method.

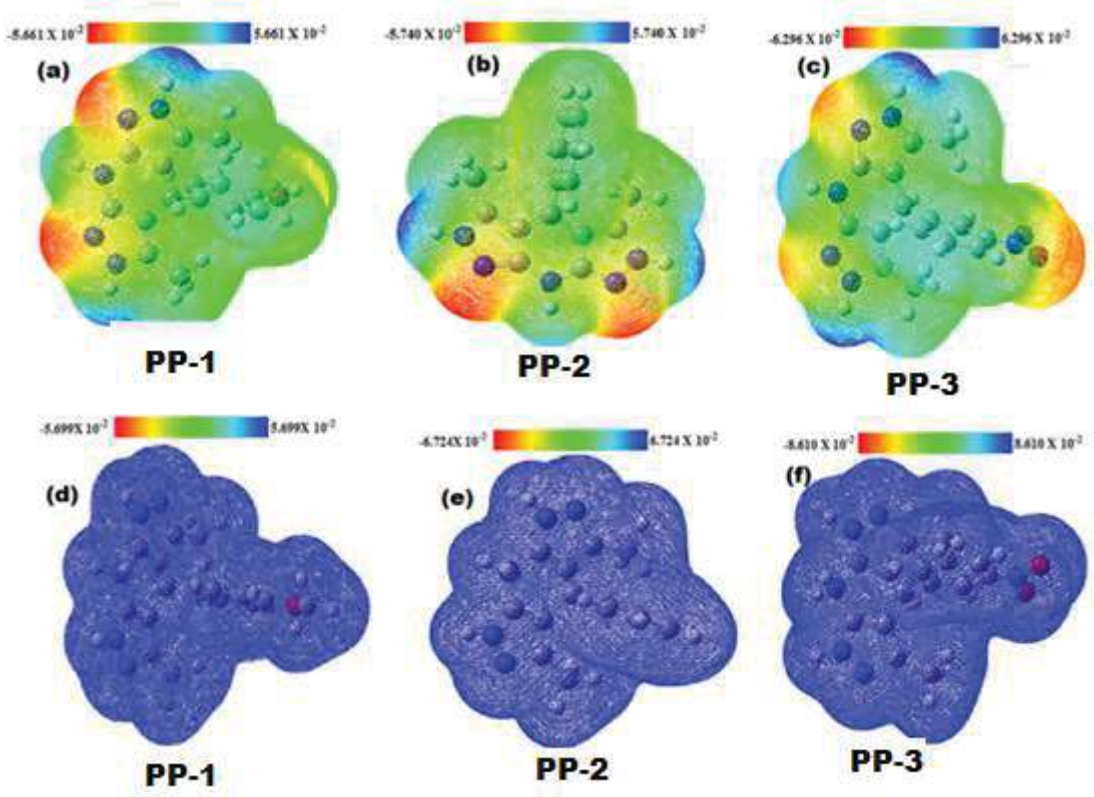

Figure 3.4.5.3: electrostatic potential map for neutral (a-c) and protonated (d-f) PP-1, PP-2, PP-3 respectively

3.4.6.4. Fukui index analysis

Table 3.4.8 shows the calculated fukuii indices, the most electrophilic regions for PP-1 are on the C(15), C(16), C(17), C(19) and on C(20), while the nucleophelic regions f_k^- are at the C(1), C(2), C(4), C(5), N(6), N(7), N(8), C(9), N(10), N(11), and C(12) respectively. In the case of PP-2 the most favoubarale sites for electron acceptance (f_k^+) are C(1), C(2), C(5), and N(6) and the nucleophilic regions are spread over the C1, C2, N7, N8, C10, C(11), N(12), N(13), N(14), C(15), N(16), N(17) and over the C(18) respectively. In the case of PP-3 the f_k^- regions lies on the C(1), C(2), C(4), C(5), N(6), N(7), N(8), C(9), N(10), N(11), and C(12), and the electrophilic regions (electron accepting) f_k^+ reside over C(14), C(15), C(16), C(18), N(19), O(20) and O(21) these atoms respectively.

The analysis of fukuii indexes reveals that pyrazolo-pyridine ring and phenyl ring are the reactive sites and responsible for donor-acceptor interactions and thus facilitate bonding between metal and inhibitor molecules.

Table 3.4.8: Calculated Fukui functions for the studied inhibitor molecules in neutral form

PP- 1	***fk-***	***fk+***	**PP- 2**	***fk-***	***fk+***	**PP- 3**	***fk-***	***fk+***
C1	0.0464	0.0004	C1	0.0000	-0.0050	C1	0.0488	0.0001
C2	0.0435	0.0014	C2	0.0091	0.1732	C2	0.0412	0.0009
C3	-0.0038	0.0025	C3	0.0001	0.3246	C3	-0.0036	0.0007
C4	0.0424	0.0010	C4	0.0001	0.0019	C4	0.0405	0.0006
C5	0.0428	0.0004	C5	0.0000	0.1786	C5	0.0449	0.0001
N6	0.2049	0.0000	N6	0.0002	0.3062	N6	0.2020	0.0000
N7	0.1753	0.0000	N7	0.0488	0.0007	N7	0.1749	0.0001
N8	0.0470	0.0002	N8	0.0412	0.0110	N8	0.0445	0.0001
C9	0.0742	0.0007	C9	-0.0036	-0.0002	C9	0.0788	0.0002
N10	0.1675	0.0001	C10	0.0404	0.0063	N10	0.1665	0.0001
N11	0.0475	0.0004	C11	0.0449	0.0011	N11	0.0449	0.0002
C12	0.0783	0.0005	N12	0.2021	0.0001	C12	0.0829	0.0003
C13	-0.0036	0.0008	N13	0.1749	0.0003	C13	0.0091	-0.0052
C14	-0.0035	0.0004	N14	0.0444	0.0005	C14	0.0000	0.1340
C15	0.0092	-0.0146	C15	0.0787	0.0007	C15	0.0003	0.0559
C16	0.0000	0.2046	N16	0.1666	0.0000	C16	0.0001	0.1453
C17	0.0002	0.2848	N17	0.0449	0.0004	C17	0.0001	-0.0036
C18	0.0000	-0.0118	C18	0.0829	0.0014	C18	0.0001	0.2027
C19	0.0001	0.2254	C19	-0.0038	0.0006	N19	0.0000	0.1837
C20	0.0001	0.3041	C20	-0.0037	0.0005	O20	0.0001	0.1447
O21	0.0000	0.0003				O21	0.0000	0.1454
C22	0.0000	0.0023				C22	-0.0038	0.0007
						C23	-0.0037	0.0003

3.4.7. MD simulations

Figure 3.4.6.1(a) and 3.4.6.1(b) shows that after 500ps, both the temperature and energy reach balance. Figure 3.4.6.2 and 3.4.6.3 represent the equilibrium configurations for the three corrosion inhibitors both in the neutral and protonated forms respectively. From the Figure (3.4.6.2(and 3.4.6.3) it is clear that all three inhibitor molecules of both forms were moved gradually near the Fe (110) surface. And the calculated interaction and the binding energies are given in the Table 3.4.9. The corrosion inhibition performance of studied inhibitors follows the order: PP-1 > PP-2 > PP-3. The presence of electron releasing group (-OCH_3) increasing the adsorption ability of PP-1[Fouda *et al* (2008)].The low interaction energy in case of PP-3 is attributed to the presence of electron withdrawing NO_2 group [Saha *et al*. (2016**(b)**)]. The interaction energy protonated inhibitors with metal are more negative than neutral inhibitors/ metal, thereby suggesting that protonated inhibitors are better adsorb than neutral inhibitors. These findings agree well with the experimental results as well as with previously reported studies [Zhang *et al* (2016)].

Table 3.4.9: Interaction energies between the inhibitors and Fe (110) surface (kJ/mol) in gas phase

System	Neutral form		Protonated form	
	$E_{Interaction}$ (kJ/mol)	$E_{Binding}$ (kJ/mol)	$E_{Interaction}$ (kJ/mol)	$E_{Binding}$ (kJ/mol)
Fe + **P-1** +500H_2O + $5H_3O^+$ + $5Cl^-$	-701.13	701.13	-743.70	743.70
Fe + **P-2**+500H_2O + $5H_3O^+$ + $5Cl^-$	-673.11	673.11	-711.51	711.51
Fe + **P-3**+500H_2O + $5H_3O^+$ + $5Cl^-$	-562.51	562.51	-652.33	652.33

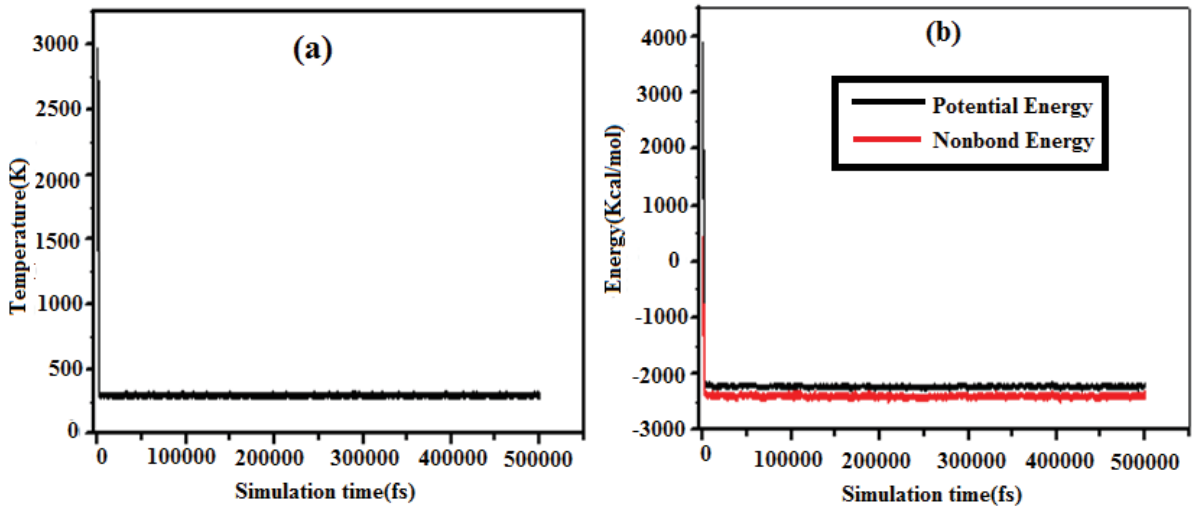

Figure 3.4.6.1(a) and (b): Temperature (a) and Energy (b) equilibrium curves of studied inhibitors adsorbed on the Fe (1 1 0) surface in solution.

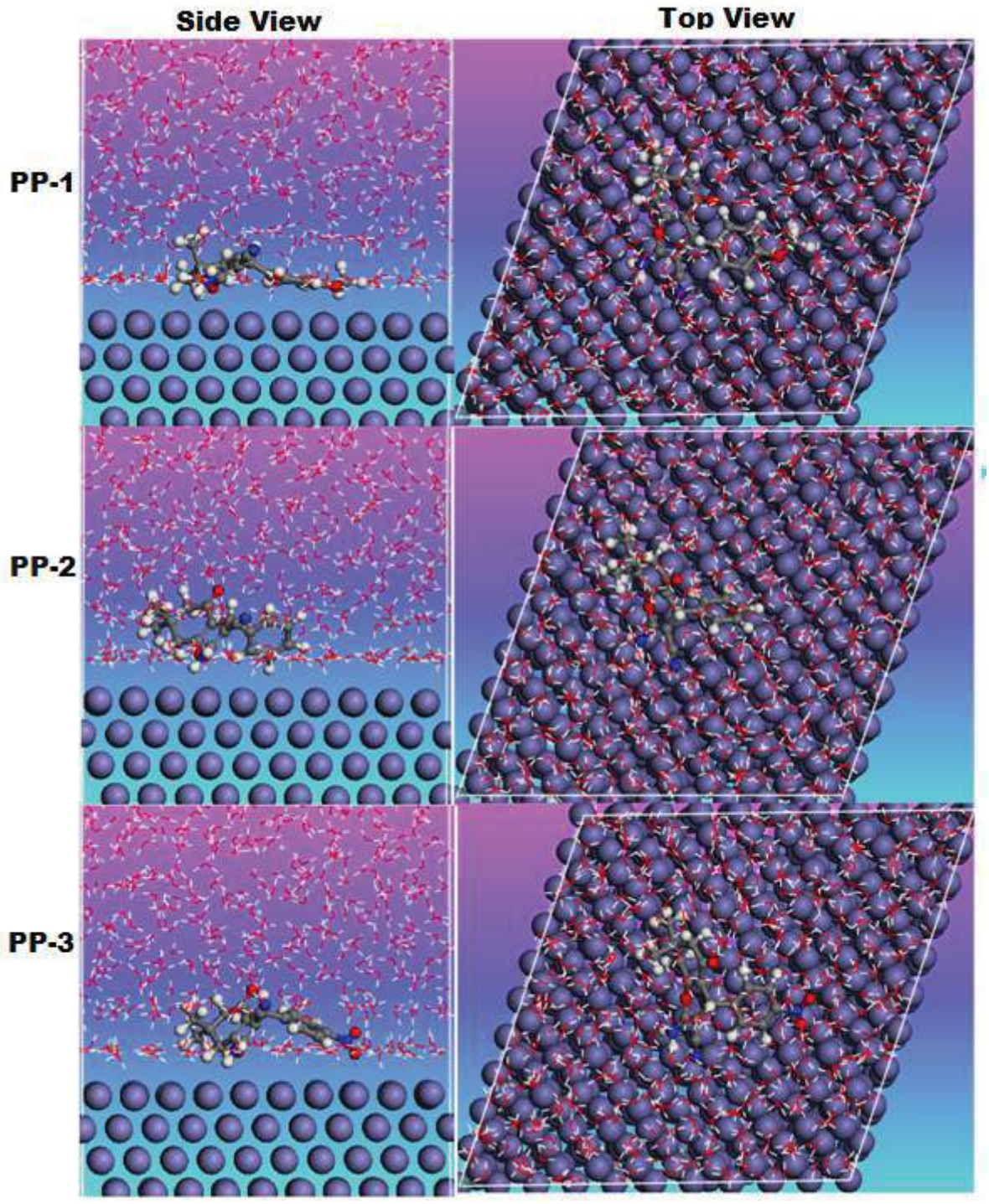

Figure 3.4.6.2: Side views of the most stable configurations for adsorption of (a) PP-1 (b) PP-2 and PP-3 on Fe (110) surface calculated using Molecular Dynamics simulations in the neutral phase in the aqueous medium

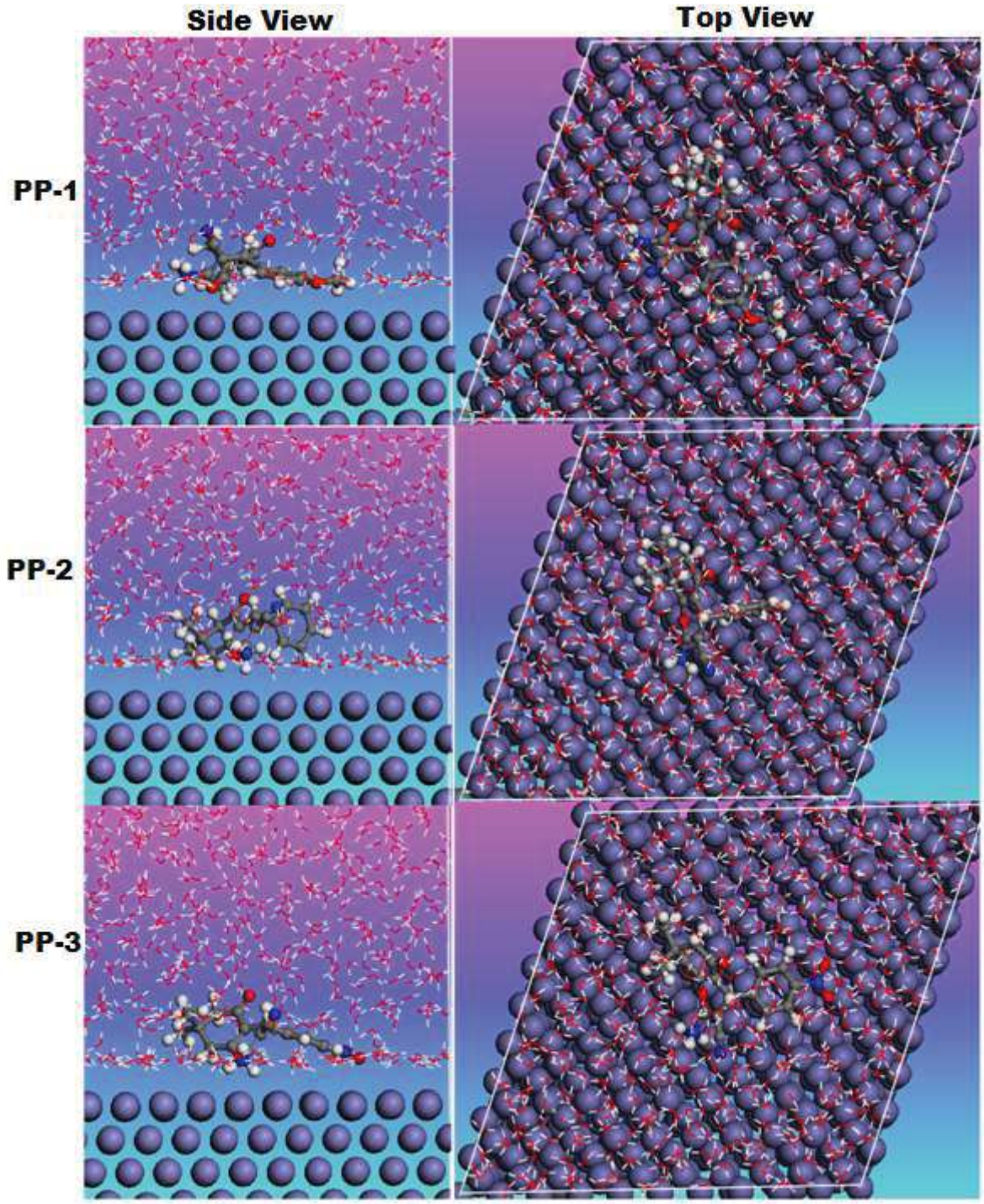

Figure 3.4.6.3: Side views of the most stable configurations for adsorption of (a) PP-1 (b) PP-2 and PP-3 on Fe (110) surface calculated using Molecular Dynamics simulations in the protonated phase in aqueous medium

3.4.8. Diffusion mechanism

MD simulation is considered as reliable method to estimate the diffusion coefficients of corrosive species [Yan *et al* (2013)]. In this case, the mean square displacements (MSD) functions were used to investigate the transport of corrosive particles (Cl^- and H_3O^+) inside inhibitor films. A small diffusion coefficient of the corrosive species means strong hinder of simulation system which will induce to high inhibition efficiency [Hu *et al.* (2011)], [Zhang *et al*. (2011)], [Guo *et al* (2015)], [Xie *et al* (2015)]. The diffusion coefficient is defined as follow [Zhang *et al.* (2016):

$$MSD(t) = \left[\frac{1}{N} \sum_{i=1}^{N} \left| R_i(t) - R_i(0) \right|^2 \right] \tag{3.2}$$

$$D = \frac{1}{6} \lim_{t \to \infty} \frac{d}{dx} \sum_{i}^{n} \left[\left| R_i(t) - R_i(0) \right|^2 \right] \tag{3.3}$$

Where $\left| R_i(t) - R_i(0) \right|^2$ and N are the mean-square displacement (MSD) and number of target molecules respectively, while $R_i(t)$ and $R_i(0)$ are the positions of corrosive species at time t and 0, respectively. Diffusion coefficients have been calculated using the following equation:

$$D = \frac{m}{6}(1) \tag{3.4}$$

"m" is the slope of MSD curve.

Figure 3.4.7 shows the diffusion models and MSD curves of Cl^- and H_3O^+ in the three corrosion inhibitor films at 303 K. Thus, Table 3.4.10 listed the calculated diffusion coefficients of Cl^- and H_3O^+ in three inhibitor films. It can be seen from the Table 3.4.10 that the diffusion coefficients of Cl^- and H_3O^+ in the inhibitor film of PP-1, PP-2 and PP-3 follow the order of: $D_{H_3O^+}$ (PP-3) > $D_{H_3O^+}$ (PP-2) > $D_{H_3O^+}$ (PP-1) and D_{Cl^-} (PP-3) > D_{Cl^-} (PP-2)

$> D_{Cl^-}$ (PP-1). These results are in accordance with the reported inhibition efficiency. The much smaller diffusion coefficients of Cl^- and H_3O^+ in PP-1 indicates that the migration rate of these corrosive species are both be inhibited. This is because; the inhibitor film constrains the diffusion of these particles [Zhang *et al* (2011)]. It is also apparent from the Table 3.4.10 that the diffusion coefficients of Cl^- and H_3O^+ in PP-2 and PP-3 inhibitor film increased comparing with that in PP-1 which indicates the decrease in the inhibitive capacity of these inhibitors against the diffusion of the corrosive particles.

Table 3.4.10: The diffusion coefficient of Cl^- and H_3O^+ at 303 K

System	$D_{H_3O^+}$ $(10^{-9} m^2/s)$	D_{Cl^-} $(10^{-9} m^2/s)$
PP-1	0.0086	0.0021
PP-2	0.0410	0.0065
PP-3	0.0515	0.0227

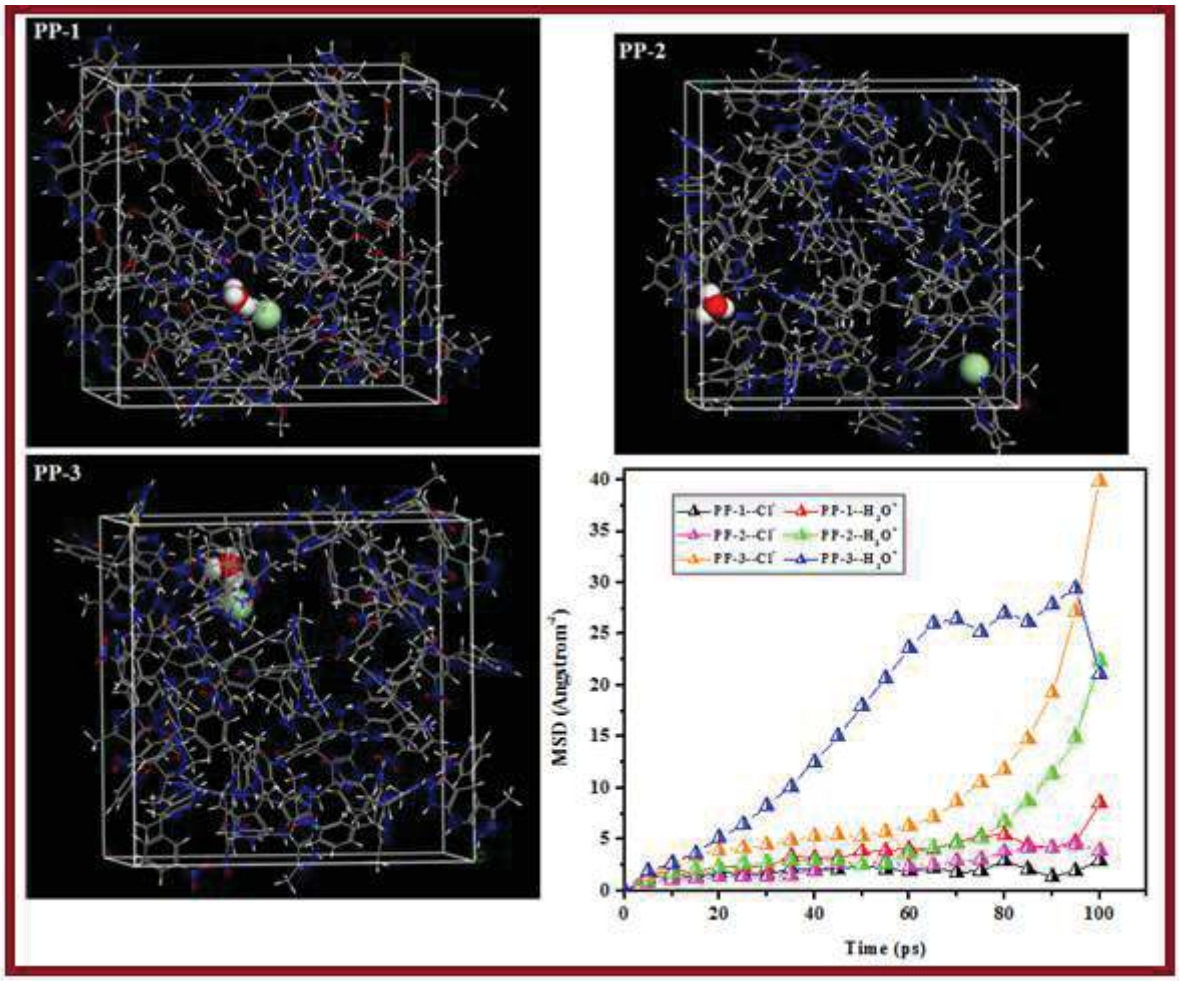

Figure 3.4.7: The diffusion models and MSD curves of Cl^- and H_3O^+ in the PPs corrosion inhibitor films at 303 K.

3.5. Mechanism of inhibition

The following mechanism can be proposed on the basis of experimental and theoretical methods (Figure 3.4.8:

(1) In hydrochloric acid solution pyrazolo-pyridine molecules can exist in protonated and neutral form. The protonated inhibitor can adsorbed on mild steel surface at previously adsorbed chloride ions

$$PP + H^+ \rightleftarrows PP - H^+$$

In the beginning Cl^- ions get adsorbed over the mild steel (MS), which create negative charge on the metal surface. The protonated inhibitor molecules are adsorbed on chloride ions through electrostatic interaction (physical adsorption).

(2) The protonated inhibitor molecules get reduced by accepting the electron from the cathode and become neutral. These neutral inhibitor molecules are chemically adsorbed on metal surface through their lone pair of electrons.

(3) Further back-bonding (reterodonation) occurs between the inhibitor and the metal surface, which strengthen the adsorption of inhibitor molecules.

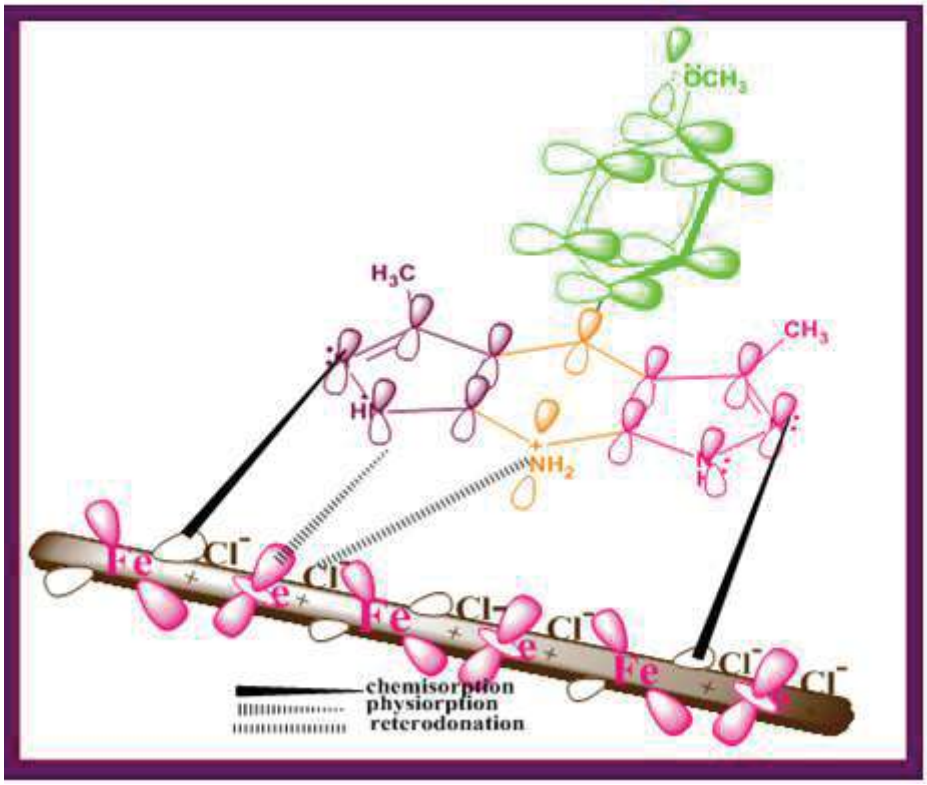

Figure 3.4.8: Schematic adsorption and inhibition mechanism of PP-1 molecule